DEUTERON COMPTON SCATTERING BELOW PION THRESHOLD

BY

LUKE S. MYERS

DISSERTATION

Submitted in partial fulfillment of the requirements
for the degree of Doctor of Philosophy in Physics
in the Graduate College of the
University of Illinois at Urbana-Champaign, 2010

Urbana, Illinois

Doctoral Committee:

Professor David Hertzog, Chair
Professor Alan Nathan, Director of Research
Professor Jose Mestre
Professor John Stack

Abstract

A series of experiments were performed at the Tagged Photon Facility at MAX-lab in Lund, Sweden to study photon scattering from the deuteron and extract the neutron polarizabilities. The deuteron Compton scattering cross section was measured at laboratory angles of 60^o, 120^o, and 150^o for photon energies from 70 - 112 MeV. The photons were scattered from the Lund liquid deuterium target and detected in three large (20" x 20") NaI photon spectrometers. These detectors have sufficient energy resolution ($\sim$2% at 100 MeV) to separate the elastically and inelastically scattered photons.

The extracted scattering cross section for this experiment was found to have angular distributions that matched prior experiments but needed a scaling factor to bring the absolute cross section into agreement. This scaling factor was determined to have a value of 1.47 $\pm$ 0.10. Suggestions are made for future studies that could yield further knowledge of the scaling factor and potentially allow for this data to be re-normalized.

Dedicated to my parents and sisters. Thank you for all your support through this process and all the other things in life.

Acknowledgments

Praise to God and thanks to Dr. Michael Robertson and the entire staff at the Indiana University Medical Center. Without your care and skill I don't know that I would be here. Blessings to you all.

I would like to thank my adviser Alan Nathan for his guidance and support throughout this entire experiment. I truly appreciate all the expertise and guidance you've passed along over these years.

I would also like to mention Gerald Feldman, Mike Kovash, Lennart Isaksson, and Bent Schroeder for all their hard work in getting this experiment approved, commissioned, and running. I can not thank each of you enough for your willingness to discuss any detail that came up throughout the experiment.

To Kevin Fissum, well, I just can't find the right words. I enjoyed all of our conversations – both those that focused on everything physics and, more so, those that didn't. Thank you for so kindly welcoming from the first day and for all your advice. I feel fortunate to call you a friend.

To Kurt Hanson, Magnus Lundin, Jason Brudvik and the rest of the nuclear physics group at MAX-lab, I am grateful for all the time and effort you guys poured into making this experiment run as smoothly as it did. Thank you for always being willing to explain what you were doing. And a special thanks to Magnus for always answering all of my many questions about the analysis program.

I would also like to thank all the machine operators at MAX-lab, especially Lars-Johan Lindgren and Per Lilja, for their hard work in setting up our electron beam and keeping it running smoothly. Our demands were new to your facility and I appreciate your efforts to supply the beam we needed.

I would like to thank Ulrika Forsberg, specifically, for taking the time to explain (more than once) the ins and outs of the beam control system. Also, for her friendship, unusual conversations, and her valiant efforts to introduce me to Swedish culture. I can only hope to be as much a help to your Ph.D. process as you've been to mine.

To Harald Griesshammer I offer my sincerest thanks for always being there to help me out with some up-to-date theoretical calculations. I'm not sure how you and your collaborators

do what you do, but I am grateful.

I would like to thank Sean Stave, Seth Henshaw, Daniel Mittelberger, Kasey Lewis, and John Capone for their assistance in times of need during this experiment. Your efforts made sure that this experiment ran as smoothly as it did. I am humbled by your willingness to help out someone who was once a stranger.

To my committee: Profs Hertzog, Mestre, and Stack. Thank you for waiting so patiently and for your direction in this process.

Finally, to the many family and friends who I simply do not have time or space to mention by name in this space: please know that I am here only because at some time you provided some words of encouragement, perspective, laughter or support when it was most needed. I thank God for all of you. I feel like this accomplishment is due to all of you and I am just the one accepting it. Thank you from the bottom of my heart.

This material is based upon work supported by the National Science Foundation grant 0855569, the Swedish Research Council (VR), the Crafoord Foundation, and the Royal Physiographic Society in Lund. Additionally, we would like to acknowledge support of the European Community-Research Infrastructure Activity under the FP6 "Structuring the European Research Area" program (Hadron Physics, contract number RII3-CT-2004-506078).

Table of Contents

List of Figures

List of Tables

List of Abbreviations

ADC	Analog charge-to-Digital Converter
CFD	Constant Fraction Discriminator
χPT	Chiral Perturbation Theory
DAQ	Data AcQuisition
FP	Focal Plane hodoscope
FWHM	Full Width Half Maximum
LED	Leading Edge Discriminator
LEX	Low energy EXpansion
LINAC	LINear ACcelerator
ndf	number of degrees of freedom
PMT	PhotoMultiplier Tube
SAL	Saskatchewan Accelerator Laboratory
TDC	Time-to-Digital Converter
ToF	Time-of-Flight

1 Introduction

1.1 Overview

The last twenty-five years have seen an increased interest in the structure of nucleons led by both improved theoretical models and more sensitive experimental measurements. In particular, photon scattering has been used to investigate the response of nucleons to external electric and magnetic fields. These responses, the electric and magnetic polarizabilities (denoted by α and β, respectively), yield information about the internal structure of the proton and neutron.

Recent studies of proton targets have led to improved knowledge of the polarizabilities. At this time, the proton cross section and extracted polarizabilities are well-known. While multiple efforts have been made to measure the neutron polarizabilities these lack the precision of the proton measurements at this time. This experiment seeks to use elastic Compton scattering from the deuteron to measure the neutron polarizabilities. Its purpose was to extend the range of the current world data of the deuteron Compton scattering cross section and to extract neutron polarizabilities with improved precision.

This chapter will define the polarizabilities and briefly cover their connection to photon scattering. The current status of the experimental nucleon polarizabilities will be discussed and, lastly, there will be a brief review of the current theoretical work that is necessary to extract polarizabilities from the scattering data.

1.2 Definition of Polarizability

A nucleon, or any other composite particle, consists of a number of sub-particles that can react to any external field – in particular, electric and magnetic fields. The tendency of the constituent particles to move under the influence of a static or slowly varying field creates an induced electric or magnetic dipole moment. These dipole moments are given by

$$\vec{p} = \alpha \vec{E} \tag{1.1}$$

$$\vec{m} = \beta \vec{B}, \tag{1.2}$$

where α and β are the electric and magnetic polarizabilities, respectively, and relate the induced moment to the applied field. One must be careful to remember that these moments are not related to the intrinsic moments ($\vec{d}$ and $\vec{\mu}$). The electric and magnetic polarizabilities can be thought of as defining the "stretchability" and "alignability" of the nucleon, respectively. This is because the electric dipole moment results from the separation of opposite charges and the magnetic moment arises from a net direction in the constituent moments. The induced magnetic dipole moment has two parts: the first is a paramagnetic term resulting from the alignment of the internal moments to the magnetic field, while the second is a diamagnetic term that arises from the magnetic field producing an induced current which results in a magnetic field (and moment) that opposes the externally applied field (Lenz's Law). This can be seen in Fig. 1.1.

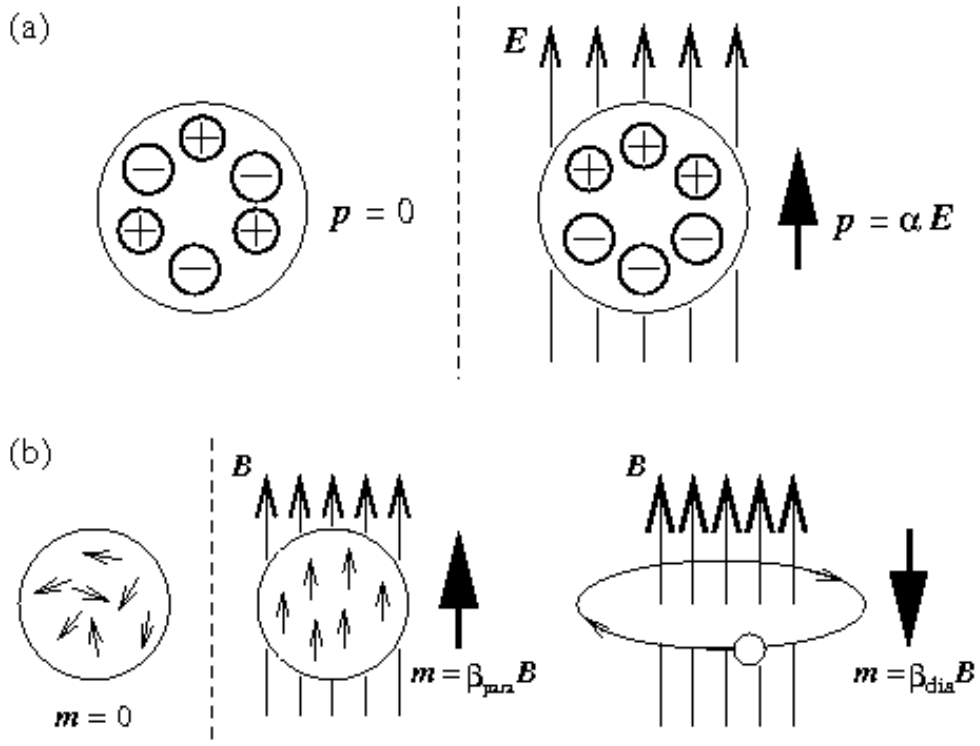

Figure 1.1: Response of a particle to applied electric (E) and magnetic (B) fields. (a) The induced electric dipole moment is caused by the separation of the constituent particles when exposed to the external electric field. (b) The induced magnetic dipole moment is a result of the internal moments aligning with the external magnetic field. Taken from [Hor99].

A polarizability of zero indicates that the particle is "frozen" and unaffected by external fields. Likewise, as the polarizability increases, the particle is more easily influenced. Clearly, these structure constants are important to understanding the internal structure of the proton and neutron.

1.3 Photon Scattering

One of the methods used to probe nucleon structure is photon scattering. A qualitative understanding of this process can be understood by considering the nucleon and the deuteron in a classical manner. An exact, quantum-mechanical, low-energy expression is also given in this section. In order to extract the polarizabilities from higher energy scattering experiments such as this one, more detailed theoretical calculations are necessary. These are presented later in the chapter.

1.3.1 Classical Model of the Nucleon

The proton and neutron can be viewed classically as consisting of two charged masses connected by an ideal spring with a spring constant k. The charges and masses can be obtained by applying the knowledge of the quark structure of the nucleons. Models of the proton and neutron are shown in Fig. 1.2.

An oscillating electromagnetic field causes the nucleon, as well as its constituent particles, to oscillate and re-radiate electromagnetic fields. The photon scattering cross section in this model can be written down for both the proton and neutron ([Luc94]) as

$$\frac{d\sigma}{d\Omega_p} = r_0^2 \left| 1 - \frac{2\omega^2}{(\omega_p^2 - \omega^2) - i\omega\Gamma_p} \right|^2 \left(\frac{1+\cos^2(\theta)}{2} \right) \tag{1.3}$$

$$\frac{d\sigma}{d\Omega_n} = r_0^2 \left| -\frac{2\omega^2}{(\omega_n^2 - \omega^2) - i\omega\Gamma_n} \right|^2 \left(\frac{1+\cos^2(\theta)}{2} \right), \tag{1.4}$$

where ω_p and Γ_p represent the energy of the proton resonance and its damping width, ω_n and Γ_n represent the neutron resonance, and r_0 is the classical proton radius. The neutron cross section differs from the proton in that it lacks the center-of-mass term that gives rise to the Thomson scattering cross section[1] (proportional to r_0) – this is due to the lack of charge

[1]Thomson scattering is the scattering from a point-like object where $\frac{d\sigma}{d\Omega} = r_N^2 \sin^2(\theta)$ and $r_N = \frac{q_N^2}{4\pi\epsilon_0 M_N c^2}$.

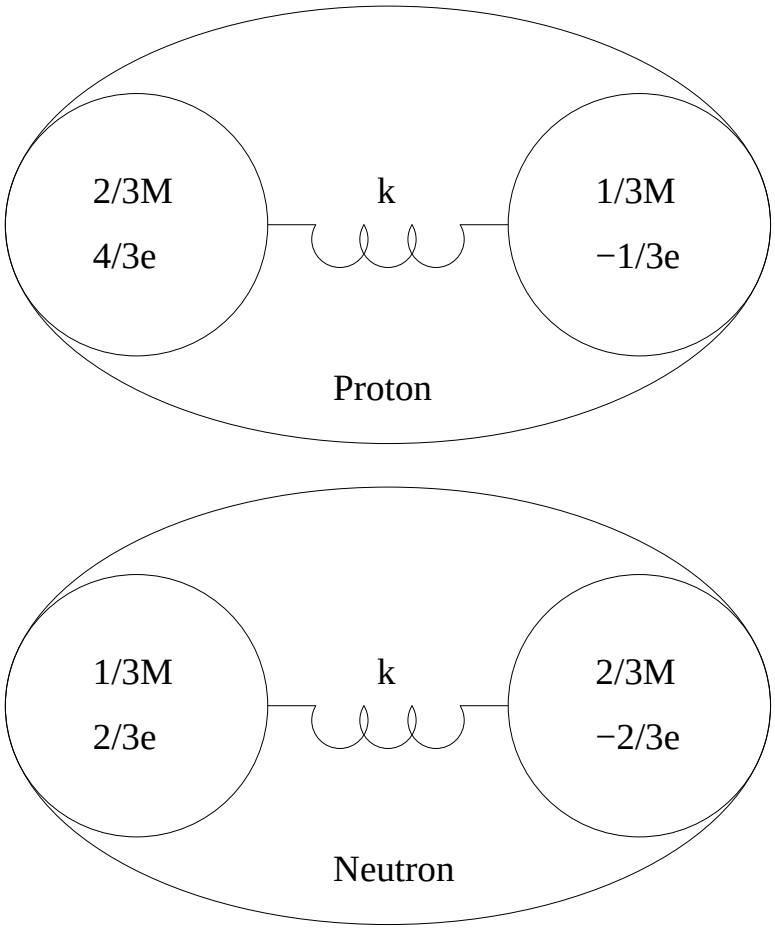

Figure 1.2: Classical picture of the nucleons in a mass-spring model. The charges and masses are inferred from a three quark model of the nucleon and the charge properties of the quarks.

of the neutron.

Assuming that $\omega \ll \omega_{p,n}$, and writing the electric polarizability arising from this model as $\alpha_{p,n} = \frac{2r_0}{\omega_{p,n}^2}$ allows the cross section to be approximated as

$$\frac{d\sigma}{d\Omega_p} = (r_0^2 - 2r_0\omega^2\alpha_p)\left(\frac{1+\cos^2(\theta)}{2}\right) \tag{1.5}$$

$$\frac{d\sigma}{d\Omega_n} = \alpha_n^2\omega^4\left(\frac{1+\cos^2(\theta)}{2}\right). \tag{1.6}$$

For low photon energies, the neutron scattering cross section is much smaller than that of the proton.

1.3.2 Low Energy Expansion

Quantum-mechanically, the cross section for photon scattering from the nucleons has been fully developed. At very low energies, the photon is insensitive to the internal structure of the nucleon and the cross section is that for a spin-1/2 structureless particle with an anomalous magnetic moment λ. The cross section is given by [Pow49]

$$\frac{d\sigma}{d\Omega}^{Pow} = \frac{1}{2}(\frac{q_N^2}{m_N c^2})^2(\frac{\omega'}{\omega})^2(1+\cos^2\theta) + (\frac{\omega\omega'}{m_N^2 c^4})[(1-\cos^2\theta) + f(\cos\theta)], \qquad (1.7)$$

where $f(\cos\theta)$ depends on λ, the nucleon charge and mass are given by q_N, m_N, and ω, ω' are incident and scattered photon energies.

At higher energies, but still below pion threshold, the cross section must be corrected for terms arising from the internal structure. The lowest order corrections at $O(\omega^2)$ are sensitive to the nucleon electromagnetic polarizabilities α_N and β_N. The cross section can be written exactly for these low energies as

$$\frac{d\sigma}{d\Omega}^{LEX} = \frac{d\sigma}{d\Omega}^{Pow} - \frac{1}{2}(\frac{q_N^2}{m_N c^2})(\frac{\omega\omega'}{(\hbar c)^2})[(\alpha_N+\beta_N)(1+\cos\theta)^2 + (\alpha_N-\beta_N)(1-\cos\theta)^2]. \quad (1.8)$$

This equation is the Low Energy Expansion (LEX) of the cross section. Further corrections can be examined by going to higher photon energies. As seen in [Bab98], the terms that arise at $O(\omega^4)$ are independent of the nucleon charge but depend non-linearly on α_N and β_N and also on the so-called spin polarizabilities (quadrupole excitations). Since the photon energies in this experiment were chosen so that these effects are negligible, they will not be discussed in detail here.

Equation 1.8 provides some insight into how the cross section depends on α and β. At forward scattering angles, the cross section is dominated by the sum of the polarizabilities. It turns out that this quantity is constrained by the Baldin Sum Rule (discussed below). In combination with the LEX, this leads to the conclusion that the theoretical cross section must be model-independent in the low-energy, forward-angle regime. The input necessary to extract α and β comes from backward angle scattering. In this scenario, the cross section is dominated by the difference of the polarizabilities. Scattering from higher energies, but still sufficiently low so as to ignore terms of $O(\omega^4)$, is needed to distinguish the effects predicted by various quantum-mechanical theories.

Baldin Sum Rule The Baldin Sum Rule [Bal60] relates the sum of the polarizabilities to the total photoabsorption cross section of the nucleon σ_γ^N. It does so via the Optical Theorem, which relates the photoabsorption cross section to the imaginary part of the forward scattering amplitude. Dispersion relations are used to relate the real and imaginary parts of the complex scattering amplitude. By combining these with the differential cross section, the following relationship was found

$$\alpha_N + \beta_N = \frac{\hbar c}{2\pi^2} \int_{\omega_\pi}^{\infty} \frac{\sigma_\gamma^N(\omega) d\omega}{\omega^2}. \tag{1.9}$$

The Baldin Sum Rule has been re-evaluated in recent years for both the proton [Olm01] and neutron [Lev00], yielding[2]

$$\alpha_p + \beta_p = (13.8 \pm 0.4) \cdot 10^{-4}\,\mathrm{fm}^3 \tag{1.10}$$

$$\alpha_n + \beta_n = (15.2 \pm 0.5) \cdot 10^{-4}\,\mathrm{fm}^3. \tag{1.11}$$

1.3.3 Classical Model of the Deuteron

Since a free neutron target does not exist, it is useful to investigate photon scattering from the deuteron. The deuteron can be modeled in a similar manner to the individual nucleons (see Fig. 1.3).

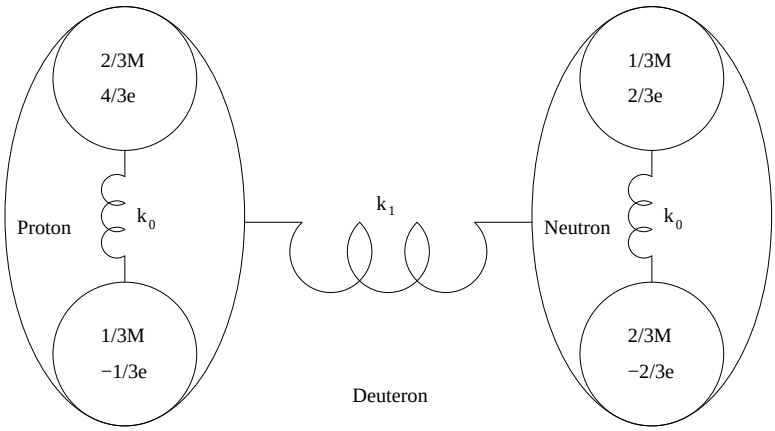

Figure 1.3: Classical picture of the deuteron in the mass-spring model.

[2]The units of 10^{-4} fm^3 will be assumed for all values of α and β from now on.

The deuteron cross section can be expressed qualitatively in terms of the proton and neutron scattering amplitudes (f_p and f_n respectively) as:

$$\frac{d\sigma}{d\Omega} = |f_d + f_p + f_n + f_{\mathrm{MEC}}|^2 \left(\frac{1+\cos^2(\theta)}{2}\right), \tag{1.12}$$

where f_d is the scattering amplitude of the photon from the deuteron and f_{MEC} is due to photons scattering from the mesons exchanged between the proton and neutron. It is impossible to calculate the effects of these meson exchange currents (MEC) on the photon scattering cross section in this classical model. Such treatment requires the full quantum calculations discussed at the end of this chapter. It is thus sufficient to realize that there are interference effects that arise from f_{MEC} and proceed.

Ignoring the effects of the MEC for now, the cross section in general terms is ([Luc94])

$$\frac{d\sigma}{d\Omega} = r_0^2 \left| 1 - \frac{\omega^2}{(\omega_1^2-\omega^2) - i\omega\Gamma_1} - \frac{2\omega^2}{(\omega_p^2-\omega^2) - i\omega\Gamma_p} - \frac{2\omega^2}{(\omega_n^2-\omega^2) - i\omega\Gamma_n} \right|^2 \left(\frac{1+\cos^2(\theta)}{2}\right), \tag{1.13}$$

where the nuclear resonance is defined by ω_1 and Γ_1. The energy of the nuclear resonance ($\sim$4.5 MeV) is much smaller than the nucleon resonance energies ($\omega_p = \omega_n \simeq 300$ MeV). This allows for scattering of photons in the region where $\omega_1 \ll \omega \ll \omega_{p,n}$. Using the proper approximations and the polarizabilities defined above, the cross section can be re-written as

$$\frac{d\sigma}{d\Omega} = (r_0^2 - 2r_0\omega^2(\alpha_p + \alpha_n)) \left(\frac{1+\cos^2(\theta)}{2}\right). \tag{1.14}$$

In this energy regime, the deuteron photon scattering cross section is more sensitive to α_n than the neutron scattering cross section (Eq. 1.6). However, in order to accurately extract the neutron polarizability, α_p must be well-known.

Combining the results of all the above work leads to several key elements useful for designing a deuteron Compton scattering experiment, which will be re-visited in the last section of this chapter:

- deuteron Compton scattering is sensitive to the isoscalar polarizabilities ($\alpha_s = \frac{1}{2}(\alpha_p+\alpha_n)$ and $\beta_s = \frac{1}{2}(\beta_p+\beta_n)$). Well-known proton polarizabilities are therefore essential to extracting the neutron values.

- the Baldin Sum Rule provides a constraint on $\alpha+\beta$ that is independent of any model or theory.

- the scattering cross section is constrained at forward angles, and even more so if the photon energies are well below pion threshold.

- the greatest sensitivity for extracting polarizabilities comes from back-scattered photons.

1.3.4 Estimate of α_p, α_n

The classical picture of the nucleons (Fig. 1.2) can be used to obtain an estimate of the electric polarizabilities. If an electric field is applied to the nucleon in this picture, the charges will separate, resulting in an induced dipole moment. By solving the equations of motion, the charge separation (and, therefore, the induced dipole moment) can be determined as a function of the applied field strength. As seen in Eq. 1.1, the constant of proportionality between the dipole moment and applied field is the polarizability, which in this case is given by

$$\alpha = \frac{q_{eff}^2}{4\,\pi\,\epsilon_0\,\mu\,\omega^2}, \tag{1.15}$$

where $q_{eff} = (q_1 M_2 - q_2 M_1)/\mathrm{M}$, $\mu = m_1 m_2/(m_1 + m_2)$, $\mathrm{M} = M_1 + M_2$, and $\omega^2 = \mathrm{k}/\mu$ is the resonant energy. Using the quark masses and charges and inserting a resonant energy of 300 MeV gives $\alpha \sim 13.4$ which is quite reasonable when considering current experimental values. The same polarizability is obtained for both the proton and neutron in this picture.

A full quantum theory is necessary to make accurate predictions about polarizabilities. However, it is still possible to make some qualitative assumptions about the nucleon polarizabilities in the non full-quantum limit. One method is to treat the nucleons as baryons surrounded by a pion cloud. In the simplest case, this models the proton as a combination of a π^+ and a neutron. Similarly, the neutron is viewed as the combination of a π^- and a proton. Here, one would predict that the neutron (two oppositely charged constituents) would have a larger electric polarizability than the proton (one uncharged constituent). This result can be seen by considering the nucleons as shown in Fig. 1.4 and using Eq. 1.15 which yields a value of α_n that is $\sim$30% larger than α_p.

While the pion cloud is the dominant component of the electric polarizabilities, the valence quarks contribute the most to the magnetic polarizabilities. The major contribution, at

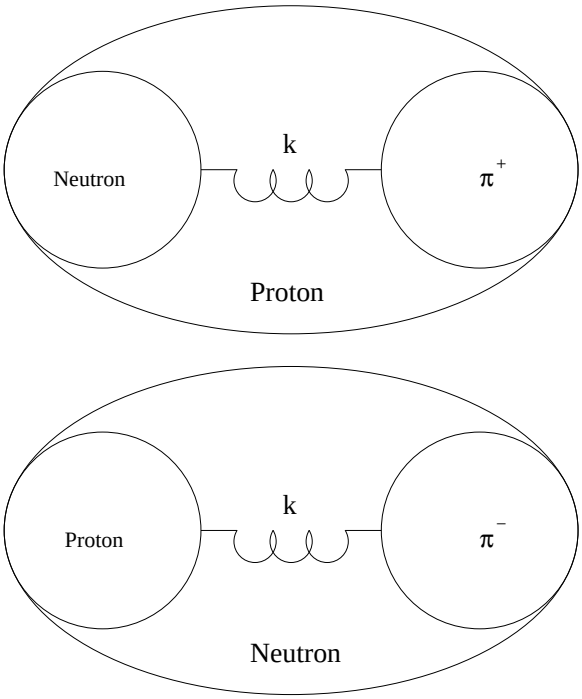

Figure 1.4: The proton and neutron as viewed in a classical mass-spring manner using the nucleon-pion cloud approach.

least to the paramagnetic term, comes from the $\Delta(1232)$-resonance excitation. Cancellation of the para- and diamagnetic polarizabilities is expected to result in $\beta \ll \alpha$ for the nucleons. The full theoretical framework, which is beyond the scope of this thesis, is needed to make more accurate statements about the magnitudes of the polarizabilities.

1.4 Current Experimental Status

1.4.1 Proton Polarizabilities

Measurements of elastic Compton scattering from the proton were conducted as early as the mid 1970's [Bar74], but it was not until the development of high duty factor, tagged photon beams that precise results became available in the early 1990's ([Fed91], [Zie92], [Mac95], and [Olm01]). As a result of improved photon beams, the cross section, and hence the extracted polarizabilities, have become more precise. This can be seen in the error contour plot (see Fig. 1.5) of α_p–β_p for all of the recent proton experiments.

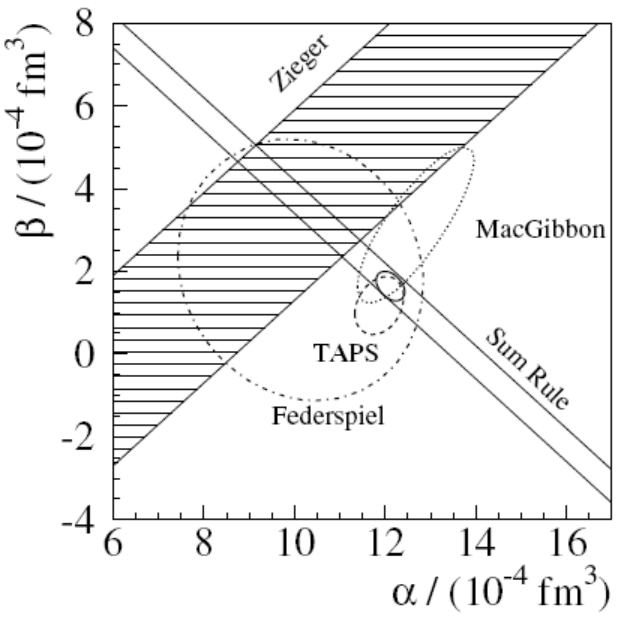

Figure 1.5: Error contour plot of the proton polarizabilities. The Baldin Sum Rule constraint is shown, along with results from the individual experiments. The solid ellipse is the global fit to all the data [Olm01].

The most recent global fit of all the data yields [Olm01]

$$\alpha_p = 11.9 \pm 0.5_{stat} \mp 0.5_{syst} \tag{1.16}$$

$$\beta_p = 1.5 \pm 0.6_{stat} \pm 0.2_{syst}, \tag{1.17}$$

which are in agreement with the Baldin Sum Rule stated above.

1.4.2 Neutron Polarizabilities

Attempts to measure the neutron polarizabilities started much later than the proton. This is because free neutron targets do not exist. The lifetime of the free neutron ($\tau_{1/2}$ ~10 min) is simply too short to allow for statistically significant experiments to be performed with current technology. Additionally, as seen above, the nucleon elastic cross section is dominated by terms that are proportional to the nucleon charge. Since the neutron has no charge, the cross section begins at $O(\omega^4)$ and is dependent on factors other than the polarizabilities. In short, even if a free neutron target were available, the small cross section

and presence of additional dependencies would make it nearly impossible to extract reliable values for α_n and β_n.

Despite these limitations, efforts began in the 1980's to measure the neutron polarizabilities. Unlike the proton where photon scattering has been used exclusively in an attempt to extract α and β, the neutron efforts have been more varied in technique with photon scattering being the most recent. These different approaches all have advantages and disadvantages.

Neutron-Nuclei Scattering The first efforts to obtain neutron polarizabilities were carried out by Schmiedmayer ([Sch88] and [Sch91]) and Koester ([Koe88] and [Koe95]). These experiments scattered a neutron beam off heavy nuclei via an interaction between the neutron electric polarizability and the electric field of the nuclei. This reaction is insensitive to the magnetic polarizability.

The most precise experimental value of α_n was reported to be 12.1 ± 2.0 [Sch91], but its quoted systematic uncertainties have been seriously questioned by [Eni97], and the results re-reported to be $7 \leq \alpha_n \leq 19$. Even with the large errors, this is still the most reasonable result from this set of experiments.

Quasi-Free Photon Scattering Starting in the early 1990's, experiments ([Ros90], [Kol00], and [Kos02]) were developed that could probe the neutron polarizabilities via photon scattering. These experiments made use of a deuteron target and the fact that a bound neutron is stable. The reaction

$$\gamma + d \rightarrow \gamma' + n + p \tag{1.18}$$

considers the neutron (or proton) to be a free particle sitting in a shallow potential well. The recoil neutron (or proton) is detected in coincidence with the scattered photon. The polarizabilities can then be extracted from the data.

This method was tested on the proton in an experiment at Mainz ([Wis99]). The ability to reproduce the polarizabilities from the proton scattering measurements seems to confirm the validity of extending the measurement to the neutron. To date, these experiments have typically been run near or above pion threshold. Since this reaction treats the neutron

as a "free" particle, it is necessarily subject to some of the issues discussed in detail in sections 1.3.1 and 1.3.2, namely a small absolute cross section (hence, the high photon energies) and dependence on factors besides α_n and β_n. These issues lead to both statistical and systematic/model uncertainties that are hard to minimize. The result is extracted polarizabilities with large error bars (see Fig. 1.7). Despite the initial interest, quasi-free photon scattering has fallen out of favor in part because of the difficulty with extracting polarizabilities.

Elastic Photon Scattering The last approach to measuring the neutron polarizabilities made use of the elastic scattering of photons from the deuteron ([Luc94], [Hor00], and [Lun02]). Like the quasi-free case, the stability of the neutron is critical to the feasibility of using the

$$\gamma + d \rightarrow \gamma' + d \tag{1.19}$$

reaction for the purpose of photon scattering experiments. As shown in section 1.3.3, scattering from the deuteron is more sensitive to α_n and β_n than scattering from a free (or quasi-free) neutron. The polarizabilities appear at $O(\omega^2)$ in deuteron Compton scattering but only at $O(\omega^4)$ in the case of scattering from the neutron. In addition, the cross section is much larger for deuteron Compton scattering than for neutron Compton scattering due to the interference between the proton and neutron scattering amplitudes. The larger cross section permits running the experiment at lower photon energies than those of the quasi-free photon scattering experiments without any loss of statistical precision. The high precision measurements of the proton polarizabilities permit accurate extraction of α_n and β_n from the isoscalar polarizabilities.

Despite the above advantages, there are effects that hinder the effort of obtaining high precision neutron polarizabilities from elastic photon scattering experiments. One disadvantage is separating elastically scattered photons from those that are scattered from the break-up of the deuteron. Since the break-up of the deuteron requires only 2.2 MeV, these inelastically scattered photons will have a very similar energy to the elastically scattered photons. In order to accurately obtain the Compton scattering cross section, the inelastic contribution must be either simulated ([Luc94]) or the photon detectors must have sufficient

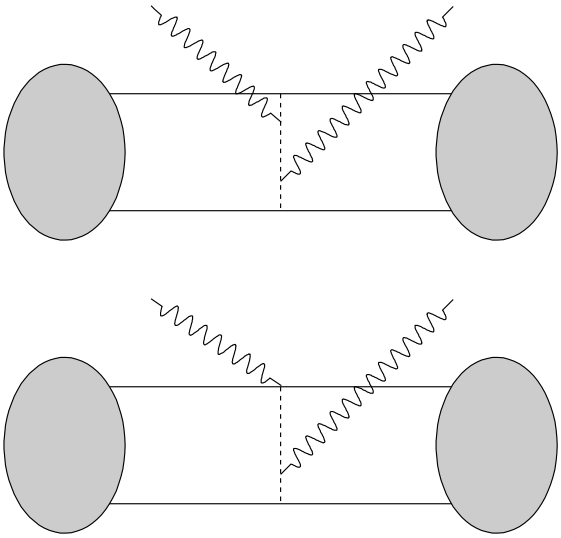

Figure 1.6: Two examples of a photon scattering from a deuteron via an interaction with a MEC between the proton and neutron.

energy resolution to separate the elastic and inelastic scattering ([Hor99]).

Beyond this technical limitation, the elastic scattering is complicated by potential scattering from MEC. In these instances, the incident photons scatter off the mesons exchanged between the proton and neutron. Several Feynman diagrams representing MECs are shown in Fig. 1.6. Theoretical models such as those described later in this chapter are used to account for the effects of the MECs on the scattering cross section. Without the development of these models, and the effective field theories in particular, it would not be possible to extract accurate values of the polarizabilities.

The values for the isoscalar electric polarizabilities ([Gri08]) extracted from the elastic scattering measurements are shown in Fig. 1.7 along with the values obtained from the quasi-free photon scattering and the result from [Sch91] with the re-analysis by [Eni97]. Furthermore, the data from [Hor99] were re-evaluated by [Bea03] using a next-to-leading order effective field theory. The current global value of the proton is also shown to highlight the discrepancy in the error bars. The extracted cross section from the deuteron Compton scattering experiments are shown in Fig. 1.8.

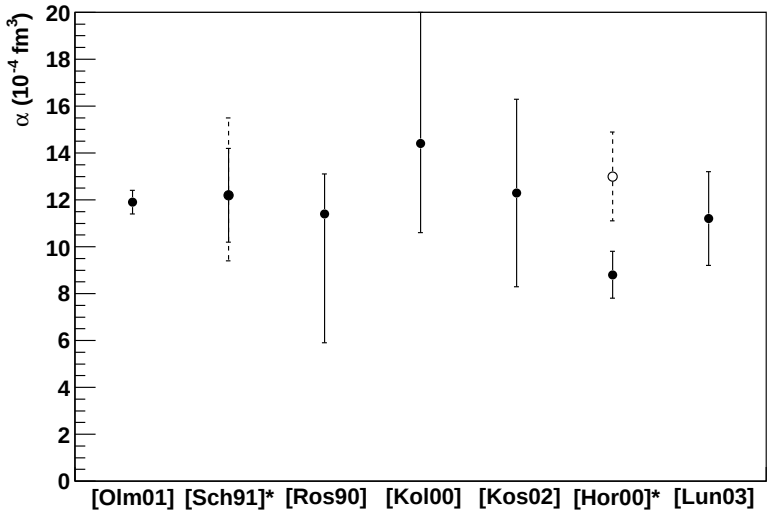

Figure 1.7: Current values of the electric polarizability from the proton, [Olm01], and the isoscalar polarizabilities from the measurements of neutron reactions. The results of the re-analysis of the data from [Sch91] and [Hor99] (by [Eni97] and [Bea03] respectively) are shown with the dotted lines.

1.5 Models and Theory

This section presents some current models and theories used for extracting the nucleon polarizabilities from the scattering cross section. The references are recommended for further details.

1.5.1 Dispersion Relations

A prediction for the scattering cross section and the neutron polarizabilities can be obtained by dispersion relations for the invariant amplitudes from a low energy expansion of the scattering amplitudes [Bab98]. The typical equation is

$$ReA_i(\nu,t) = A_i^B(\nu,t) + \frac{2}{\pi}\int_{\nu_{thr}}^{\infty} ImA_i(\nu',t)\frac{\nu' d\nu'}{\nu'^2-\nu^2} + A_i^{as}(t), \tag{1.20}$$

where A_i^B and A_i^{as} are the Born and asymptotic contributions to the scattering amplitude. The analysis of these integrals was carried out with the partial wave analysis code SAID developed by the VPI group [Arn96]. The values for the proton and neutron polarizabilities

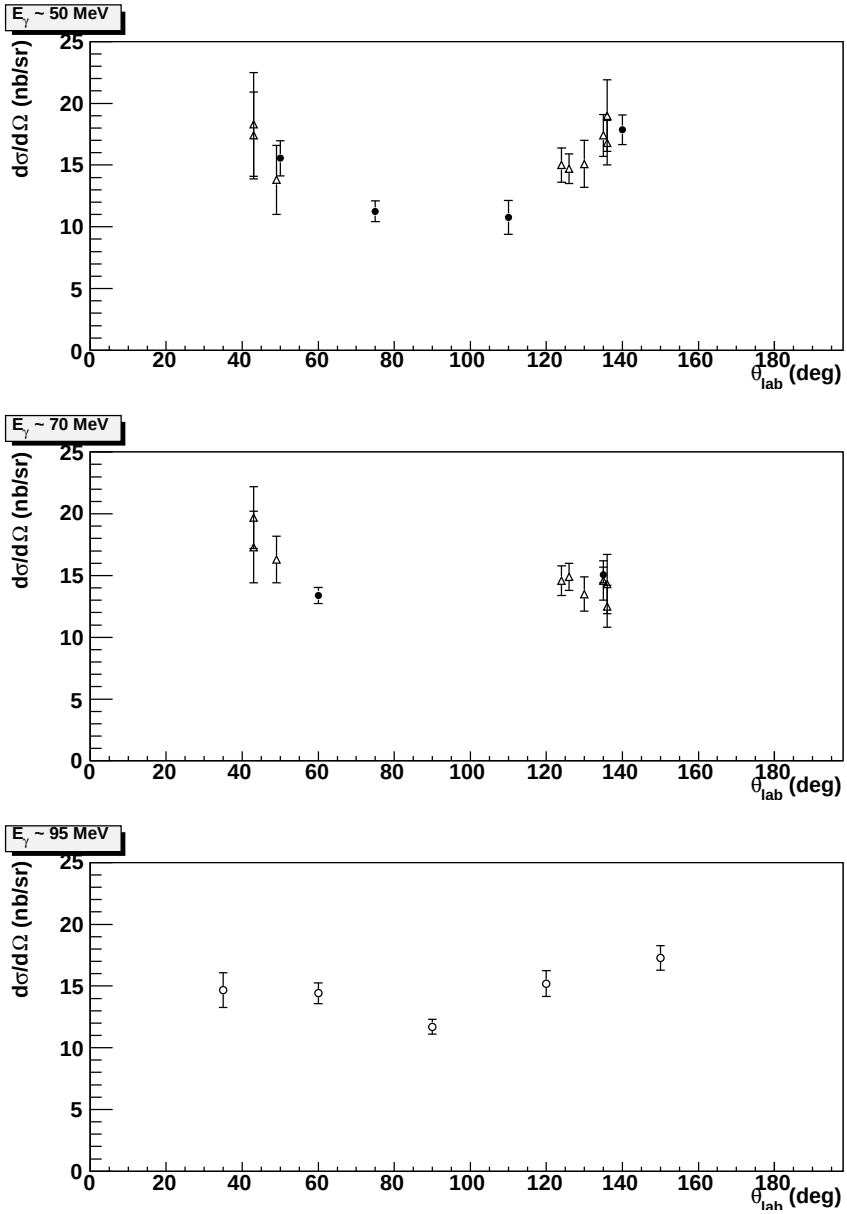

Figure 1.8: Cross section of deuteron Compton scattering as measured by [Luc94] (•), [Hor99] (○), and [Lun02] (Δ).

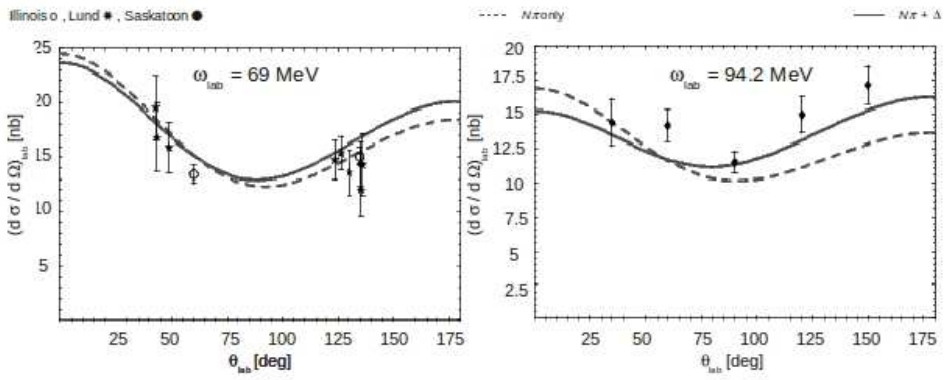

Figure 1.9: Comparison of the χPT theory with (solid) and without (dashed) the contribution from the $\Delta(1232)$-resonance. The data from [Luc94], [Hor99], and [Lun02] are shown as well. Taken from [Gri08].

are [Lvo97]

$$\alpha_p = 11.9\,,\ \beta_p = 1.9 \tag{1.21}$$

$$\alpha_n = 13.3\,,\ \beta_n = 1.8, \tag{1.22}$$

which agree very well with the current, precise experimental proton results.

1.5.2 Chiral Perturbation Theory

Chiral perturbation theory (χPT) is an effective field theory that utilizes an expansion in the parameter $P \equiv \frac{p,m_\pi}{m_\rho,4\pi f_\pi}$ ([Phi04]) of the QCD Green functions and exploit symmetries to ease the calculations. The leading order predictions depend on the pion mass, the nucleon axial coupling constant, and the pion decay constant. Other factors, such as the nucleon mass, do not appear until next-to-leading order terms. The predictions from [Ber94] are: α_p = 10.5$\pm$2.0 and α_n = 12.3$\pm$1.3. Again there is good agreement, but current uncertainties are too large to make a definite claim about these predictions.

χPT can also be used for extracting the neutron polarizabilities from the scattering cross section. The most developed model has been obtained by the inclusion of the $\Delta(1232)$-resonance ([Hil05]). Figure 1.9 ([Gri08]) shows the effect of the $\Delta(1232)$-resonance on the calculated cross section. Also shown are the appropriate data points for these energies. The development of the $\Delta(1232)$ contribution is essential to the theory replicating the backward-angle peaking in the cross section seen at higher photon energies. The current values for the

extracted neutron polarizabilities, with errors due to the deuteron wavefunction employed, are

$$\alpha_n = 14.6 \pm 2.0(stat) \pm 1.1(wf)\,,\ \beta_n = 1.4 \pm 2.2(stat) \pm 0.1(wf). \tag{1.23}$$

1.6 Motivation For This Experiment

Generally speaking, deuteron Compton scattering experiments have been motivated by a desire to probe the internal structure of the neutron and quantify the values of the fundamental structure constants α_n and β_n. This experiment ([Fel04]) was proposed with the same goals in mind. However, given the previous measurements, the aim was to extract the neutron polarizabilities with even better precision. Current results show α_n and β_n with errors 5-10 times larger than those of α_p and β_p.

Another goal was to measure the photon scattering cross section over a larger phase-space than the current data sets cover (see Fig 1.10). As seen in the phase-space plot, the data in this measurement will span angles and energies from the previous low energy results of [Luc94] and [Lun02] to the results of [Hor99] and continue to even higher energies. The reasons for this are two-fold: (1) the wide range of angles and energies will test the current theories and models in new ways and, (2) a full coverage of the phase-space, in addition to nearly doubling the number of data points, should result in extracted isoscalar polarizabilities with precision comparable to the proton values above.

Specific areas of focus/improvement for this particular series of experiments were:

- utilizing photon energies as high as 115 MeV to obtain maximum sensitivity to the polarizabilities and as low as 70 MeV in order to facilitate comparison with all the previously published data, to test the current effective field theories, and provide a substantial increase in data points to improve the precision of the extracted polarizabilities.

- using the SAL tagger and hodoscope and three large, high-resolution NaI photon spectrometers in order to separate the elastic and inelastic scattering peaks without resorting to Monte Carlo simulations.

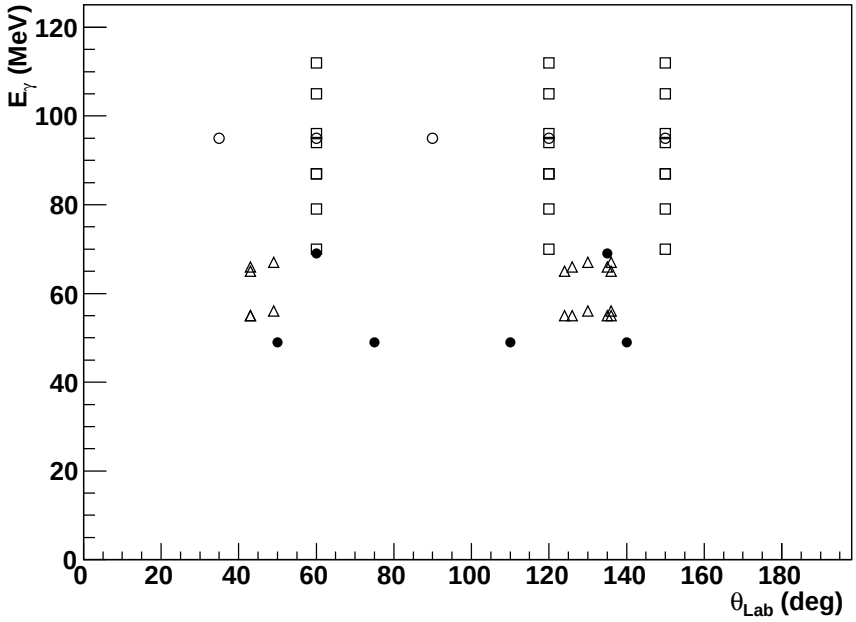

Figure 1.10: Phase-space plot showing the energies and angles of the deuteron cross section for [Luc94] (•), [Hor99] (○), [Lun02] (Δ), and this experiment (□).

- placing the NaI spectrometers at positions where the maximum solid angle could be obtained. The necessity for high statistics was considered more important than the effects of the scattering geometry (the extended target and the spectrometer acceptance) which can be calculated using Monte Carlo simulations.

- reporting of the cross section for energy bins that had a width of ±5 MeV instead of ±10 MeV as reported in [Hor99]. Narrower bins make the extraction of the polarizabilities more accurate.

- placing two of the NaI spectrometers at backward angle positions to take advantage of the enhanced sensitivity to the difference in the polarizabilities.

While not a part of the experimental program, recent developments of effective field theories since the most recent measurement of [Lun02], are necessary to the improved extraction of α_n and β_n from the cross section measurement. The precise proton measurement is also necessary to meet this condition.

2 Experimental Setup

2.1 Overview

This experiment was conducted at the MAX-lab National Electron Accelerator Laboratory in Lund, Sweden (see Fig. 2.1). It is one of the first experiments conducted after the recent upgrades to the injector and the nuclear physics tagged photon facility. The upgrade increased the available photon energies (now tagged up to and beyond 100 MeV) and, as a result, provided one of the main incentives to running this experiment at MAX-lab. This experiment was designed to measure the low absolute cross section (on the order of 10 nb/sr) with better precision and accuracy than the previous deuteron Compton scattering experiments. Such a plan requires obtaining a well-known incident photon flux and energy, a high electron rate, a high-density target, and sufficient energy resolution of the scattered photons in the photon spectrometers.

These goals were accomplished through the use of the SAL focal plane hodoscope [Vog93], a liquid deuterium target, and NaI photon spectrometers. Specific details of these elements are discussed in more detail below. The configuration of the electron and photon energies and the scattering angles for both the 2007 and 2008 run periods are shown in Table 2.1.

In addition to the topics above, a facility overview and a review of the data acquisition will also be covered in this chapter. First, though, is a brief synopsis of photon tagging.

Year	$E^0_{e^-}$	E_γ	θ_{lab}
2007	144MeV	66-97MeV	60^0(CATS), 120^o(BUNI), 150^o(DIANA)
2008	165MeV	82-116MeV	60^0(CATS), 120^o(BUNI), 150^o(DIANA)

Table 2.1: Electron energies, tagged photon energies, and scattering angles from each run period.

2.2 Photon Tagging

The process of photon tagging ([Car83]) is critical to extracting the Compton scattering cross section. In general, the cross section at a given photon energy (E_γ) is given by:

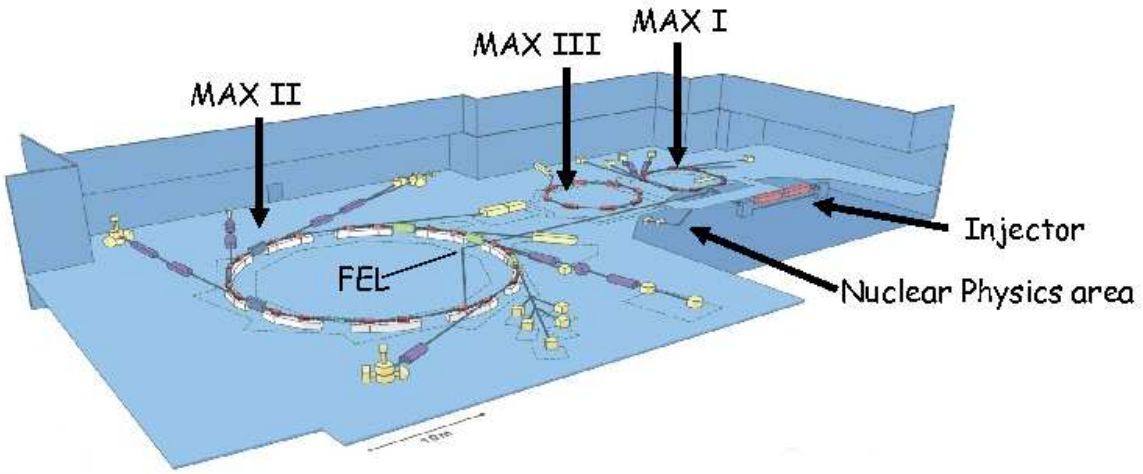

Figure 2.1: The MAX-lab facility showing the locations of the injector, MAX-I ring, and the nuclear physics area. Taken from [Sch08].

$$\frac{d\sigma}{d\Omega}_{E_\gamma} = \frac{1}{\kappa\Omega}\frac{N_{\gamma,scatt}(E_\gamma)}{N_{\gamma,inc}(E_\gamma)} \tag{2.1}$$

where κ and Ω are the target thickness and detector solid angle. The incident and scattered photon yields are given as a function of photon energy. The number and energy of the scattered photons are measured with dedicated photon spectrometers. In addition, photon tagging is used to determine the number and energy of the incident photons. The photon tagging is studied in two forms: calibration running and scattering running (Fig. 2.2).

2.2.1 Calibration Running

The incident photons are generated by electrons interacting with a metal radiator producing photons via bremstrahlung radiation. The post-bremstrahlung electrons and photons then pass through a magnetic field which deflects the recoil electrons while the photons continue on to the target. The magnet ("tagger") and a hodoscope of plastic scintillators are used to analyze the momentum of the electron via the field strength and the position along the focal plane that the electron strikes. Energy conservation is then used to determine the photon energy (E_γ) from the incident and recoil electron energies (E_0 and $E_{e'}$, respectively):

$$E_\gamma = E_0 - E_{e'} \tag{2.2}$$

This process provides a direct measurement of E_γ and also the number of photons by counting the corresponding electrons in each partition of the focal plane hodoscope.

The photons emerge in a cone which, projected forward to the target location, would subtend an area much larger than the target size. In order to restrict the beam size so that all photons entering the target room are incident on the target cell a collimator had to be inserted at the far side of the tagging spectrometer. This restriction imposes a geometrical constraint on the photons that necessarily leads to the condition where not all bremstrahlung photons are incident photons. The ratio of incident photons to bremstrahlung photons is called the "tagging efficiency" and is given by:

$$\epsilon_{Tag} = \frac{N_{\gamma,inc}}{N_{\gamma,brem}} = \frac{N_{\gamma,inc}}{N_{e'}}. \tag{2.3}$$

It must be mentioned that there are two other effects that could lead to electrons appearing in the hodoscope. These are multiple scattering of the recoil electrons within the metal radiator and Moeller (atomic electron) scattering. However, these are considered to be infrequent reactions (the radiator thickness is <1% of the mean free path of the electron and the Moeller scattering cross section is proportional to Z while the bremstrahlung cross section is proportional to Z^2). Also, these other electrons should be a constant fraction of the recoil electrons at a given energy and independent of the beam rate. Hence, any discrepancy will cancel out in the final cross section extraction.

To measure the tagging efficiency requires that a photon spectrometer be placed in the photon beam line and that the beam intensity be reduced to protect the detector. Figure 2.2(a) shows a schematic of the setup. The spectrometer is used to identify photons that pass through the collimator and would be incident on the target. The focal plane hodoscope counts electrons and "tags" them to determine energy. The tagging efficiency for each hodoscope partition (tagger channel) is then given by the ratio of photons in the spectrometer to electrons in the channel. With the accelerator setup used in this experiment the tagging efficiencies were typically 40-50%. For more details on the analysis see Section 3.4.

Since this was the first large-scale experiment conducted at MAX-lab after an accelerator upgrade there were concerns about the tagging efficiency being beam intensity dependent. A one-week run was conducted by the facility in the fall of 2007 and the tagging efficiency was

measured as a function of beam intensity from 10 Hz to ∼40 kHz electrons per hodoscope channel. The results of this test indicate that the tagging efficiency is indeed independent of the beam intensity [For10]. However, these rates are still only about 4% of the beam intensity in the scattering running. Further tests at higher beam rates were prohibited due to the space limitations between the exit window of the tagging spectrometer and the entrance face of the collimator.

2.2.2 Scattering Running

A schematic of the setup for running the scattering portion of the experiment is shown in Fig. 2.2(b). The photon spectrometer is moved out of the beam line and is looking toward the installed target. The beam intensity is increased to a nominal value of 1 MHz electrons per focal plane hodoscope channel. The spectrometer is used for detecting (scattered) photons and the hodoscope detects the number of recoil electrons. The tagging efficiency measured above relates the number of recoil electrons to incident photons without the need to physically detect the photons before they interact with the target. This allows for the cross section to be rewritten as:

$$\frac{d\sigma}{d\Omega}_{E_\gamma} = \frac{1}{\kappa\Omega}\frac{N_{\gamma,scatt}(E_\gamma)}{N_{\gamma,inc}(E_\gamma)} = \frac{1}{\kappa\Omega}\frac{N_{\gamma,scatt}(E_\gamma)}{\epsilon_{Tag}N_{e'}(E_\gamma)} \tag{2.4}$$

The need for high statistics measurements of the cross section, coupled with the low absolute cross section of Compton deuteron scattering, necessitate high electron rates in the focal plane hodoscope. The issues associated with these high rates will be discussed in chapter 3.

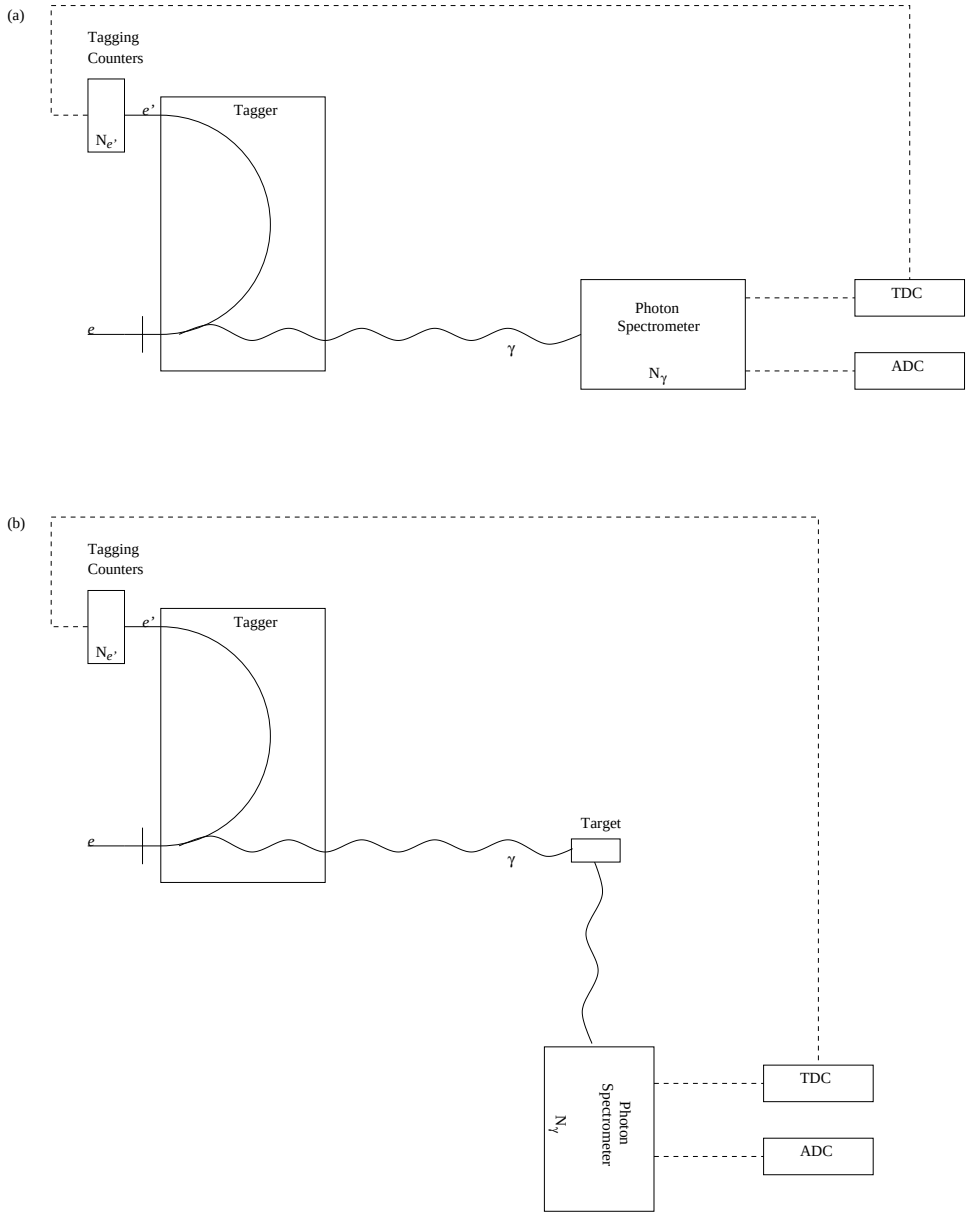

Figure 2.2: (a)Schematic diagram of the calibration running setup. The incident photons are counted by the photon spectrometer. The photon signal is passed on to the ADC to determine the photon lineshape and the TDC to measure the time difference between the photon and recoil electron in the hodoscope. (b) Schematic diagram of the scattering running setup. The incident photons interact with the target before scattering into the spectrometer.

2.3 The MAX-lab Facility

For photon physics, MAX-lab utilizes the MAX injector, MAX-I ring and the nuclear physics area. The nuclear physics area includes the tagger (the SAL magnet and hodoscope) and the target room which houses the target and detector systems.

2.3.1 Accelerator System

Electrons are created via thermionic emission in an RF electron gun which operates at 10 Hz and produces a beam pulse that is on the order of 100 ns wide. [Kum09] At this point the beam has a duty factor of 10^{-4}%. These electrons are pre-accelerated by an RF gun to 2 MeV. The electrons then enter the first of two 5.2m long linear accelerators (LINACs). Each LINAC has a maximum energy boost of 125 MeV; however, for nuclear physics applications, the maximum electron energy available is currently 205 MeV. For this experiment, the electron beam energy was 144 MeV for the November 2007 run period and 165 MeV for November 2008. During MAX-I usage, the beam is sent to the ring immediately after exiting the LINACs.

The MAX-I ring can be operated in one of two modes.

1) Storage mode: Used for synchrotron light experiments with a maximum operating electron energy of 550 MeV.

2) Pulse-stretching mode: Used for nuclear physics experiments providing a nearly continuous electron beam. After stretching, the electron beam duty factor has improved by more than five orders of magnitude to approximately 40-50%.

This experiment was conducted with the MAX-I ring in pulse-stretching mode. The electron beam is injected from the LINACs into the ring. The ring has a circumference of 32.4 m which the electrons navigate in approximately 108 ns. The beam typically winds around the ring twice and is then extracted over 100 ms at which time the next beam pulse is injected into the ring.

During operation, it has been observed that a small portion of the beam injected into the ring is immediately extracted without circulating. This "bad beam" pulse is rejected by 1) an abort kicker magnet which deflects the electrons out of the beam and 2) an inhibit signal sent

to the data acquisition electronics and synchronized to the extraction. This signal inhibits the acquisition for 1 ms after the extraction to prevent any data from the "bad beam" from being recorded in the acquisition file. The machine inhibit had the advantage that if the abort kicker failed the experiment could continue.

The beam intensity in the ring was typically 10-20 mA for this experiment. This resulted in a measured current of 10-20 nA in the Faraday cup in the nuclear physics area.

2.3.2 Tagger Magnet

The layout of the tagger, hodoscope, and target rooms is shown in Fig. 2.3. The paths of the electron and photon beams are indicated, as well as the positions of the SAL hodoscope and photon spectrometers.

The extracted, mono-energetic electron beam was transported down a beam pipe and then directed toward the tagging spectrometer by a 50 degree bending magnet where it is incident upon a radiator, typically a thin metal foil. The geometry of the beam pipe and the magnitude of the field in the bending magnet provide an independent measurement of the electron beam energy; this independent calculation always agreed with the energy quoted by the accelerator operators.

The technique of bremstrahlung-tagging discussed above is employed to obtain a quasi-mono-energetic photon beam. For this experiment, a 300 μm Al foil was placed inside the radiator chamber. This foil radiator produces bremstrahlung radiation by interaction between the electrons and the Al nuclei.

The tagging magnet used in this experiment was originally used at the Saskatchewan Accelerator Laboratory (SAL) [Vog93]. The schematic of the diagram is shown in Fig. 2.4. Its purpose was two-fold. First, the primary (non-interacting) beam of electrons were bent, with the aid of a second dump magnet, into a Faraday cup which, by integrating this beam current, provided a measure of beam stability. Secondly, the tagger uses a magnetic field (of a dipole character) to focus the recoil (interacting) electrons of the same momentum to the same channel in the the focal plane hodoscope.

As discussed in Section 2.2, a collimator was placed in the photon beam line to reduce the beam size at the target location. This collimator is located $\sim$10 cm downstream of the exit

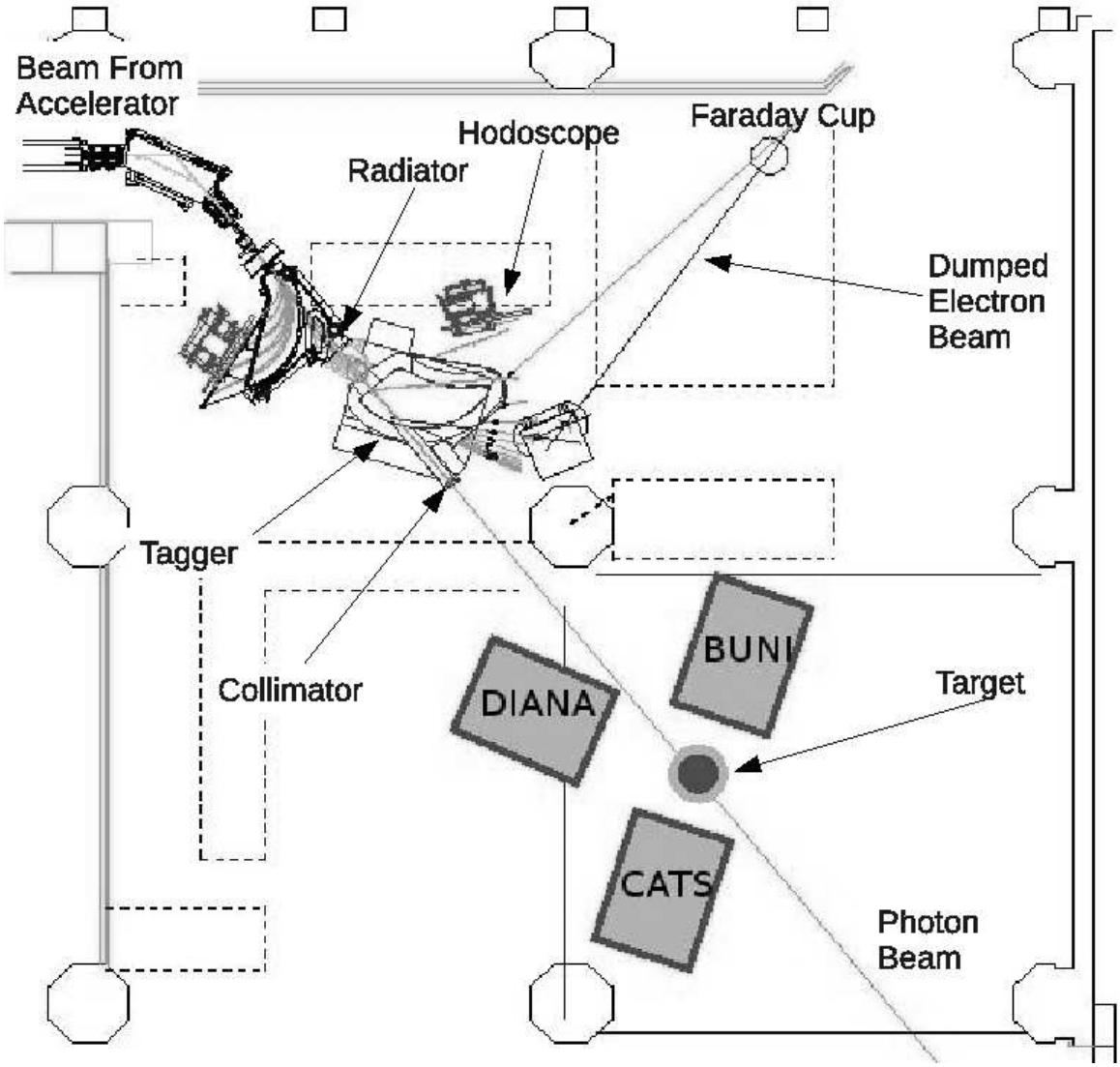

Figure 2.3: Diagram of the setup for this experiment at the MAX-lab facility. The location of the NaI spectrometers and the scattering target are indicated. The bremstrahlung photon beam that emerges from the collimator is shown also. The shielding walls are represented by the dashed lines.

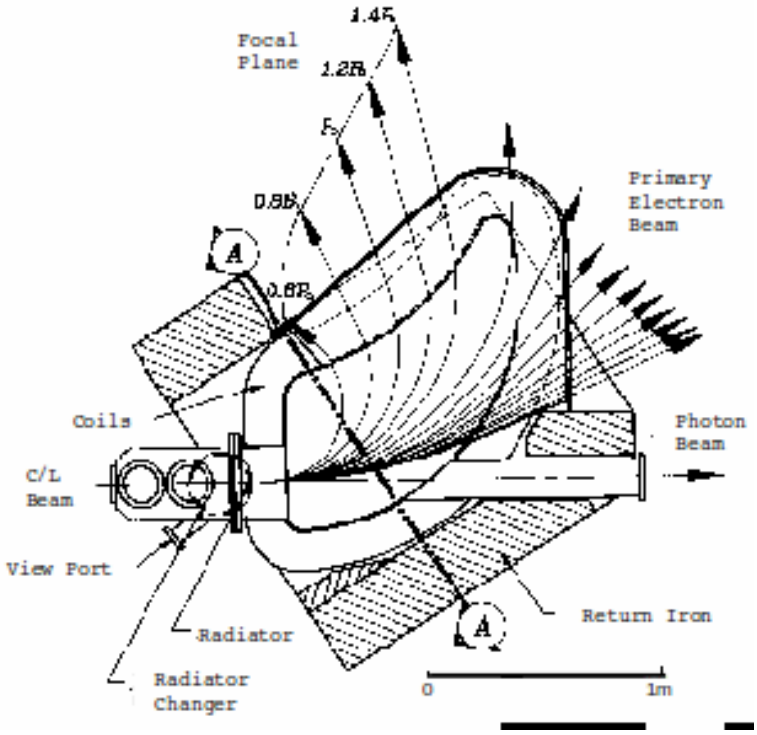

Figure 2.4: Schematic of the SAL tagger magnet. The photon beam continues to the right, while the recoil electron beam is bent toward the hodoscope. The non-interacting (primary) electron beam is deflected toward the beam dump. Figure taken from [Vog93].

window in the tagging magnet assembly. The photon beam collimator assembly is composed of a heavy metal (an alloy of tungsten, copper and nickel) main collimator with an 18.92 mm entrance diameter, 19.94 mm exit diameter, and a length of 108.5 mm. A scrubber magnet sits immediately downstream of the main collimator and is used to deflect any stray charged particles away from the photon beam. This magnet is 200 mm long with a 25.48 mm diameter aperture (see Fig. 2.5). A plastic collimator, 100 mm thick and with a 40.0 cm diameter, sits just downstream of the magnet.

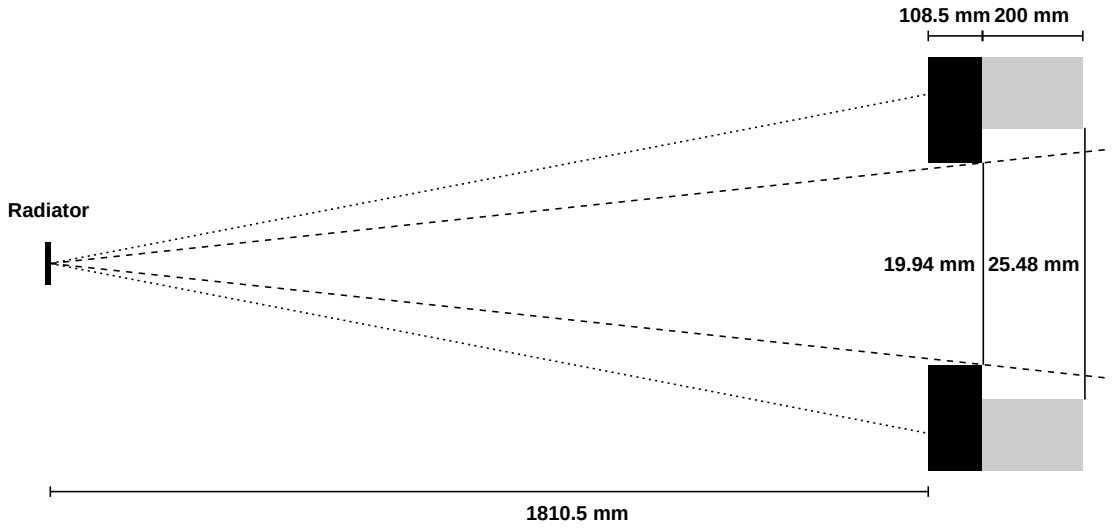

Figure 2.5: The collimator assembly: Photons emerge in a cone from the radiator and either strike the collimator (dotted) or enter the target room (dashed). The beam collimator (black) and scrubber magnet (gray) are shown.

2.3.3 SAL Hodoscope

Like the tagging magnet, the hodoscope used for this experiment was also developed and used at SAL. The SAL hodoscope [Vog93] used for tagging the recoil electrons consists of 63 plastic scintillators (3 mm x 25 mm x 50 mm) arranged in two rows. The back row was offset from the front by ∼50% of the scintillator width. This overlap, which defines a tagger channel, provides ∼300-500 keV of energy resolution in both the recoil electron and the tagged photon. The average electron rate in any tagger channel was on the order of 1 MHz for this experiment. A schematic of the hodoscope is shown in Fig. 2.6.

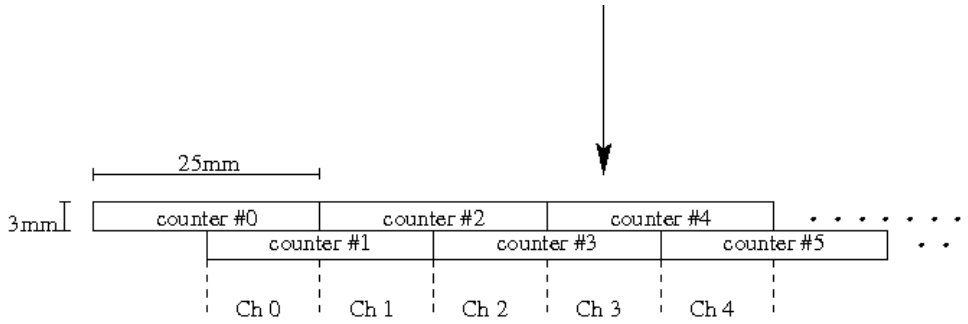

Figure 2.6: Schematic of the SAL focal plane hodoscope showing the dimensions of the plastic scintillators. The electron channels are defined by the overlap between successive counters. Electron paths are indicated by the arrows.

2.3.4 Target Room

The target room is heavily shielded from the tagger and SAL hodoscope, in effect separating the electron and photon beams. The liquid deuterium target and its cooling system, the other targets, and the photon spectrometers are housed in this area. Details of the targets are explained in the next section. Four photon spectrometers were employed throughout the experiment. Of these, three were the large NaI detectors mentioned previously. The fourth was a lead glass (PbGl) detector used solely in calibration mode for beam monitoring. Specifics of each spectrometer are discussed individually later in this chapter.

2.4 Targets

The data collected for this experiment were taken primarily from a liquid deuterium target housed in a Kapton cell. A pure Kapton target was used for determining any contributions from the cell material. Additionally, carbon and lead targets were used for setting up the electronics, but only the carbon was analyzed for the purpose of extracting a scattering cross section.

2.4.1 Liquid Deuterium Target

The liquid deuterium cryogenic target used for this experiment is a modified version of the system used in previous measurements at MAX-lab ([Lun02]). Schematic diagrams of the target system is shown in Figs. 2.7 and 2.8. The heat exchanger is powered by a DE-204SL

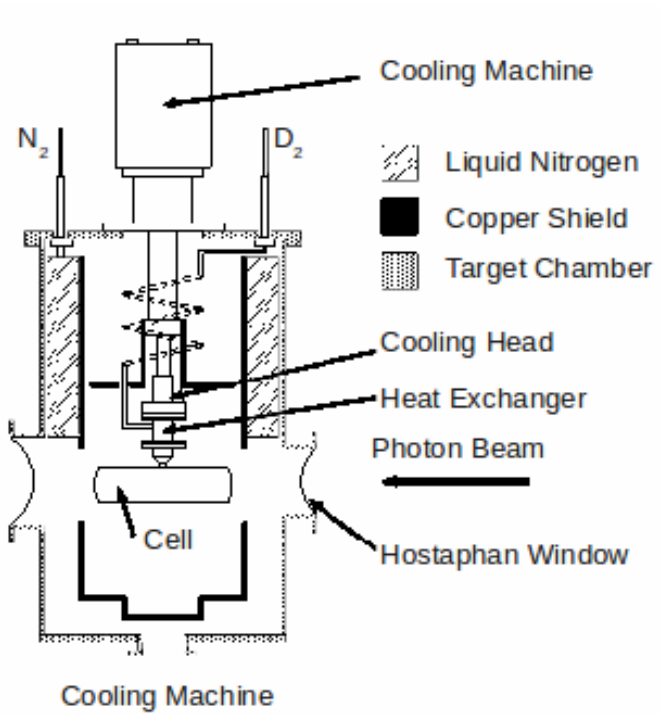

Figure 2.7: Schematic diagram of the liquid deuterium target showing the cooling head, housing, and copper and nitrogen shields. The direction of the incoming photons is also indicated. [Lun02]

cooling head with an HC-4 compressor from SHI-APD Cryogenics. The deuterium gas is liquefied and drips into the target cell. The cell itself is made of 120 μm thick Kapton. The cylindrical portion is 150 mm long and has a diameter of 68 mm. There are two, pressed spherical end caps that bring the total length of the cell to 170 mm. This cell was housed in a 1.0 mm thick stainless steel housing. Two thin windows allow the incident photon beam to enter and exit the cell with minimum interaction.

In the previous MAX-lab experiment this target system had issues with ice forming on the target end caps. This experiment took efforts to avoid any ice build-up ([Han07]). The target was constructed of thicker Kapton to prevent the diffusion of water molecules. To further eliminate water vapor a shield of nitrogen gas was made against the vacuum windows by using the return from the liquid nitrogen shield. The liquid nitrogen was refilled daily which ensured that this shield did not lessen over time. The vacuum vessel was baked out at 60°C prior to the run period and was isolated by means of a high-vacuum gate-valve so

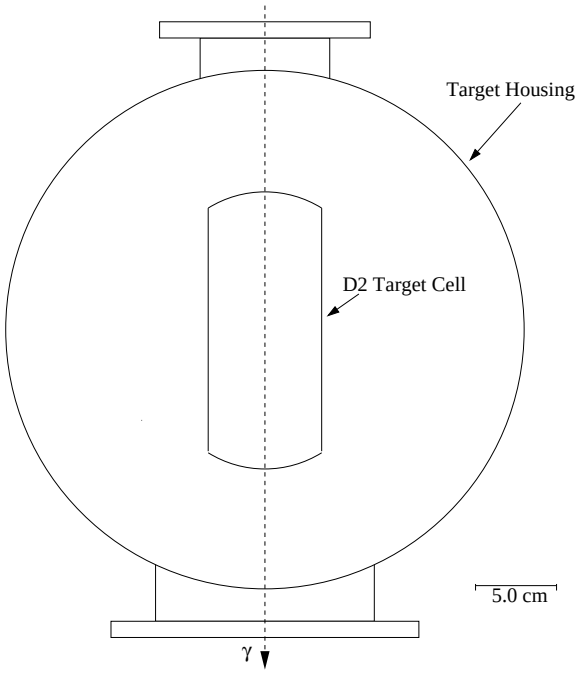

Figure 2.8: Liquid deuterium target cross section in scattering plane [Han07]. The target cell is 170 mm long, 68 mm in diameter with a wall thickness of 120 μm. The housing wall is 1 mm thick in the scattering plane and has a diameter of 320 mm..

that the target could be positioned without losing vacuum. As a result of these steps, no ice build-up was observed during this experiment.

The target cell was filled at the beginning of the run period and was monitored throughout the experimental program to ensure that the liquid level did not change. The cooling machine, as a temperature control system, employed a resistor heater and a calibrated diode to measure the cooling head temperature. Additionally, the pressure in the target cell was monitored. The pressure as a function of run number is shown in Fig. 2.9. By using these data, the condition of the target could be verified throughout the running. Furthermore, Polaroid photos of the target were used as a last monitor of the target stability. During times of filling and emptying, the liquid level line was quite visible. Daily photos confirmed that the target level did not change day-to-day.

During the November 2007 run period the superinsulation came loose and made contact with the liquid nitrogen shield. As a result, the target cell was not able to fill completely. The amount of unfilled target was roughly 15%, but this effect is taken into consideration

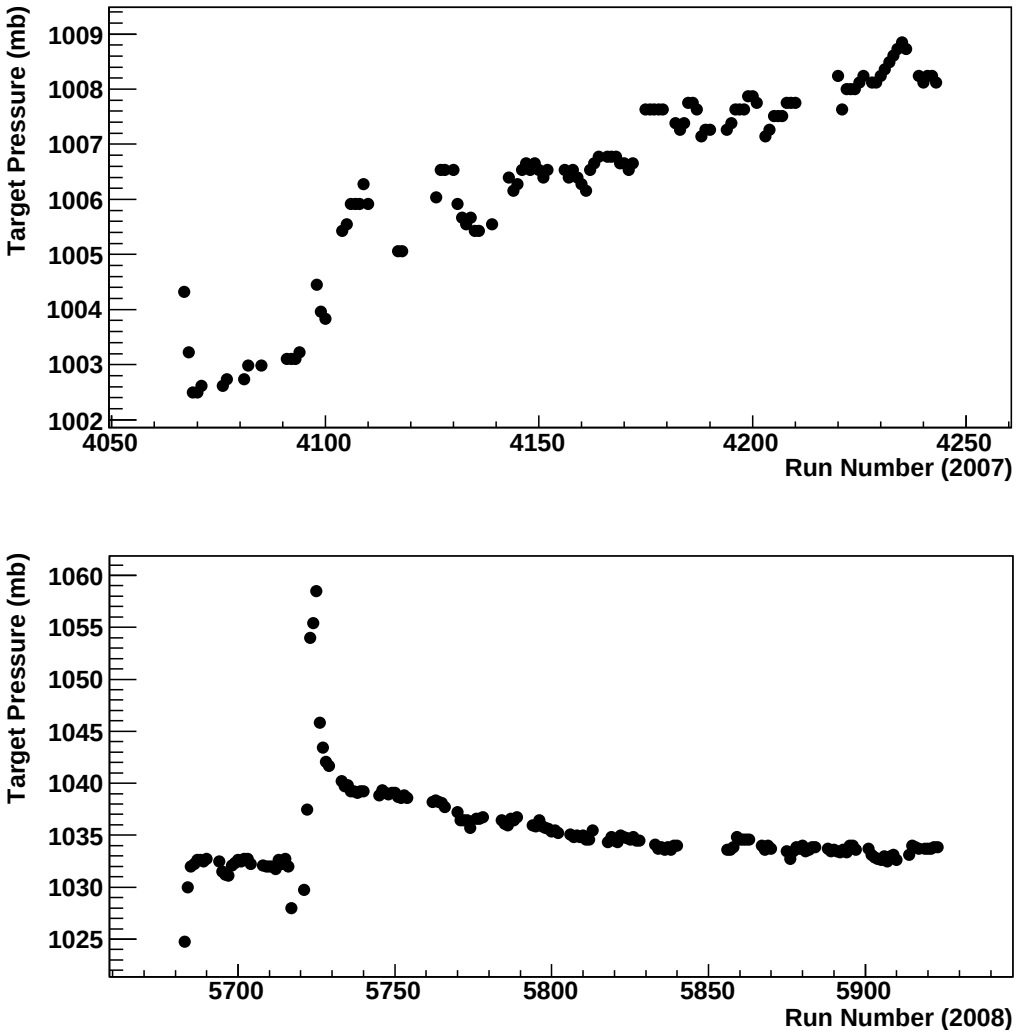

Figure 2.9: Pressure reading of the liquid deuterium target as a function of run number for the 2007 (top) and 2008 (bottom) run periods.

during the data analysis. The target filled completely during the November 2008 run period.

2.4.2 Kapton Target

In the past, experimenters have run for nearly equal times with the target cell full of deuterium and empty in order to measure the background due to the cell. However, in order to maximize beam time on deuterium and due to the relatively long ($\sim$ one day) warming/liquefying cycle of the Lund target, a pure Kapton target was employed for this experiment. This "dummy" target consisted of 107 (Nov 2007) or 200 (Nov 2008) Kapton sheets, 80 μm thick. The target was placed at the target center position and data were collected for one experimental shift. These data were then normalized and used to make necessary corrections to the deuterium yields.

2.4.3 Other Targets

A block of graphite 5.22 cm thick was used to (1) determine the functionality of the experimental setup, both detectors and acquisition, and (2) to establish the ability to extract an absolute cross section from the MAX-lab setup. Given that the carbon cross section is more than an order of magnitude larger than deuterium these data could be collected in 1-2 days without compromising the main goal of the experiment.

Occasionally, lead targets (1-3 mm thick) were placed in the beam to verify the timing of the electronics. These data were used only as a diagnostic and were never fully analyzed.

2.5 Photon Spectrometers

The success of this experiment depended primarily on the ability to accurately measure the photon flux and the number and energy of the scattered photons; hence, it was essential that quality detectors be used. Individual characteristics of these detectors are discussed below.

2.5.1 BUNI

The BUNI (Boston University Sodium Iodide) spectrometer ([Mil88]) was lent to MAX-lab by Boston University. It is composed of five NaI(Tl) crystals. The core is a cylinder

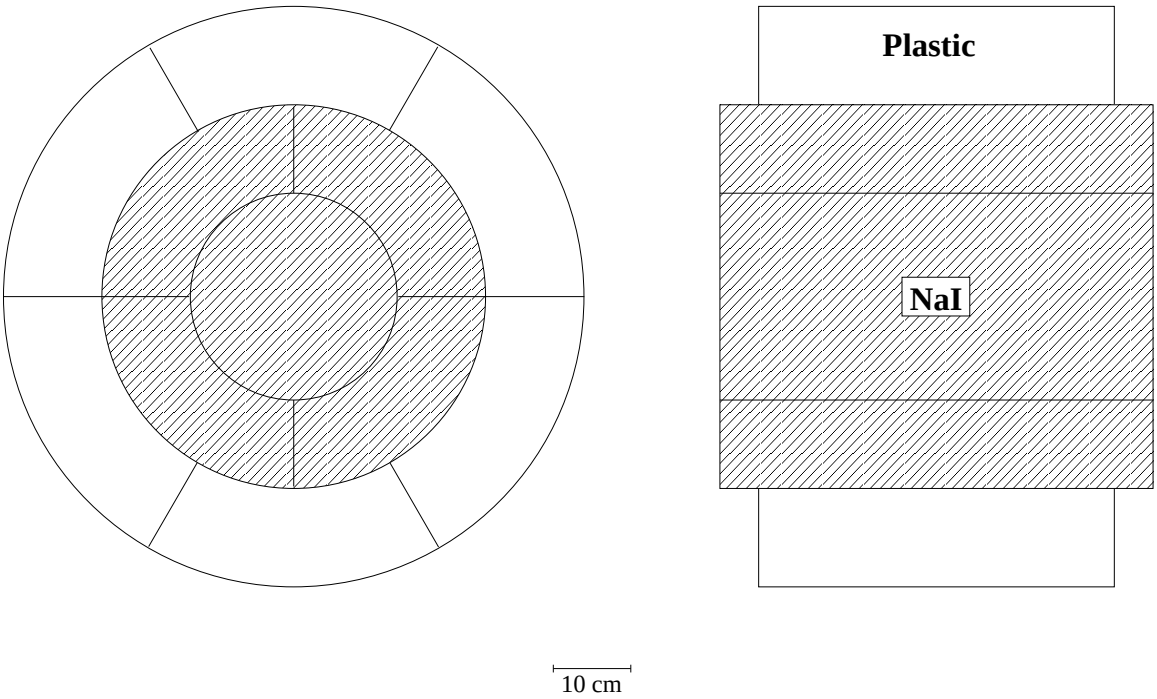

Figure 2.10: End (left) and side (right) view of the BUNI detector. Only the NaI portions are shown at proper scale. The charged particle veto and lead shielding have been omitted.

measuring 26.7 cm in diameter and 55.9 cm in length. Surrounding the core are four optically isolated annular segments. Each segment has a thickness of 11.4 cm and length of 55.9 cm. Finally, six annular segments of BC-400 plastic scintillator, 12.7 cm thick, encase the NaI crystals. This shield acts as a cosmic ray veto. The detector is the then shielded from the room by 10 cm of lead with a 15 cm diameter aperture. A 5 mm thick plastic scintillator paddle was installed in front of the shielding aperture to act as a charged particle veto. Side and end view diagrams of the BUNI detector are shown in Fig 2.10.

2.5.2 CATS

CATS (Compton And Two photon Spectrometer) ([Wis94]) is on permanent loan to MAX-lab from Mainz. Its size and construction is very similar to BUNI. CATS is composed of seven pieces of optically isolated NaI(Tl) crystals. The central core has a diameter of 26.7 cm and a length of 63.5 cm. This piece is surrounded by six, 10.8 cm thick annular segments. Surrounding the annular segments is a 1 cm layer thick of $^{6}Li_2CO_3$ and then five annular

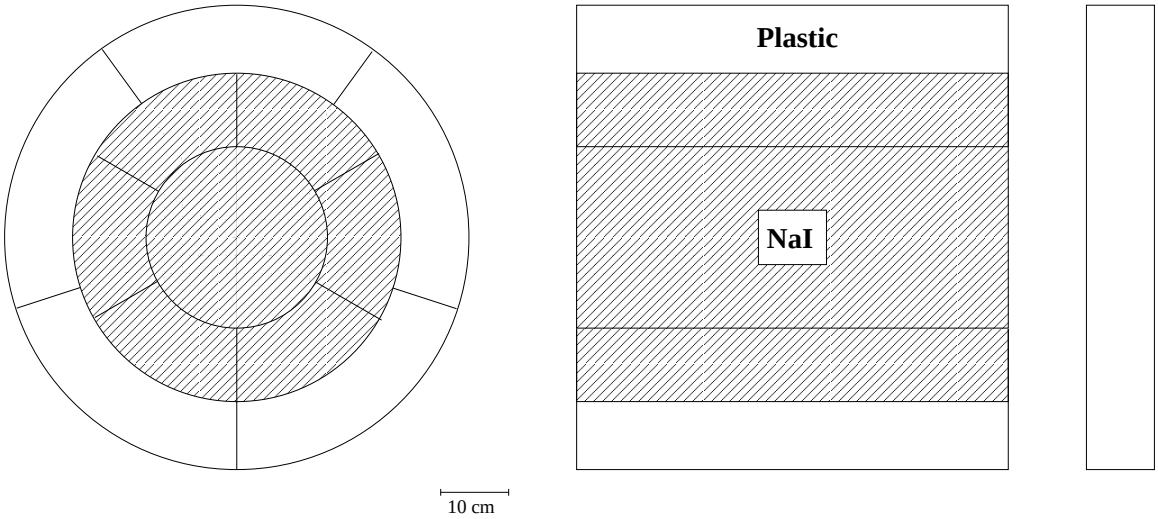

Figure 2.11: End (left) and side (right) view of the CATS detector. Only the NaI portions are shown at proper scale. The charged particle veto and lead shielding have been omitted.

segments of plastic scintillator 10 cm thick. A circular plate of plastic scintillator covers the back end of CATS. The scintillator shield is used as a cosmic ray veto. The detector is then encased is 10 cm of lead. An inner, tapered collimator was installed with a 13.8 cm diameter defining aperture. Finally, a 5 mm thick plastic scintillator paddle is placed over the aperture in the lead shield to act as a charged particle veto. Side and end view diagrams of the CATS detector are shown in Fig 2.11.

2.5.3 DIANA

DIANA (Detector of Iodine and Sodium) ([Kov08]) is currently on loan to MAX-lab from the University of Kentucky. While similar in overall size and composition to the other two NaI detectors it differs markedly in construction. DIANA consists of a single NaI(Tl) core crystal 48 cm in diameter and 51 cm long. Surrounding the core are two, optically isolated cylinders of NaI(Tl) each 4 cm thick. Each cylinder is segmented annularly into six pieces resulting in an annulus with twelve total pieces. This annulus is used for cosmic ray vetoing. The entire assembly is then shielded by 10 cm of lead to prevent any room background from entering the detector. Six, 6 mm thick pieces of plastic scintillator are arranged to provide coverage of the top of the detector and its front and back faces. These scintillators are used for charged particle and cosmic ray rejection. Side and end view diagrams of the DIANA

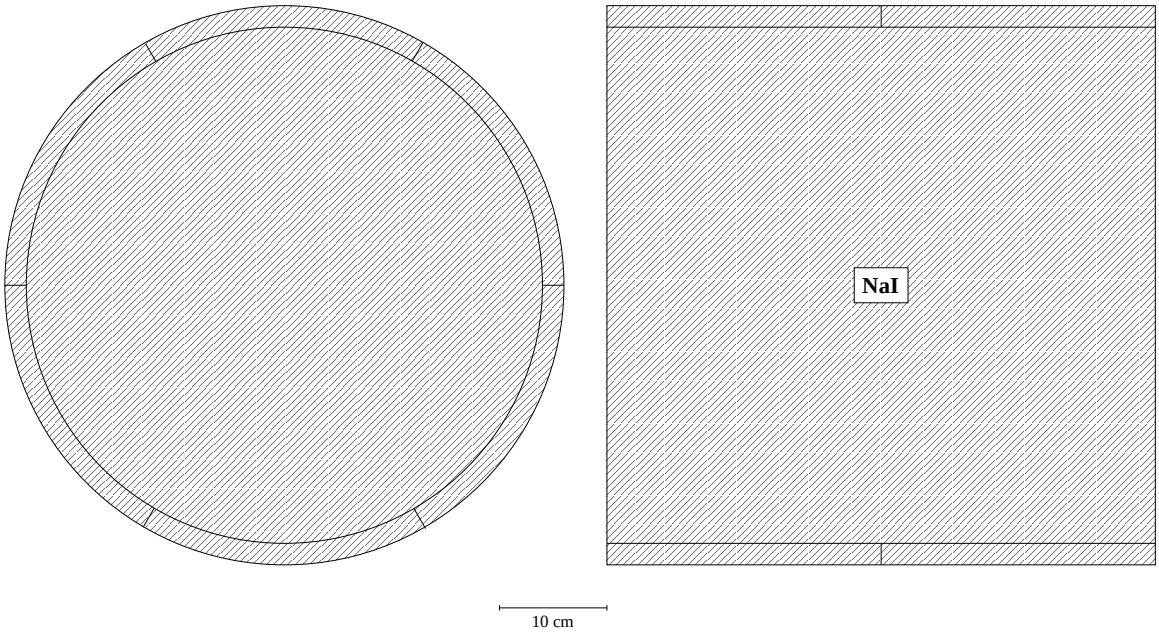

Figure 2.12: End (left) and side (right) view of the DIANA detector. The charged particle vetoes and lead shielding have been omitted.

detector are shown in Fig 2.12.

2.5.4 Pb-glass detector

A Pb-glass detector, measuring approximately 258 mm x 230 mm x 235 mm, was kept in the target room. It was surrounded by 10 mm of Al on the sides and 15 mm of Al on the front and back. The detector was mounted on a hydraulic lift so that it could be raised into the beam line for the daily tagging efficiency measurement and then lowered out of the way to return to scattering mode. It was not used in collecting any of the elastically scattered photons due to its poor energy resolution.

2.6 Data Acquisition

2.6.1 The Computer Setup

The data acquisition (DAQ) program is based on a PCI-VME bus-adapter system run. It was run on a linux PC (Mandrake 9.2) based on ROOT ([Roo10]), a source code developed

at CERN and used extensively at MAX-lab. The DAQ is instrumented with CAMAC and VME modules as shown in Fig. 2.13 ([Lun05]). Modules used were ADCs (charge-to-digital converters), TDCs (time-to-digital converters) and scalers. The scalers were used to count the number of events within a given detector. The ADCs were connected to the PMTs from the photon spectrometers and provide information about the energy deposition of the photons. The TDCs are used to measure the time difference between the start signal from the trigger source and the stop signal from the detector. Two types of TDCs were used: single-hit (which record only the first stop after the start) and multi-hit (which record several stops after the start).

The multi-hit TDCs were not suitable for extracting yields. The time resolution between the start and stops was 25 ns – too poor for analysis purposes. The time resolution between any two channels is only 100 ps, though. In order to achieve this resolution, a copy of the start signal had to be delayed and sent into a stop. However, the added delay was not sufficient to guarantee that the copied signal was always recorded. As a result, approximately half the events do not have the high resolution timing. For this reason, the multi-hit TDCs were not used in the extraction of the photon yields. They did prove useful in constructing a simulation of the electron beam and tagger hodoscope (as discussed in Appendix C).

2.6.2 Electronics Setup

A schematic of the trigger is shown in Fig. 2.14 and of the electronics setup in Fig. 2.15. The trigger signal opened the DAQ latch at which time the computer read out all the ADC and TDC modules in the CAMAC and VME crates. The ADC and TDC modules were read out for each trigger. The scaler modules are read out and cleared at pre-determined intervals (nominally every two seconds). This 0.5 Hz readout rate allowed for near real-time diagnostic abilities while minimizing the dead time in the system . The only hardware coincidence is made between the trigger signal and the signal for "good beam", which is defined as any portion of the beam occurring one millisecond or more after the extraction of the electron beam from the MAX-I ring.

The experiment is run with two types of triggers:

1) FP triggers – The data acquisition is started by an electron in any one of the tagger

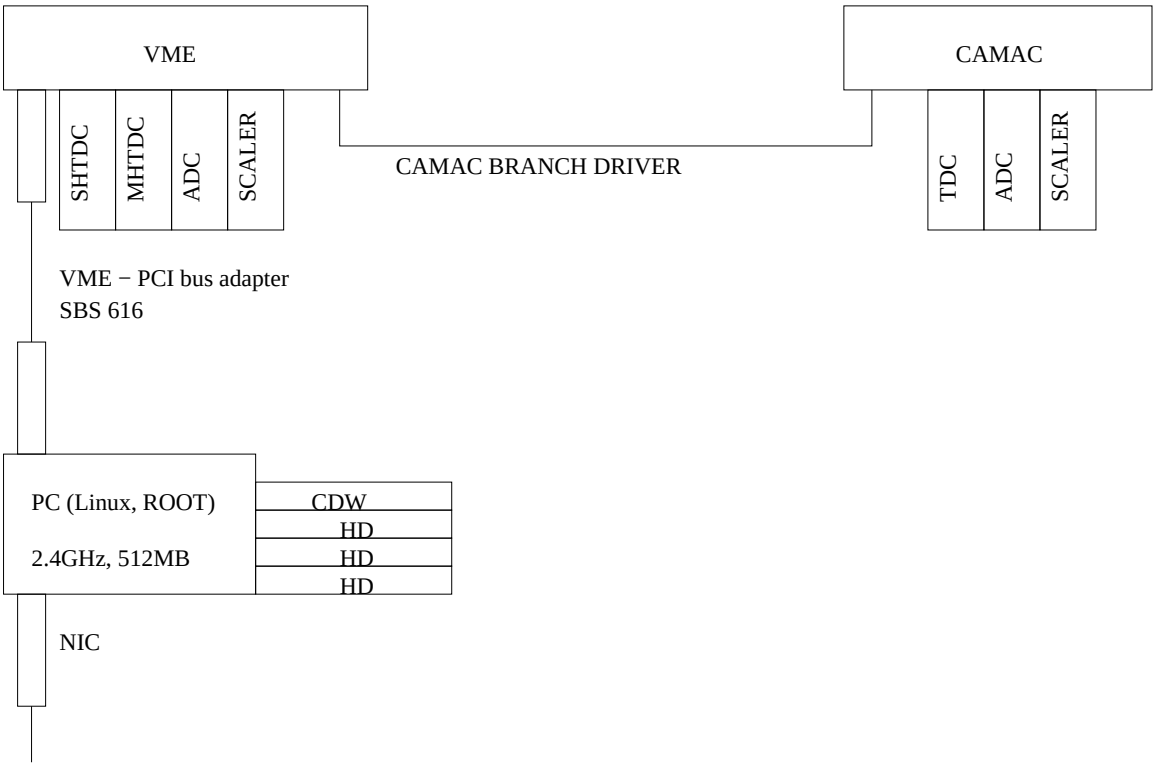

Figure 2.13: Schematic of the data acquisitions system (DAQ). The CAMAC and VME modules used are indicated as well as the branch driver that feeds into the acquisition PC.

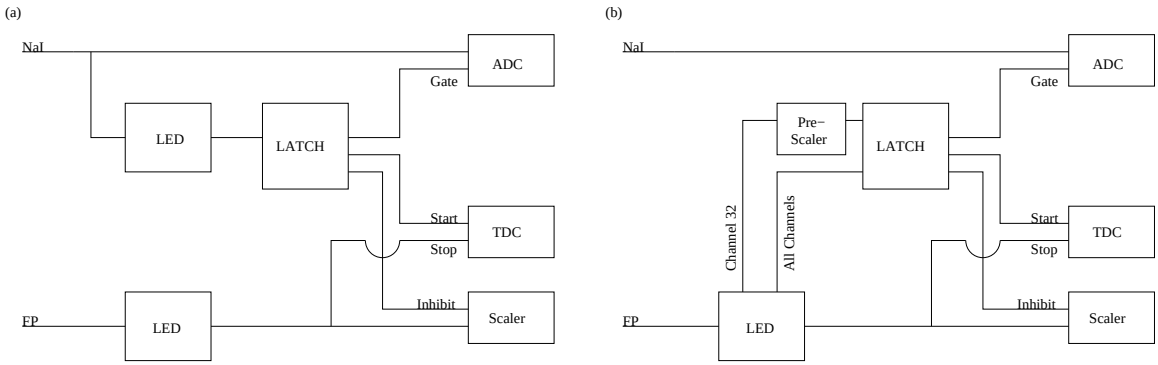

Figure 2.14: Overview of the trigger electronics. (a) For the singles trigger, which is generated by the NaI detectors, the signal is processed by a discriminator and then sets the latch for the DAQ. (b) For the focal plane hodoscope (FP) triggers, either summed over all channels or just one, the signal from the discriminator is pre-scaled and then sets the latch. In either case, once the latch is set the DAQ reads out the ADCs, TDCs, and scalers.

channels. A pre-scaler was used to reduce the number of triggers coming from the hodoscope. Due to the low electron rates required for safety when a detector is in the beam, the pre-scale factor could be set to one and the OR of all channels used to form the trigger. However, the high electron rates used in scattering mode would overwhelm the DAQ without a change to the pre-scaler. Here, data were collected by triggering on one channel only and keeping the pre-scaled event rate to $\sim$10 Hz in scattering running. The pre-scale factor could be adjusted as necessary but was typically on the order of 100,000. This pre-scaled trigger would prove useful in making corrections that arise due to rate-dependent effects.

2) Singles trigger – The data acquisition is started by an event occurring in any one of the photon spectrometers. Most of the time, the trigger signal came from the core of the spectrometer. At times, though, the trigger would be changed so that an event in another part of the detector would start the DAQ. This is most commonly done for the Th-C source calibrations discussed in the next section. The singles trigger is used in both calibration mode and scattering mode.

Employing both types of trigger setups during the calibration period allowed for cross checks of their validity. Once identical results were obtained from each method the DAQ was considered ready for production data collection.

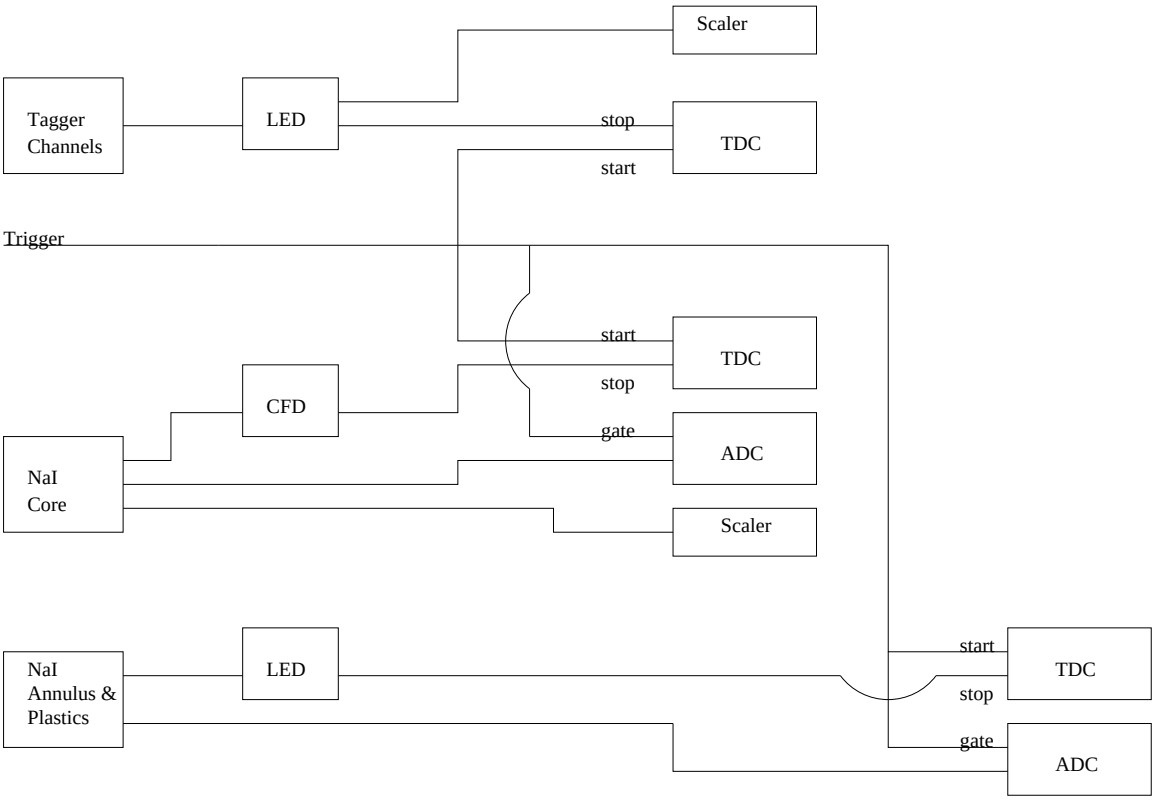

Figure 2.15: Schematic drawing of the electronics setup for this experiment. The NaI and tagger channel signals are sent to scalers and TDCs and the NaI signals are also sent to an ADC. The trigger signal is one processed in Fig. 2.14.

2.6.3 Running Modes

The experiment has several forms of operation. These are

1) calibration mode,

2) tagging efficiency (Pb-glass) mode,

3) scattering mode,

4) source mode,

5) cosmic ray mode.

In calibration mode, a NaI detector was placed directly in the beam line. The beam intensity was lowered so that the count rate in the detector was on the order of 1 kHz (so as to avoid over-stressing the NaI or the DAQ). This setup was typically done at the beginning of the run period. By running in this setup, the tagging efficiency was measured, the energy calibration of the detector (via the tagged photons) was determined and the position of the tagged photon coincidence peak was located.

In tagging efficiency mode, the Pb-glass detector was moved into the beam line. Once again, the beam intensity was lowered and data were collected. These data were analyzed for the purpose of monitoring the tagging efficiency on a daily basis. It is also a check of the beam stability throughout the run period.

In scattering mode, the Pb-glass detector was lowered out of the beam, the chosen target was placed at the target location and the NaI detectors were moved into their scattering positions. The beam intensity was increased to its maximum, typically 1 MHz per tagger channel, and data were collected. Once the scattering program began, the only stops were for facility maintenance and injections into the other rings. At this time, the deuterium target was serviced. The MAX-I ring was tuned after these shut downs so the daily tagging efficiency measurement was done at this time to measure any effect that the beam tuning may have had on the beam characteristics.

In addition to the calibration runs, a second, unique calibration of BUNI was done by using a Th-C source. This source was placed inside the aperture and the DAQ was triggered on the four NaI annular segments. The 2.614 MeV line is clearly seen in the data sets (Fig. 2.16) and is used for both calibrating the segments as well as monitoring their gain drifts.

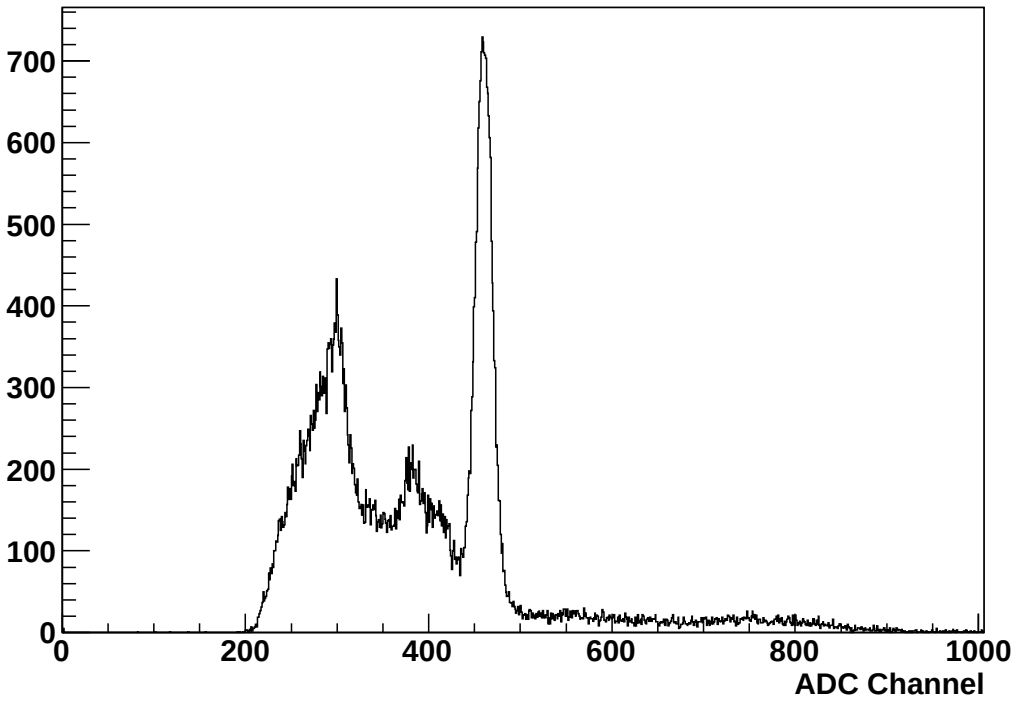

Figure 2.16: Sample spectrum taken from a BUNI annular segment using the Th-C source. The 2.614 MeV line dominates the spectrum and is used for both calibration and gain monitoring.

Finally, when time and conditions allowed, data were collected with the beam off. Typically, these runs happened before or after the run period or when the beam was lost for an extended period of time. These data were critical in order to subtract any cosmic rays or room background that might not be rejected by the vetoes surrounding the NaI. Additionally, cosmic ray data were collected for each NaI detector immediately after its calibration measurements. As discussed later, the cosmic rays provided a valuable means of tracking the gain drifts in the NaI detectors.

3 Data Analysis

3.1 Overview

This chapter details the process necessary for analyzing the d(γ,γ)d data sets. Subjects include energy calibration, data reduction, yield determination, detector efficiencies, and effects due to the finite geometry of the experimental setup.

The purpose of this analysis is to extract the experimental cross section which can be expressed as

$$\frac{d\sigma}{d\Omega} = \frac{1}{f_{geo}\kappa\Omega}\frac{f_{rate}Y_\gamma}{N_{\gamma,inc}}, \tag{3.1}$$

where:

κ	=	target thickness (target nuclei/cm^2),
Ω	=	solid angle subtended by the NaI detector,
Y_γ	=	scattered photon yield in the NaI detector,
$N_{\gamma,inc}$	=	incident photon flux on target,
f_{geo}	=	correction to the cross section due to finite geometry effects,
f_{rate}	=	correction to the cross section due to rate-dependent effects in the tagger.

The essence of the procedure is to count the numbers of incident and scattered photons and measure the target thickness and solid angles. As noted in the above equation, there are corrections that have to be considered. Furthermore, the low signal-to-noise ratio for deuteron scattering introduces other complications:

- extracting a photon yield requires good energy resolution. This necessitates properly reconstructing the event energy from the various detector components. In addition, gain drifts must be determined and corrected in order to maintain energy resolution.

- accidental coincidence events comprise a large portion of the data. Careful analysis is needed to properly subtract these events and extract an accurate yield.

- rate-dependent issues due to the high average electron rate ($\geq$ 1 MHz per tagger channel) in the focal plane hodoscope require careful analysis and simulation to make

proper corrections (f_{rate}). In addition, the instantaneous electron rates are as high as 5-10 MHz in the individual tagger channels.

- the finite geometry of the scattering setup and the non-standard target cell shape have an effect on the overall efficiency. Also considered here is the detector efficiency. These aspects had to be handled specifically via a Monte Carlo simulation (f_{geo}).

The rest of this chapter will detail these and all other aspects central to the data analysis. The analysis of the tagger calibration is discussed in section 3.2. Section 3.3 details the process of analyzing the data from the photon spectrometers. At the end of this section, the analysis of the scattering data is brought to its conclusion by determining the photon yield. The tagging efficiency and lead glass data are reviewed in section 3.4. Corrections to the data due to the high electron rate are explained and calculated in section 3.5. Section 3.6 covers the Monte Carlo simulations needed to determine the effective solid angle and account for the detector efficiency. The systematic uncertainties are detailed in section 3.7 and the data from the carbon and Kapton targets are presented in section 3.8. The scattering cross section is reported in the next chapter.

3.2 Focal Plane Hodoscope Analysis

The analysis of the electrons striking the hodoscope and recorded in the electronics is critical to extracting an accurate absolute cross section. The proper timing of the prompt electrons is needed in order to identify the tagged photons and the number of electrons are required to properly normalize the cross section. These factors are discussed in this section.

The hodoscope TDCs measure the relative timing between the electron in the tagger channel and the photon event in the NaI detector which is central to identifying tagged photons. This process is discussed in section 3.2.2. Due to the high electron rate, it is possible for a true electron to be preceded by an accidental and therefore the tagged event is lost. This effect and the subsequent correction is considered in section 3.5.1.

Equally important, the tagger channel scaler counts are essential for determining the photon flux. In order to properly normalize the cross section the number of incident photons on the target must be known. This is determined by measuring the number of tagged

photons per electron. (This procedure is referred to as the tagging efficiency measurement and is detailed in section 3.4.) The tagger channel scalers accurately count the number of electrons in each channel. A sample distribution is shown in Fig. 3.1 from November 2008. As with the TDCs, there are rate-dependent effects that need to be considered for the electron scalers as well and those are discussed in section 3.5.2.

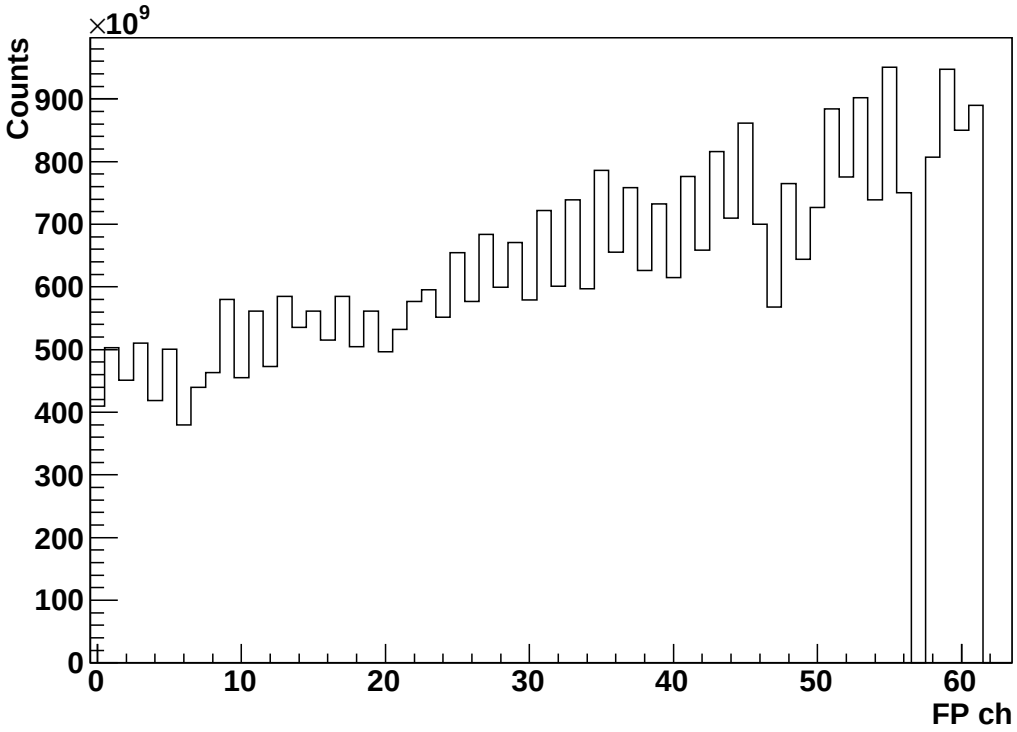

Figure 3.1: Sample tagger channel electron hits distribution. Channel 57 did not count due to a dead channel in the overlap coincidence module. The overall slope is due to the energy distribution of the recoil electrons after striking the radiator.

3.2.1 Tagged Photon Energies

The momentum of the recoil electrons in a given tagger channel is determined by the magnetic field in the tagger and the location of the tagger channel. This can be seen by considering the simple, classical case of an electron moving through a magnetic field that is perpendicular to its motion. The electron is deflected into circular motion by a force given by F = qvB and the centripetal acceleration is $a_{cent} = m\mathrm{v}^2/r$. Combining these gives the relation between

the size of the orbit and the momentum

$$r = \frac{m\mathrm{v}}{\mathrm{qB}} = \frac{p}{\mathrm{qB}}. \tag{3.2}$$

The subsequent photon energies are shown in Fig. 3.2 for both the 2007 ($E^0_{e^-} = 144$ MeV) and 2008 ($E^0_{e^-} = 165$ MeV) run periods. Each run period was divided into four bins and these are indicated. The tagged photon energies for each hodoscope channel are given in Appendix A.

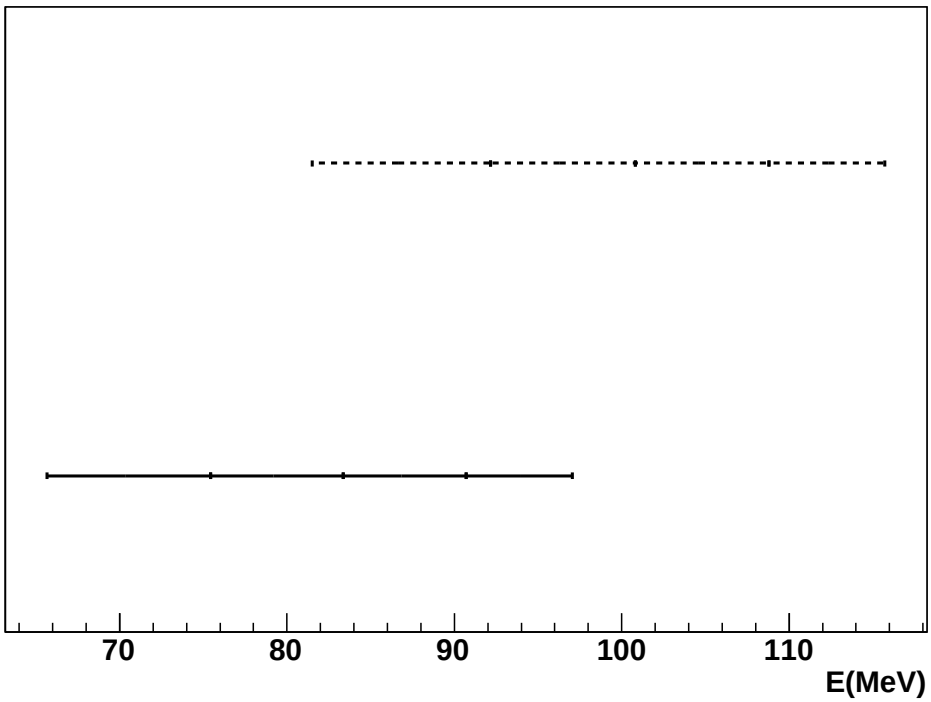

Figure 3.2: Tagged photon energies for the Nov 2007 (solid) and Nov 2008 (dashed). The divisions of the hodoscope into four bins are indicated also.

3.2.2 Hodoscope TDC Calibration

The single-hit TDCs employed for the SAL hodoscope in this experiment were not uniformly calibrated. In order to align the individual TDC spectra it was necessary to first determine the calibrations. This was accomplished by using a high frequency pulser with a logic output

which was fed into the TDC stops. The TDC start was synchronized to the pulser. The calibration constants for each tagger channel are shown in Fig. 3.3.

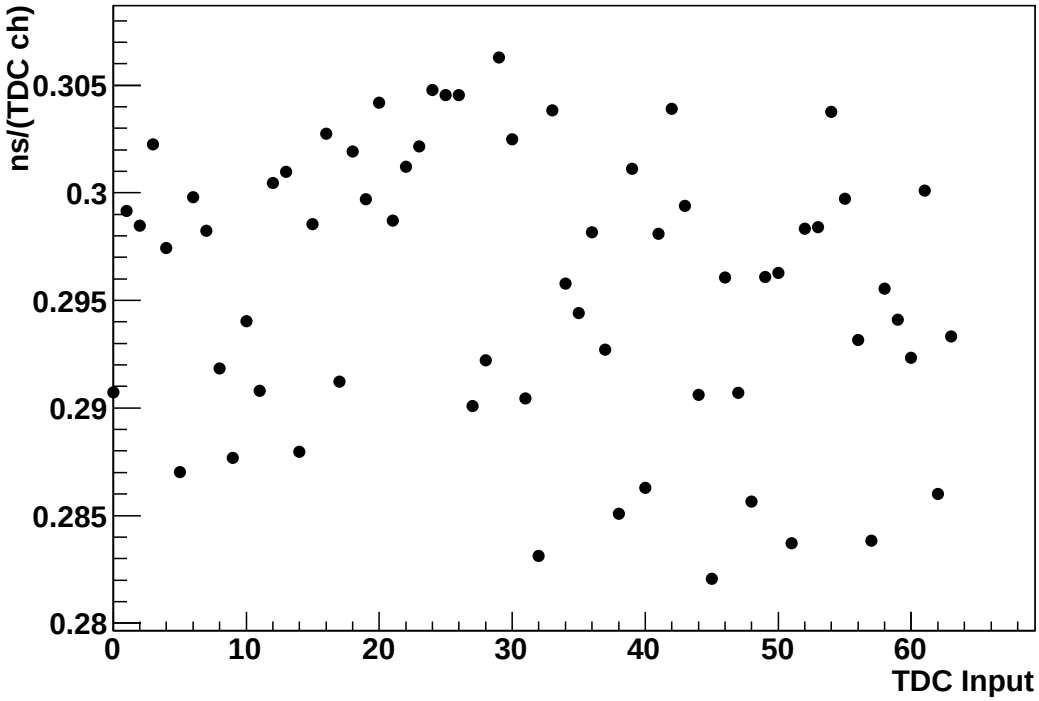

Figure 3.3: Calibration constants for each of the tagger channel TDCs.

A leading-edge discriminator (LED) is part of the electronics setup for both the hodoscope and the NaI detectors. An output from the LED is given only when the input pulse exceeds a given threshold. The overall amplitude of the pulse can affect the timing by moving the start of the output earlier in time for larger pulses (see Fig. 3.4). This effect is not significant in the tagger channels because the LED is firing on the minimum ionizing pulses which always have the same amplitude. However, the NaI detectors can have a wide variety of pulse heights depending on the energy deposition of the incident photon. This leads to a time walk in the tagger channel TDCs which is seen in the TDC output given by

$$T_0 = T_{TagCh} - T_{LED}, \tag{3.3}$$

where T_0 is the time difference between the stop (output signal from the tagger channel

LED) and the start (output from the NaI LED). As seen in Fig. 3.5, the timing of the pulse is correlated to the energy deposited in the photon spectrometer. In order to correct this effect, a second TDC was installed which used the same start (from the NaI LED) as the tagger channel TDC. However, the stop was now taken from the output of a constant-fraction discriminator (CFD) whose input is the same NaI pulse. The CFD fires when the input pulse reaches a certain fraction of the maximum so that there is no time walk. Due to its slow processing time, on the order of the rise time of the input pulse, the CFD was not a suitable choice for forming the trigger. The value of the second (self-timing) TDC is given by

$$T_1 = T_{CFD} - T_{LED}. \tag{3.4}$$

By combining the two previous equations, a time walk-corrected timing can be obtained

$$T = T_0 - T_1 = T_{TagCh} - T_{CFD}, \tag{3.5}$$

the result of this subtraction is seen in the bottom panel of Fig. 3.5.

Once the data have been corrected for the varying calibration constants and time walk, the timing peak can be resolved. Without the above steps the Time-of-Flight (ToF) peak is more spread and would make the subsequent analysis much more difficult. The ToF spectra is compared with and without the above analysis steps in Fig. 3.6. Typical cuts on the prompt peaks are 7-8 ns wide and contain $\sim$98% of all events.

The ToF spectrum, summed over all the tagger channels, is shown in Fig. 3.7 for the scattering data collected during the November 2008 run period. The same spectrum is shown in Fig. 3.8 where the region around the prompt peak has been enhanced. The three plots show the data with (a) no cuts, (b) a cut on the deposited energy corresponding to the entire tagged energy region, and (c) a missing energy cut on each individual tagger channel. The time structure of the beam and the location of the prompt peak necessitate that the timing resolution be optimized.

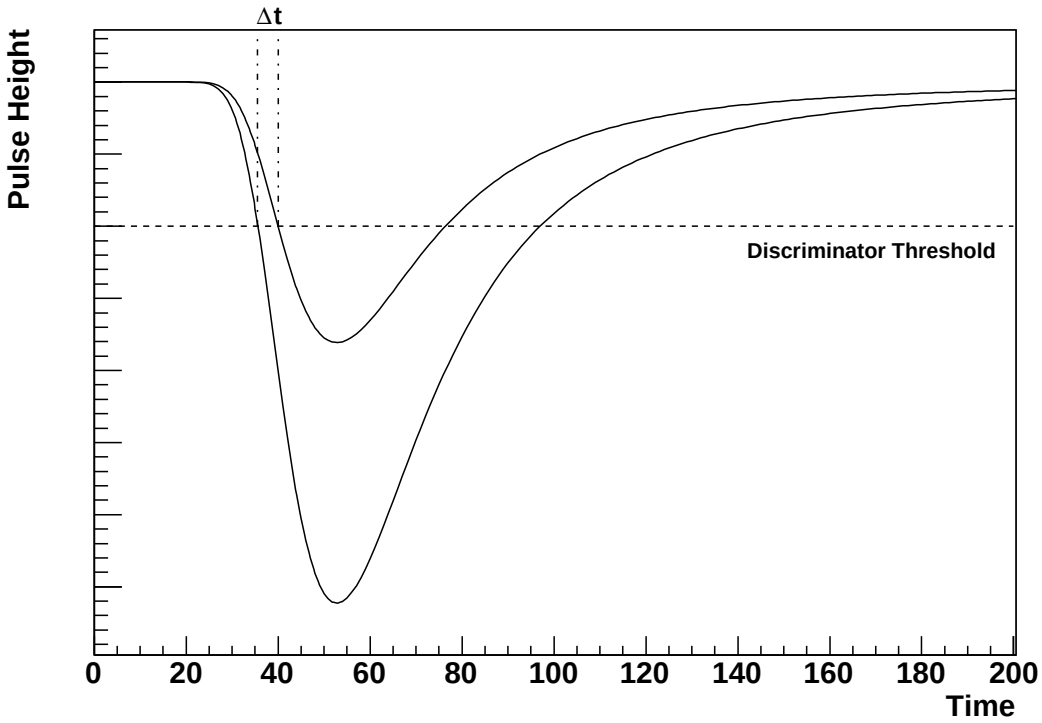

Figure 3.4: Example of the time walk effect in the leading-edge discriminators. The larger pulse crosses the threshold earlier than the smaller pulse. As a result, the larger pulse starts the DAQ earlier by the time Δt, as shown.

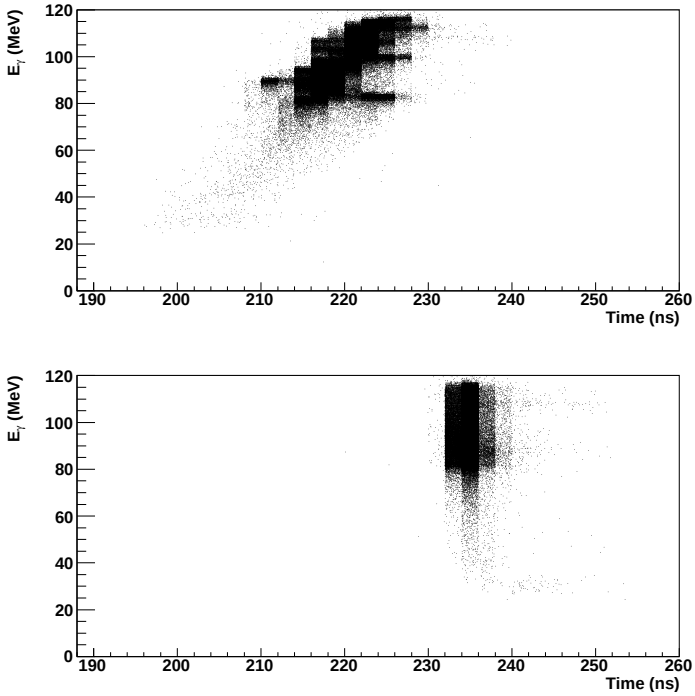

Figure 3.5: Plot showing the relationship between the photon energy in the NaI detector and the recorded time difference between the photon and electron discriminators. Without (top) and with (bottom) applying the correction for the time walk via the CFD.

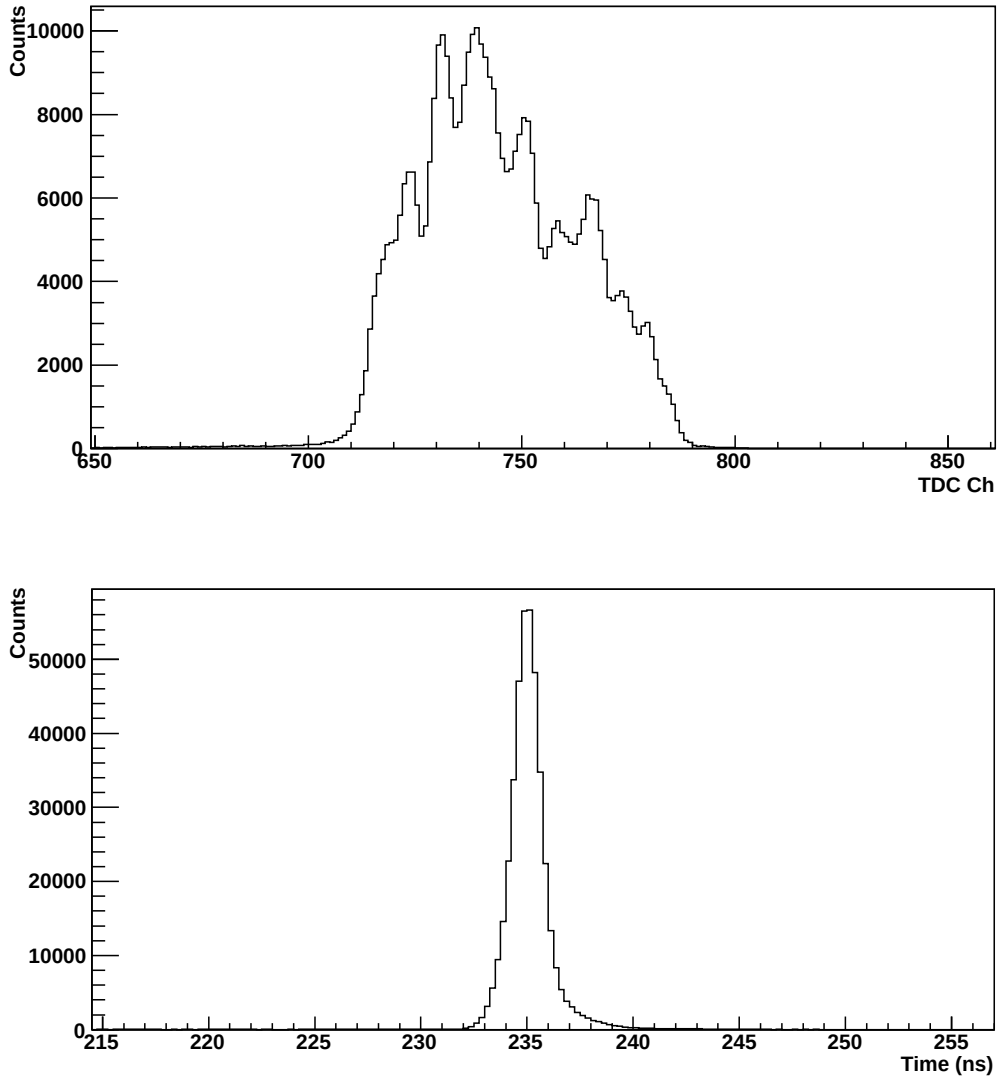

Figure 3.6: Time-of-Flight spectra for the electrons from calibration run. Top panel: sum of all tagger channels before any offline analysis. Bottom panel: sum of all tagger channels after correcting for time walk and calibration constants.

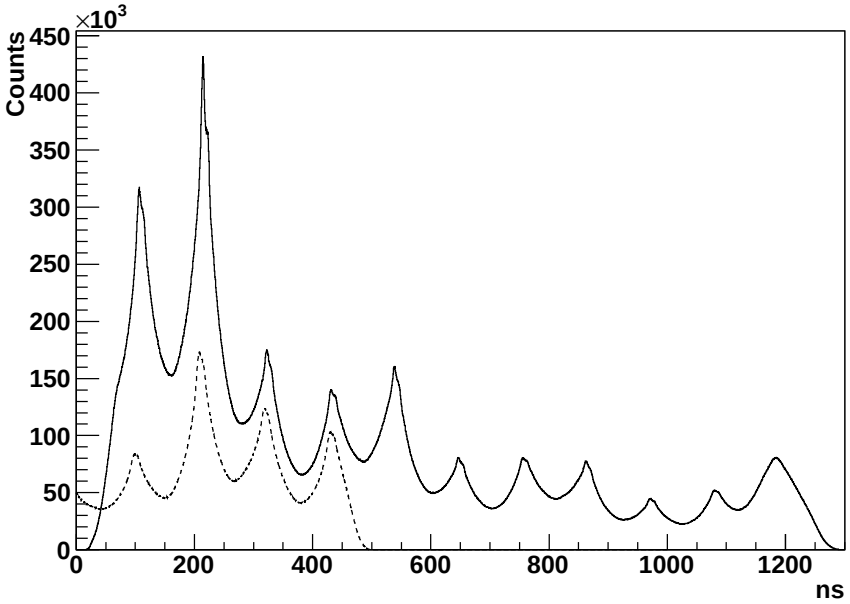

Figure 3.7: Time-of-Flight spectra from scattering runs (BUNI, 2008) for both the single-hit (solid) and multi-hit TDCs (dashed). The prompt peak that defines coincident electrons is centered at 220 ns.

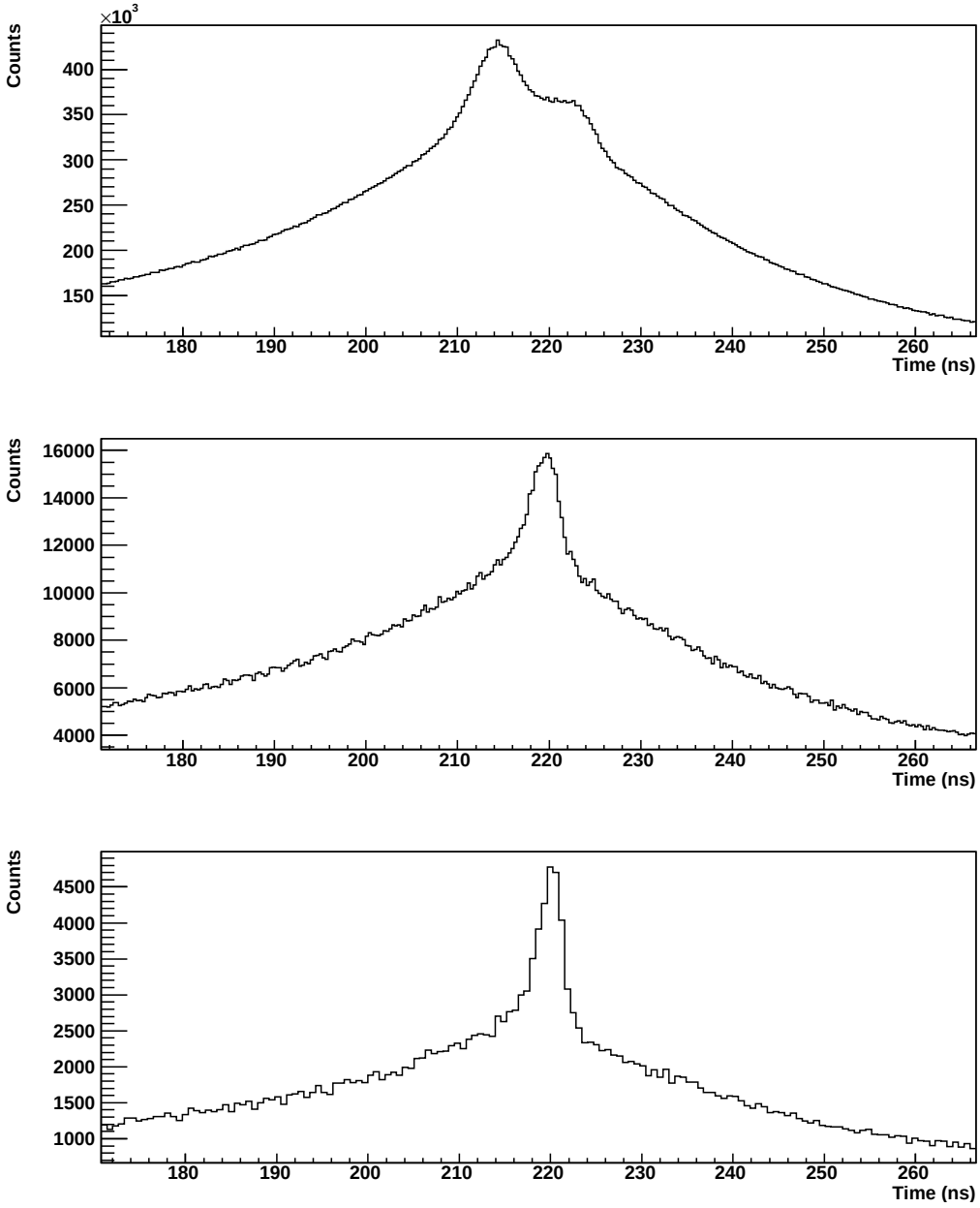

Figure 3.8: Time-of-Flight spectra from scattering runs (BUNI, 2008) with the prompt region enhanced. Top panel: no energy cut. Middle panel: $E_{63} \leq \mathrm{E} \leq E_0$. Bottom panel: E_i - 2MeV $\leq \mathrm{E} \leq E_i$ + 2MeV. The prompt peak is defined to be 216-224 ns.

3.3 NaI Detector Analysis

In order to extract yields from the photon spectrometers, it is necessary to:

1. gain match the PMTs on each detector.
2. determine the ADC output energy calibration.
3. make any corrections for the PMT gain drifts over the course of the run period.
4. generate appropriate prompt and accidental energy spectra.
5. accurately subtract the accidentals from the prompts in order to identify and integrate the elastic scattering peak.

3.3.1 Energy Calibration

This section details the steps in determining the energy calibration of the detector ADC. The calibration is done by using data taken in the calibration setup with a NaI detector in the beam line. Furthermore, in order to maintain good energy resolution when combining the data collected over the entire four-week run period, gain drifts in the PMTs must be monitored. The analysis for correcting the gain drifts is discussed at the end of this section. These corrections are made using selected cosmic ray events from the scattering data.

Software PMT Gain Matching The PMTs are gain matched in hardware, but this matching was not exacting enough and rarely tended to last beyond the initial setup. In addition then, the PMTs were further gain matched in software. The calibration data sets were used for this procedure. This process is broken into two parts. The first, which applies to all three NaI detectors, is to match the core PMTs using the tagged photons. Photons tagged by a given hodoscope channel have the same energy and therefore the same lineshape. Any differences in the ADC spectra are due to unmatched gains. The principle is to stretch or compress the pulse height spectra for each PMT so that for a given tagger channel the peak-to-pedestal separation is constant (see Fig. 3.9). By using all tagger channels an accurate gain matching factor is obtained for each core PMT.

The gain matching for DIANA is done at this point. For BUNI and CATS, though, a second step is necessary to accurately recreate the energy deposition in the detector. The annular segments must be gain matched so that they can be summed together with the core. This procedure was based on the premise that for some events the electromagnetic shower will be contained in one and only one segment. For events with a segment multiplicity of exactly one the segment ADC was plotted against the gain-matched, core pulse heights (see Fig. 3.9). The line that defines the leading edge of the plot is given by

$$E_{tag} = f_{seg} \times E_{core} + E_{seg}, \tag{3.6}$$

where E_{tag} is the constant tagged energy, E_{core} and E_{seg} are the energies (which are proportional to the pulse height) deposited in the core and segment respectively, and f_{seg} is the scaling factor used to gain match the segment. The effect of adding the annular segments in this way can be seen in the improved energy resolution in Fig. 3.10.

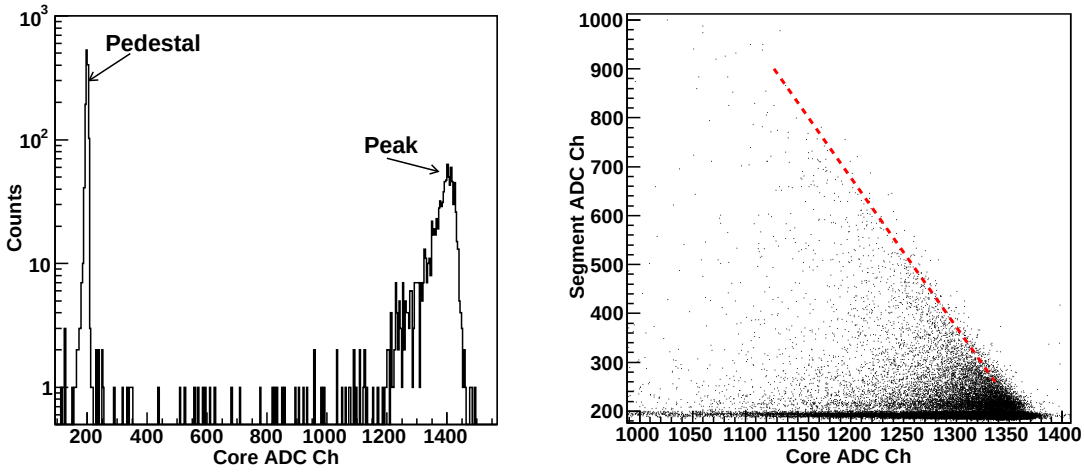

Figure 3.9: Left: Typical core spectrum from a FP trigger run showing both the pedestal and peak. Right: Plot of segment ADC vs (gain-matched) core ADC. The slope of the dashed line is the segment scaling factor. Both plots are taken from the calibration run with the NaI detector.

ADC Calibration Once all the PMTs have been gain matched, the pulse height spectrum in the detector can be fully reconstructed. The next step is to determine the absolute energy

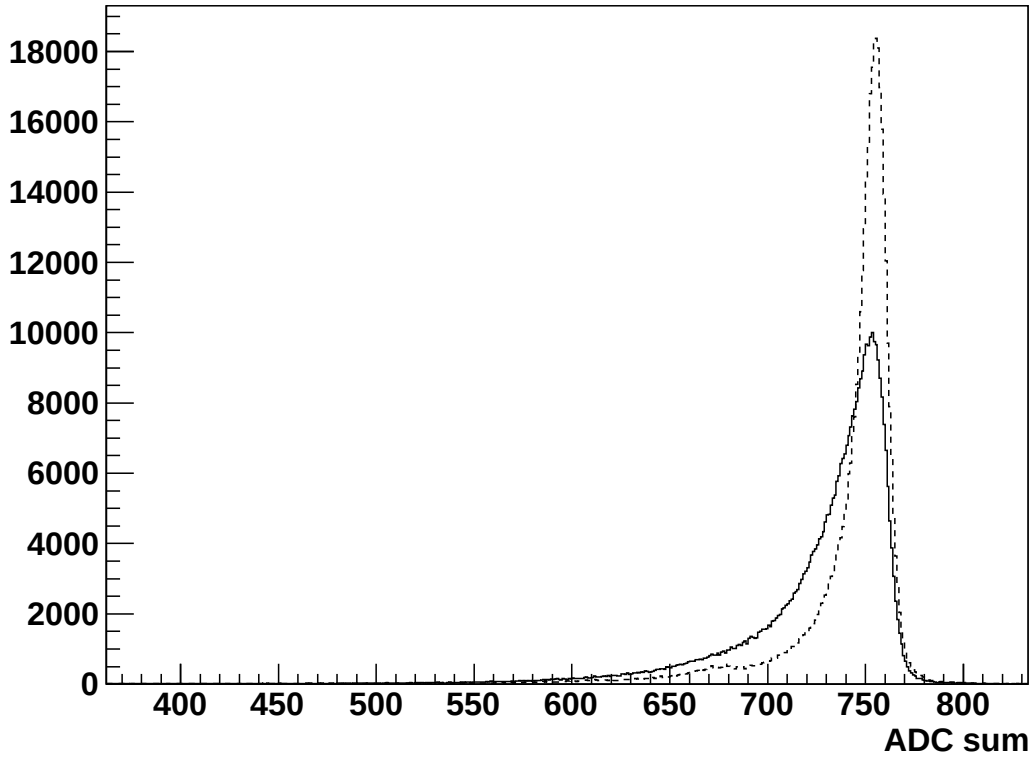

Figure 3.10: The photon lineshape taken from a BUNI in-beam run. The solid line is taken from the core only. The dashed line shows the improved resolution when the annular segments are added to the core.

calibration. For each tagger channel the peak of the summed ADC spectrum is found. These peak positions are then plotted against the known tagged photon energies and fit to a linear function to determine the energy calibration (see Fig. 3.11). The typical energy resolution for the NaI detectors is $\sim 2\%$ FWHM.

Gain Drift Corrections Tracking and correcting for gain drifts in the PMTs was essential in order to achieve the energy resolution stated above. The method of measuring this drift utilized the constant cosmic ray background. The energy deposition of the highest energy particles is directly correlated to the path length through the detector. Given sufficient statistics the pulse height spectrum of the cosmic ray background corresponds to a constant energy distribution. The variation of the pulse height lineshape from run to run depends

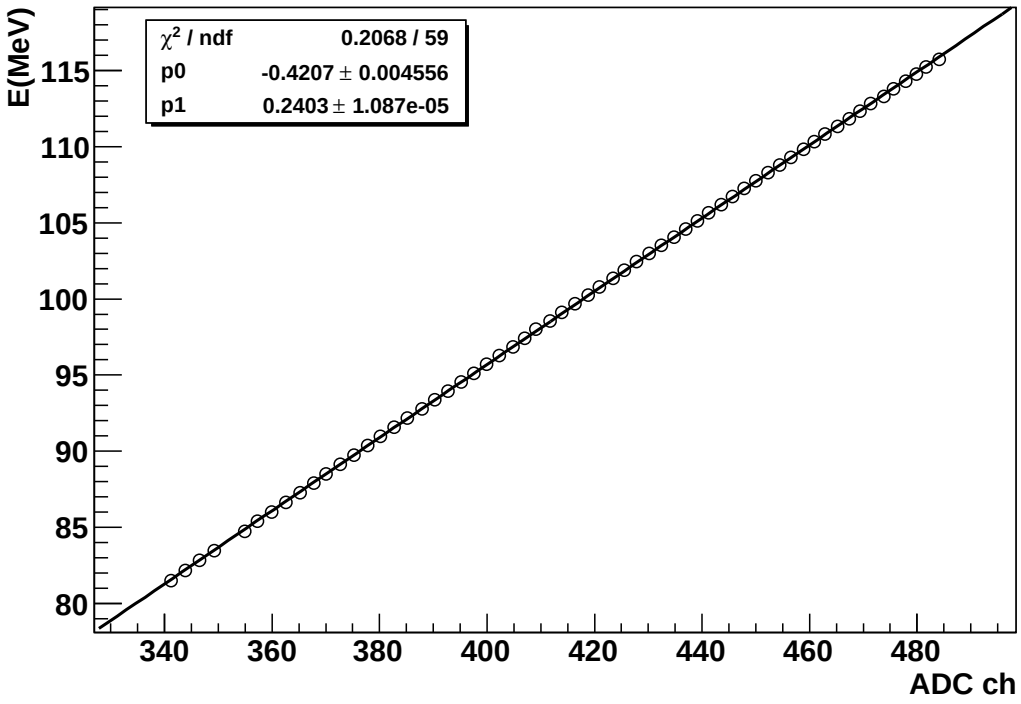

Figure 3.11: Plot of known tagger energy versus the peak position of the DIANA summed pulse height spectrum. The linear fit and its parameters are shown. The ADC is linear over the tagged energy region.

only on gain drifts in the PMTs. The gain drift for a few PMTs is shown in Fig. 3.12.

A more detailed explanation of the gain correction and the effect that it has on the energy spectra is discussed in Appendix B.

3.3.2 Subtracting Accidentals

The previous two sections outlined the steps involved in identifying the prompt peak and calibrating the photon spectrometers. At this point, the prompt and accidental missing energy spectra can be generated. The prompt window is clearly defined and a cut can be applied to the prompt peak. There are a variety of options available for choosing an accidental window. The significant time structure in the beam led to many questions of whether the accidental lineshape is time-dependent. As shown in Fig. 3.13, the lineshapes from different accidental time windows are consistent which allows for the accidental window

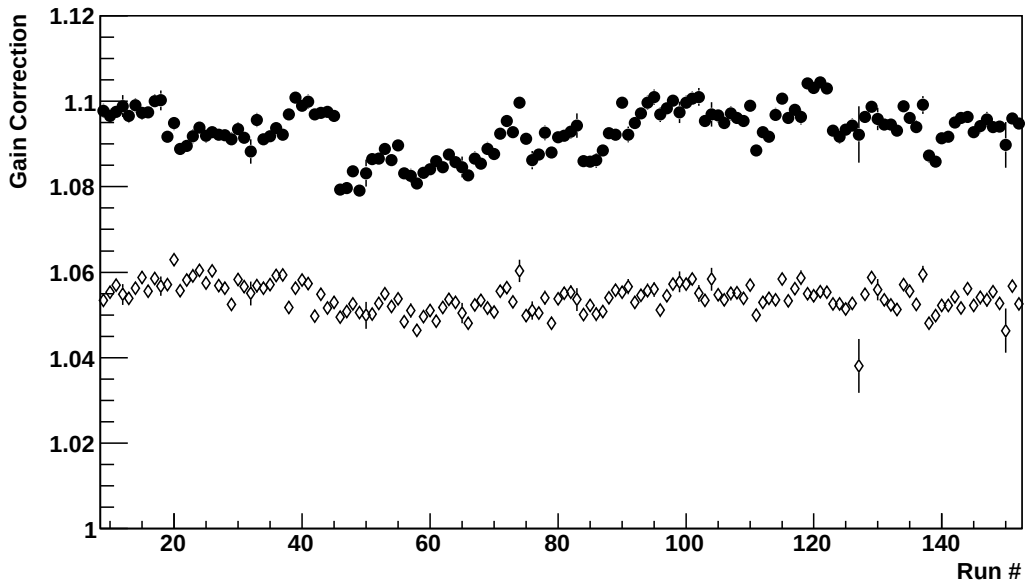

Figure 3.12: Plot of PMT gain drifts and statistical errors for BUNI core PMT 1(•) and 4(◇). These data were collected over three weeks of running for $\sim$ 150 runs.

to be chosen on the basis of maximizing statistics alone. A proper, accurate subtraction of the accidentals is critical to extracting the yields and getting proper fits to the lineshapes generated by the Monte Carlo simulations.

Cosmic Ray Background In order to properly subtract the accidentals, it is imperative that the normalization region (in both the prompt and accidental spectra) depend only on beam-related events. The accidentals are subtracted by normalizing them to the prompts in the energy region from 2 MeV above the elastic peak to the bremstrahlung endpoint energy. However, this region is not restricted to only beam-related events simply by applying the plastic veto cuts. The veto paddles are 95-99% effective at eliminating cosmic ray events. It was discovered that the accidental normalization was sensitive to the events that were missed by the vetoes. These residual cosmic rays occurred in different proportions in the prompt and accidental windows (due to different beam intensities and the widths of the respective windows) and so a preliminary cosmic ray subtraction was the first step in generating the proper "trues" missing energy spectrum. The cosmic ray spectrum was determined by applying the veto cuts to the pure cosmic ray runs that were collected throughout the run period. The

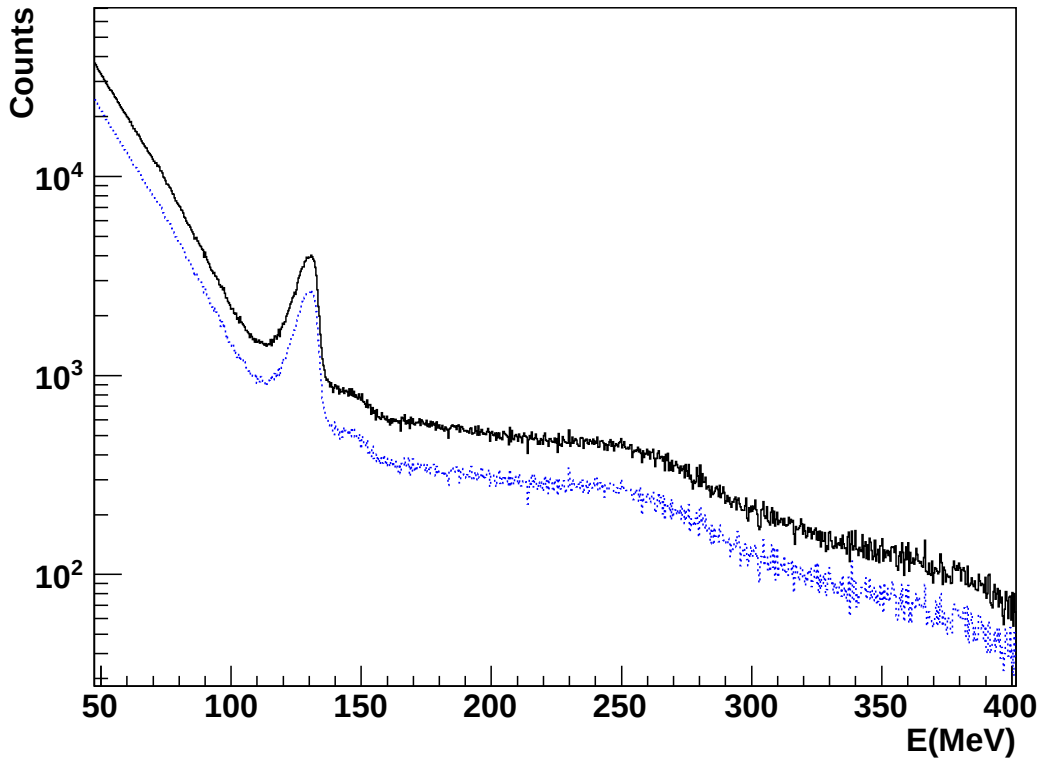

Figure 3.13: Plot of accidental energy spectra for two, separated, regions of the ToF spectrum. The missing energy spectra is independent of the timing window chosen.

resulting energy spectrum, for each hodoscope channel, was then normalized to the prompt and accidental spectra in the energy region above the bremstrahlung endpoint energy before being subtracted. Typical prompt, accidental and cosmic ray spectra are shown in Fig. 3.14. This step of subtracting the residual comics ensured that the normalization region for subtracting accidentals from prompts contains only beam-related events.

The scattering peak that appears in the prompt and accidental spectra at E-E_T $\simeq$ 55 MeV is due to π^- photoproduction. These pions are then captured by the deuteron and the reaction emits two neutrons and a photon with an energy of $\sim$130 MeV. Since these events are untagged (the photon energies necessary for pion photoproduction are outside the tagger channel energies) they appear as accidentals. These events, aside from increasing the statistics in the accidental subtraction, are not relevant to this analysis.

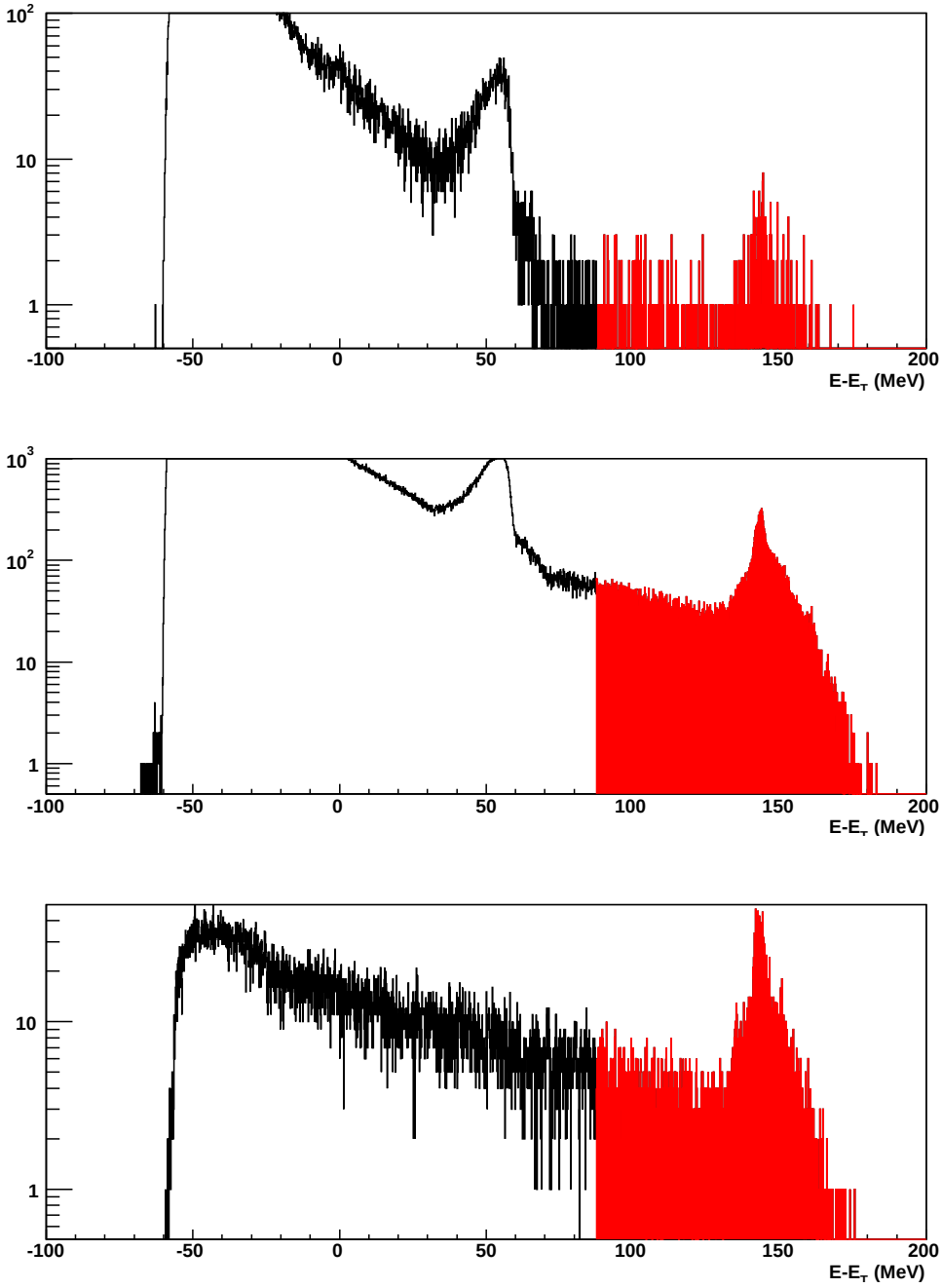

Figure 3.14: Prompt (top), accidental (middle), and cosmic ray (bottom) spectrum from the deuterium data set. The highlighted region corresponds to photon energies above the electron beam energy and is used to normalize the cosmic rays to both the prompt and accidentals.

The Trues Spectrum Once the cosmic ray spectrum has been subtracted, the correct accidental subtraction can be done to generate the final scattering lineshape. The cosmic ray-corrected accidentals are normalized, channel-by-channel, to the cosmic ray-corrected prompt spectra in the energy region from ∼2 MeV above the elastic peak to the electron beam energy. An example of the cosmic ray-corrected prompts and accidentals is shown in Fig. 3.15.

Several energy regions were taken for the normalization and the resulting effect on the extracted yield was smaller than the statistical fluctuations. The variation in these different normalization regions is taken as part of the systematic uncertainty in the yield. The trues spectra, summed over all the tagger channels, taken from the 150° detector (DIANA) in Nov 2008 is shown in Fig. 3.16.

3.3.3 d(γ,γ)d Yields

The SAL hodoscope was divided into four bins of ∼7.5 MeV widths. For each bin, the associated trues spectra were summed over the appropriate tagger channels and the yield was extracted. Due to the presence of an inelastic peak ∼2.2 MeV below the elastic peak the integration window extended from 1.8 MeV below the elastic peak to 1.8 MeV above it. Losses in the yield due to lineshape extending outside this window will be accounted for in the Monte Carlo simulations. The yields for each angle and energy bin are shown in Table 3.1[3].

[3]Tables are formatted so that the results from the 2007 data set are above (or to the left of) results from the 2008 data set

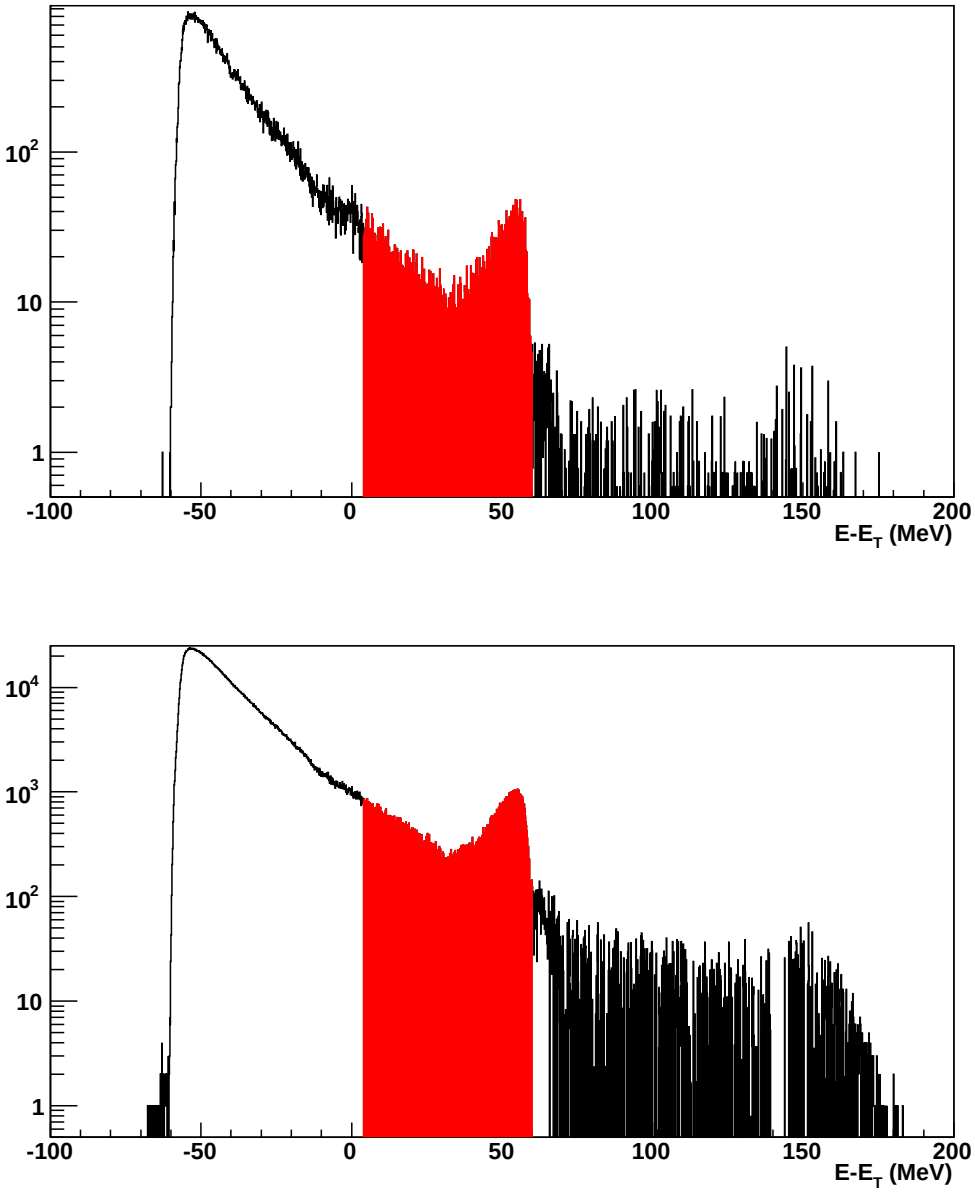

Figure 3.15: Prompt (top) and accidental (bottom) spectra after subtraction of cosmic rays. The region used to normalize the spectra is highlighted.

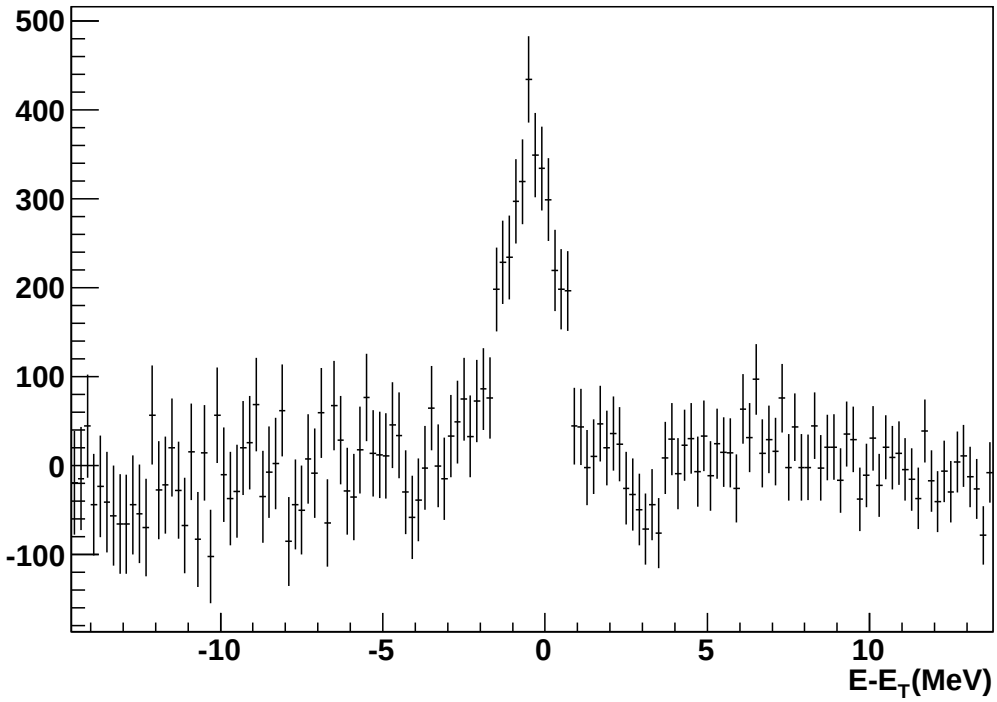

Figure 3.16: Trues spectrum in the 150° detector (DIANA) from 2008 resulting from the subtraction of the accidentals from the prompts. This spectrum is summed over all the tagger channels. The photon yield is obtained by integrating this spectrum from -1.8 MeV to +1.8 MeV.

	$\theta_{Lab} = 60°$			$\theta_{Lab} = 120°$			$\theta_{Lab} = 150°$		
E_γ(MeV)	Y	δY_{stat}	δY_{syst}	Y	δY_{stat}	δY_{syst}	Y	δY_{stat}	δY_{syst}
94	410	45	18	750	75	33	322	53	14
87	536	64	32	1028	93	36	413	65	24
79	606	90	41	1299	118	49	418	78	42
70	932	135	40	1076	167	90	651	103	60
112	891	79	26	1208	87	36	497	61	18
105	991	96	54	1285	102	56	663	71	38
96	1164	128	103	2192	123	23	999	87	44
87	1552	182	129	2067	151	94	891	109	49

Table 3.1: Photon yields in each spectrometer from integrating the missing energy spectrum from -1.8 MeV to +1.8 MeV.

3.4 Tagging Efficiency

In order to normalize the yields, the number of photons incident on the target cell had to be determined. To do so, the ratio of tagged photons to recoiling electrons in the tagger channel was measured by putting the detectors into the calibration position. This ratio, termed the tagging efficiency, is given by

$$\epsilon_{Tag,i} = \frac{\dot{N}_{\gamma,i}}{\dot{N}^{beam}_{e^-,i} - \dot{N}^{bg}_{e^-,i}} \tag{3.7}$$

where

$\dot{N}_{\gamma,i}$ = Rate of photons in hodoscope channel i,

$\dot{N}^{beam}_{e^-,i}$ = Rate of beam related electrons in hodoscope channel i,and

$\dot{N}^{bg}_{e^-,i}$ = Rate of background related electrons in hodoscope channel i.

During scattering runs $\dot{N}^{beam}_{e^-,i} \gg \dot{N}^{bg}_{e^-,i}$ so the background electron rate can be safely ignored. However, when the beam intensity is lowered to the rates needed for collecting tagging efficiency data the background rate is sufficiently large to require correcting. To do this, two sets of data are collected sequentially; the first is taken with the electron beam running and the second with the beam turned off. The beam on runs determine the photon and total electron rates. The beam off run is sensitive only to the background related electron rate. Rather than use equation 3.7, the time integrated version was used where the beam and electron rates are normalized by the livetimes with the beam on and off, t^{on} and t^{off}, respectively.

$$\epsilon_{Tag,i} = \frac{N_{\gamma,i}}{N^{on}_{e^-,i} - \frac{t^{on}}{t^{off}} N^{off}_{e^-,i}}. \tag{3.8}$$

The tagging efficiency was measured daily using the Pb-glass spectrometer with the runs conducted using the FP trigger discussed in chapter 2. A typical photon lineshape is shown in Fig. 3.17(a), the corresponding electron hit pattern is shown in 3.17(b), and the subsequent beam off electron scalers are shown in Fig. 3.17(c). The procedure for obtaining the tagging efficiency is to determine the number of tagged photons by integrating the photon spectrum above the pedestal. The background-corrected electrons are normalized and the tagging efficiency is determined for each tagger channel.

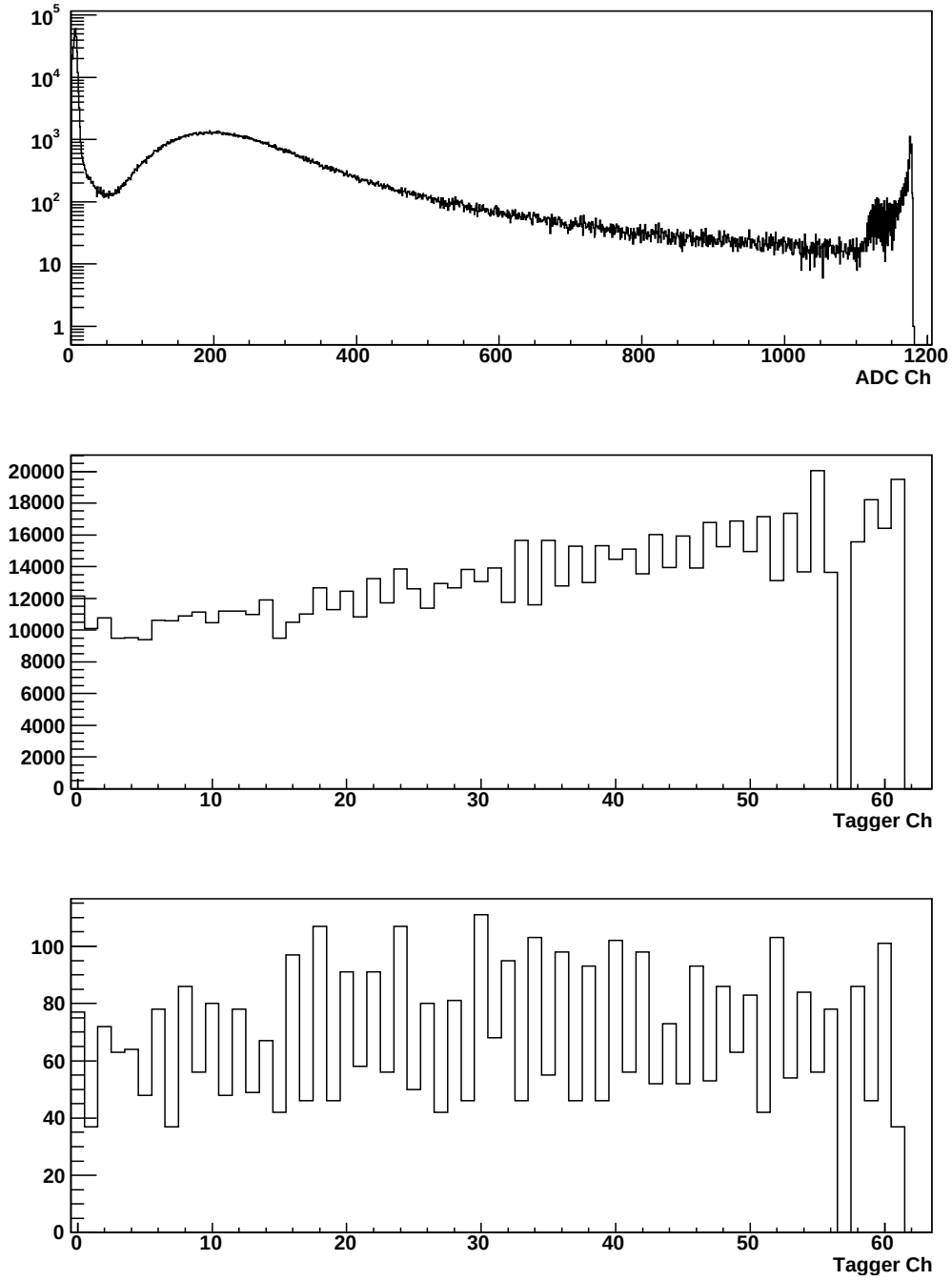

Figure 3.17: Sample spectra from the Pb-glass spectrometer while it was placed in the beamline. The beam-on ADC (a), beam-on tagger channel scalers (b), and beam-off tagger channel scalers (c) are all shown. These spectra are necessary for calculating the tagging efficiency.

E_γ(MeV)	ϵ_{Tag}	$\delta\epsilon_{Tag}^{stat}$	$\delta\epsilon_{Tag}^{syst}$	$\epsilon_{Tag}^{uncorrected}$
94	0.4296	5.74E-04	3.40E-03	0.4277
87	0.4308	5.21E-04	2.86E-03	0.4288
79	0.4299	4.68E-04	3.23E-03	0.4280
70	0.4263	4.42E-04	3.38E-03	0.4248
112	0.4651	5.57E-04	5.73E-03	0.4615
105	0.4683	5.29E-04	5.28E-03	0.4648
96	0.4674	4.85E-04	5.82E-03	0.4642
87	0.4644	4.39E-04	5.46E-03	0.4616

Table 3.2: Tagging efficiencies, with and without the background correction, for each energy bin.

Data from all tagging efficiency runs are combined and the result for each run period and tagger bin is shown in Table 3.2. Also shown are the tagging efficiencies that are obtained without subtracting the background. The background subtraction increases the tagging efficiency value by ∼1% or less.

Comparison of the calibration data from the NaI and the Pb-glass detectors indicate that the relative efficiency between the spectrometers in calibration setup is consistent with one. This result was confirmed by an independent Monte Carlo simulation.

3.5 Rate-dependent corrections

As mentioned at the beginning of this chapter the photon yields and electron counts are subject to two rate-dependent effects.

1. Stolen trues are tagged photons that are not recorded in the prompt TDC peak. This effect is due to the occurrence of an accidental electron in the time after the TDC start and prior to the true electron stop. Stolen trues affect only the photon yields.

2. Ghost electrons are an artifact of photon tagging systems using a focal plane hodoscope with overlapping channels. In short, chance coincidences between next-neighboring

channels can create a signal that is processed as a real electron in the middle channel. These electrons can show up in both the yield and normalization so it is necessary to correct both for ghosts.

3.5.1 Stolen Trues

As mentioned above, the stolen trues are the result of accidental electrons occurring in the time interval between the TDC start and the prompt electron. In general, the correction factor is $e^{-\mathrm{RT}_{\mathrm{prompt}}}$ where R is the electron rate in the hodoscope channel and T is the amount of time between the TDC start and the prompt electrons less the discriminator pulse width. (For details of the stolen trues correction see [Mac95].) However, the specifics of the electronics used in this experiment raised complicating issues so that the above assumption is no longer valid. These topics are discussed further in Appendix C. In the end, rather than relying on a general formula to determine the stolen trues correction a Monte Carlo simulation was written for the tagger electronics.

The tagger simulation was run for several electron beam rates and an interpolation of these results were made to the proper beam rates from each scattering run. The interpolation used was obtained by fitting the simulation results with:

$$f_{stolen} = e^{-\tau \mathrm{R}_{\mathrm{ave}}} \tag{3.9}$$

where f_{stolen} is the stolen trues correction, $\mathrm{R}_{\mathrm{ave}}$ is the average beam rate used an input to the simulation, and τ is a fitting constant. The tagger simulation is analyzed to determine its stolen trues correction from the TDC spectrum. These corrections and the appropriate average beam rates are combined to extract a value for τ. Once τ is known, the correction for the scattering data can be determined. To do so, the beam rate for each tagger channel and run is determined by analyzing the electron scalers. This rate was then inserted into the above equation to calculate the correction. These values were then summed appropriately over the channels and runs to obtain a final correction factor. The corrections for the stolen trues are shown in Table 3.3.

The same simulation was also analyzed in terms of the fraction of stolen trues, g_{stolen}, and the prompt window, $\mathrm{T}_{\mathrm{prompt}}$ using:

	$\theta_{Lab} = 60°$			$\theta_{Lab} = 120°$			$\theta_{Lab} = 150°$		
E_γ(MeV)	f_{stolen}	δf^{stat}_{stolen}	δf^{syst}_{stolen}	f_{stolen}	δf^{stat}_{stolen}	δf^{syst}_{stolen}	f_{stolen}	δf^{stat}_{stolen}	δf^{syst}_{stolen}
94	1.190	0.004	0.024	1.240	0.004	0.025	1.195	0.004	0.024
87	1.225	0.004	0.024	1.287	0.004	0.026	1.232	0.004	0.025
79	1.275	0.004	0.026	1.357	0.004	0.027	1.285	0.004	0.026
70	1.328	0.004	0.027	1.431	0.004	0.029	1.341	0.004	0.027
112	1.098	0.004	0.022	1.219	0.004	0.024	1.111	0.004	0.022
105	1.111	0.004	0.022	1.249	0.004	0.025	1.126	0.004	0.023
96	1.132	0.004	0.023	1.301	0.004	0.026	1.150	0.004	0.023
87	1.156	0.004	0.023	1.359	0.004	0.027	1.177	0.004	0.024

Table 3.3: The stolen trues corrections, as determined by the tagger simulation, for each spectrometer and energy bin.

$$g_{stolen} = e^{\mathrm{R_{eff}\,T_{prompt}}} \tag{3.10}$$

where $\mathrm{R_{eff}}$ is the effective beam rate accounting for the duty factor and any other potential effects and the prompt window is held constant. Table 3.4 shows the value of $\mathrm{T_{prompt}}$ obtained from the data and the effective beam rate obtained from the simulation in this approach. Also shown is the average beam rate used as an input to the simulation. The greater discrepancy between $\mathrm{R_{ave}}$ and $\mathrm{R_{eff}}$ in the 2007 run is assumed to be due to the beam having a worse duty factor at that time.

The ratio of effective to average beam rate in CATS and DIANA is much larger that of BUNI for the 2007 data because the smaller $\mathrm{T_{prompt}}$ prevents the detectors from seeing more of the total beam profile. In 2007, the periodicity of the beam was several hundred nanoseconds and so the detectors were sensitive to different portions of the beam. However, in 2008, the beam period was ∼100 ns and so each detector saw approximately a whole number of beam cycles prior to the prompt peak. This results in the $\mathrm{R_{eff}}$ to $\mathrm{R_{ave}}$ ratio being more consistent across the detectors.

Detector	Year	T_{prompt}(ns)	R_{ave}(kHz)	R_{eff}(kHz)
BUNI	2007	145	638	1043
			1284	2098
CATS	2007	46	638	2704
			1284	5167
DIANA	2007	62	638	2121
			1284	4095
BUNI	2008	148	663	912
			1133	1553
CATS	2008	45	663	1516
			1133	2496
DIANA	2008	54	663	1346
			1133	2321

Table 3.4: Comparison between simulated R_{ave} and R_{eff}. This comparison is sensitive to the duty factor of the beam in the window T_{prompt}.

3.5.2 Ghost Coincidences

Ghost coincidences arise when the two hodoscope counters that make up a channel are fired by separate electrons but within the coincidence resolving time of the channel, as shown in Fig 3.18. Here, the real electrons (e_1 and e_2) hit the tagger counters and show up in the respective channels (1 and 3 in this case). If the timing of the real electrons are such that they hit the counters that define the middle channel (here, channel 2 is defined by counters 2 and 3) within the coincidence resolving time then the electronics will process and record a hit in the middle channel as well. This accidental in channel 2 is referred to as a ghost.

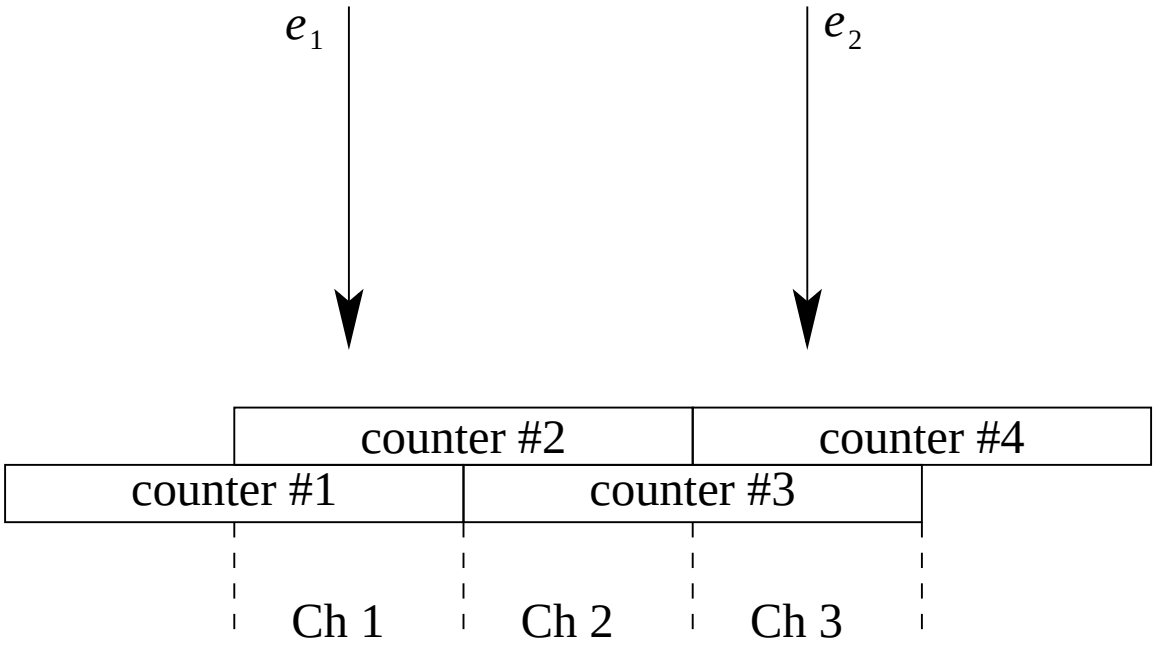

Figure 3.18: Diagram of the electrons in next-to-neighboring tagger channels that can lead to an accidental coincidence (ghost) in the middle channel.

The ghost electrons show up not only as extra counts in the electron scalers but can also appear as stops in the electron TDC. Unlike stolen trues, the correction due to ghosts must be made to both the cross section normalization and yields, which partially cancel. The very nature of the ghosts require special analysis and simulation. The same tagger simulation used to determine the stolen trues correction is also used to determine the ghost correction. Details of the simulation are in Appendix C. Ghost corrections are shown in Table 3.5.

	$\theta_{Lab} = 60°$			$\theta_{Lab} = 120°$			$\theta_{Lab} = 150°$		
E_γ(MeV)	f_{ghost}	δf^{stat}_{ghost}	δf^{syst}_{ghost}	f_{ghost}	δf^{stat}_{ghost}	δf^{syst}_{ghost}	f_{ghost}	δf^{stat}_{ghost}	δf^{syst}_{ghost}
94	1.031	0.010	0.015	1.028	0.010	0.013	1.018	0.010	0.009
87	1.018	0.010	0.010	1.017	0.010	0.008	1.009	0.010	0.007
79	1.036	0.010	0.020	1.035	0.010	0.018	1.022	0.010	0.013
70	1.027	0.010	0.015	1.020	0.010	0.013	1.010	0.010	0.010
112	1.013	0.005	0.005	1.012	0.005	0.005	1.013	0.005	0.006
105	1.009	0.005	0.005	1.009	0.005	0.005	1.008	0.005	0.005
96	1.015	0.005	0.007	1.015	0.005	0.007	1.014	0.005	0.006
87	1.010	0.005	0.006	1.010	0.005	0.006	1.010	0.005	0.006

Table 3.5: The ghost corrections for each spectrometer and energy bin based on the calculations of the tagger simulation. The correction depends on the beam rate, duty factor, and the pulse widths of the tagger channel discriminators.

3.6 $\kappa\Omega_{eff}$ Calculation

The measured (physical) solid angle and target thicknesses are not suitable for calculating the absolute cross section. These values need to be corrected for finite geometry effects, photon absorption within the target, end caps that alter the target length, and photon penetration through the lead shielding. In order to account for these factors a Geant4 simulation was used. This had the additional benefit of allowing the calibration and scattering lineshapes to be determined via a fit of the simulated spectrum to the data. This provides the necessary information to account for losses in the photon yield due to cosmic ray cuts and the yield integration window.

3.6.1 Geant4 Setup

Geant4 was used for simulating the effects of the setup and the resolution of the photon spectrometers. This simulation program is a general-purpose code written by the CERN group [Gea10]. As such, it contains all the essential physics for the purposes of simulating energy deposition in NaI spectrometers as well as the lead shielding, target and target hous-

ing. The program was written so that the geometry of the target and NaI detectors were accurately reproduced. The photon energies reflect those those of the tagged photons in the experimental setup. The overview of the simulation is shown in Fig. 3.19.

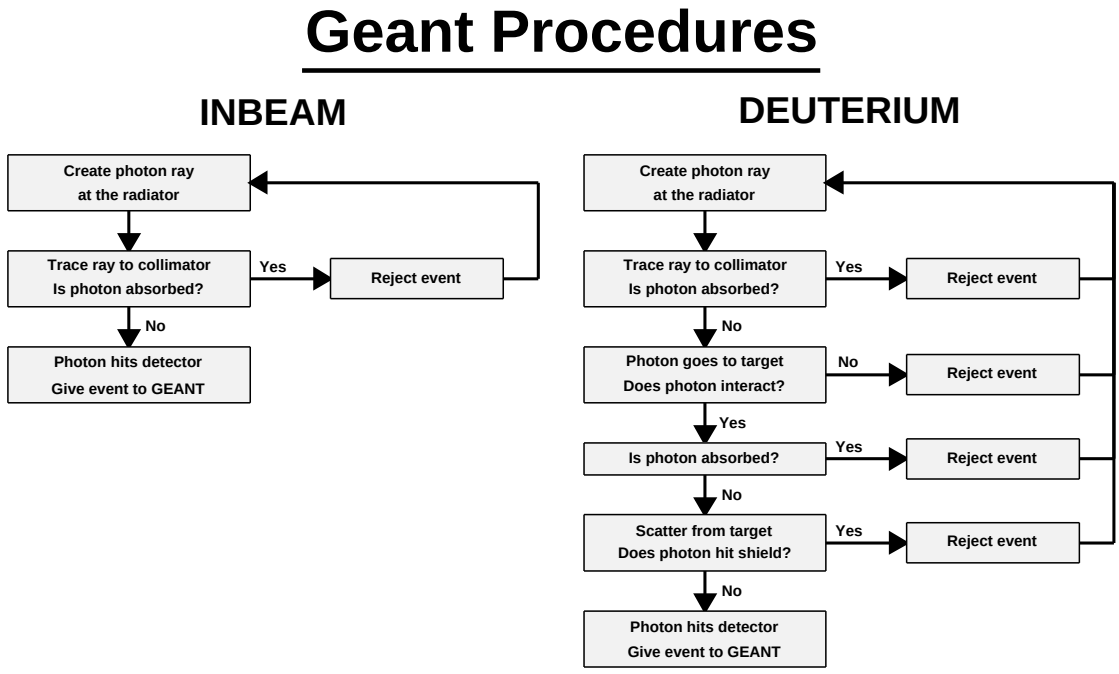

Figure 3.19: Steps in the Geant simulation where cuts are placed prior to the photon entering the detector and energy deposition. If the event is rejected at any step, the event is ignored and the simulation begins the next event. Only if a photon will be scattered into the spectrometer is the event fully processed by Geant.

The simulation does not account for fluctuations in the energy deposition (light collection) within the individual PMTs of the NaI detector. Instead, the output is an ideal representation of the lineshape without any intrinsic resolution effects. As a result it is necessary to smear the simulated lineshape to accurately reflect the data collected during the run period. Gaussian statistics were assumed to represent the light collection fluctuations and so the simulated lineshape was convoluted with a Gaussian (as given by Eq. 3.11). The detector response function, $R(x)$, is given in terms of the simulation output, $S(x)$, and three parameters: the amplitude of the lineshape, a; an arbitrary shift, i; and the smearing factor,

$\sigma(E)$, which is taken as a function of photon energy

$$R(x) = \Sigma_{x'} \frac{a}{\sigma(E)x'} S(x') e^{\frac{(x-x'-i)^2}{-2(\sigma(E)x')^2}}. \tag{3.11}$$

The case of the calibration run is considered first. The Geant4 simulation is run for multiple hodoscope channels so that $\sigma(E)$ can be accurately determined. The convoluted lineshape is free to vary in a, i, and $\sigma(E)$ until a best fit is obtained. See Fig. 3.20. Using the results from the various tagged photon energies surveyed a relationship is determined for $\sigma(E)$ as a function of incident photon energy.

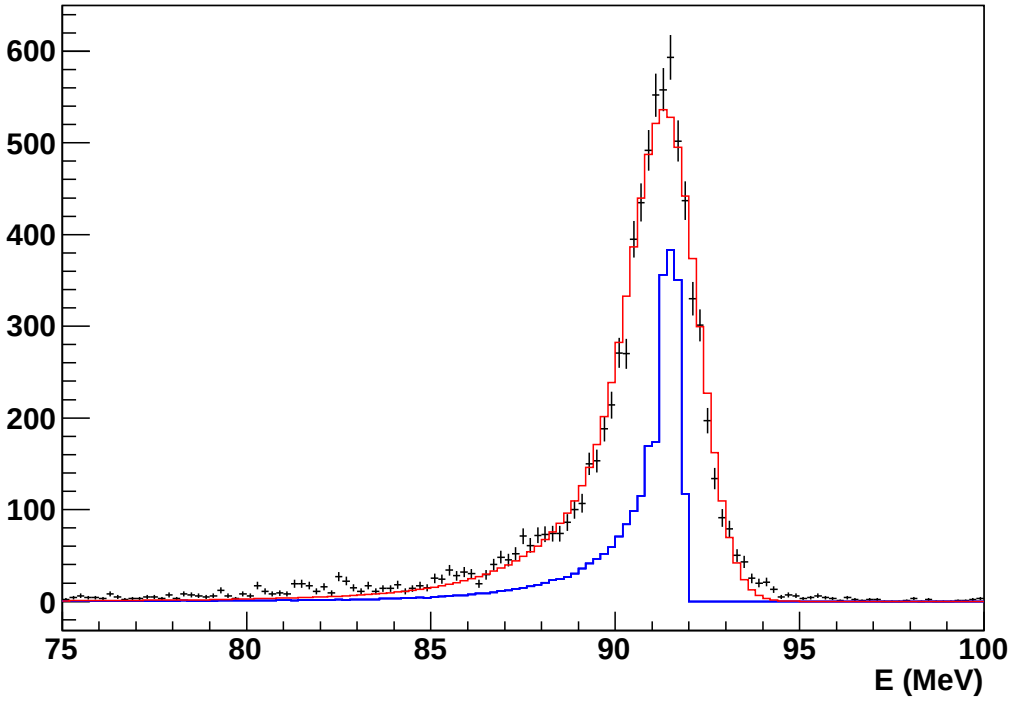

Figure 3.20: Sample spectrum from a calibration run showing a tagged photon energy spectrum with its errors (black), the simulated output (blue), and the convoluted response function fit to the data (red) with the proper smearing, amplitude, and relative shift.

Once the smearing values were obtained the simulation was run for the scattering geometry. The simulated scattering lineshape is convoluted and fit to the scattering data. The procedure is identical to the calibration case with the exception that $\sigma(E)$ is now constrained by the results of the calibration data. Fig. 3.21 shows the typical result of fitting

	$\theta_{Lab} = 60^\circ$			$\theta_{Lab} = 120^\circ$			$\theta_{Lab} = 150^\circ$		
E_γ(MeV)	Σ_W^{data}	Σ_W^{sim}	χ^2/ndf	Σ_W^{data}	Σ_W^{sim}	χ^2/ndf	Σ_W^{data}	Σ_W^{sim}	χ^2/ndf
94	381	410	1.95	741	750	1.61	353	322	0.98
87	497	536	1.00	952	1028	0.83	429	413	0.77
79	559	606	0.98	1199	1299	0.80	515	418	1.43
70	817	932	1.17	1002	1076	0.96	640	651	0.43
112	886	891	0.92	1187	1208	0.92	527	497	0.57
105	988	991	0.61	1350	1285	0.98	683	663	0.89
96	1149	1164	1.00	2071	2192	1.23	952	999	0.79
87	1520	1552	0.66	2078	2067	0.58	887	891	0.21

Table 3.6: Comparison of the yields obtained from integrating the missing energy lineshape and the simulated lineshape. Also shown is the value of chi^2/ndf for each measurement. The goodness-of-fit does not correlate to the ratio of measured and simulated yields.

the scattering lineshape.

A comparison of the yields from the data and the Geant simulation (over the summing window) are shown in Table 3.6 along with the reduced χ^2 for each detector and energy bin. There is no correlation between the yield comparison and the goodness of the fit.

Inelastic Contributions Unlike previous experiments which show a contribution to the elastic lineshape from the inelastic reaction, the plots in Fig. 3.21 do not show any indication of inelastic photons. An effort was made to fit the spectrum with an elastic and inelastic lineshape, but only null results were obtained for the inelastic contribution. The conclusion is that the inelastic contribution (which is already smeared out due to the kinetic motion of the quasi-free nucleons) is washed out by the large background in the spectrometers. Even so, the fitting and summing windows of the deuteron missing energy spectra are kept within the region of -1.8 MeV to +1.8 MeV to prevent inelastic contamination.

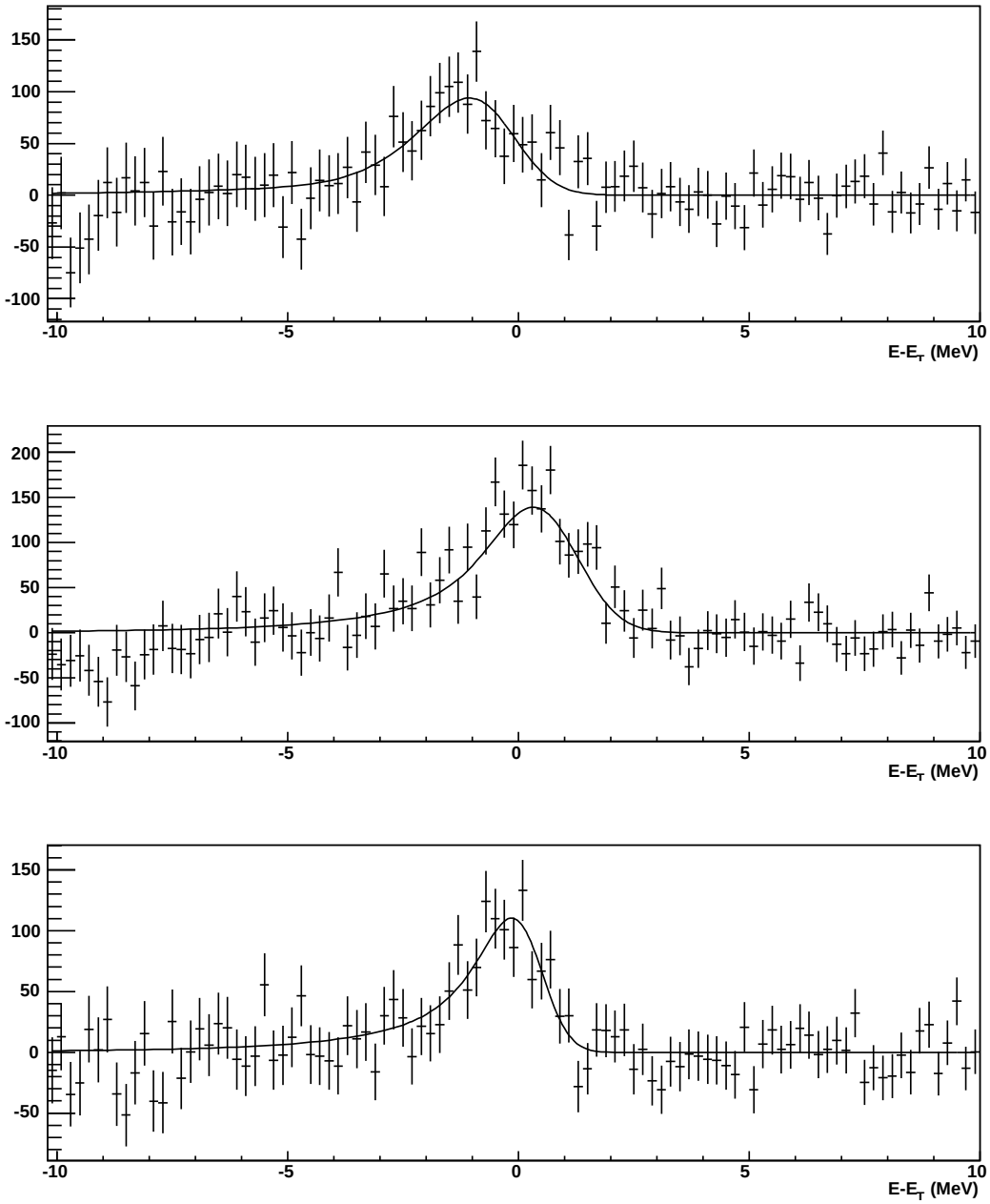

Figure 3.21: Sample spectra from a scattering run and the response function fit to the data (solid curve). The smearing of the simulated lineshape is constrained by the in-beam analysis, the only fit parameters were the amplitude and relative shift. These are taken from the 60^o (top), 120^o (middle), and 150^o (bottom) detectors. $E_\gamma = 96$ MeV; Nov 2008.

3.6.2 Extracting $\kappa\Omega_{eff}$

As mentioned at the beginning of this chapter the Geant4 simulations provide a means for determining the corrections due to finite geometry, absorption and cuts on the energy deposited in the different regions of the detector. The first two are determined by Geant4 based on the dimensions and physical characteristics of the materials involved; the last by carefully invoking the same cuts on the simulation as are used in reducing the data. These cuts are determined by the in-beam spectra and then applied to the scattering data. Table 3.7 shows the cuts and the net reduction[4] of events for the in-beam data for each detector. Once the simulation is performed, the resulting lineshape then contains all the information to calculate $t\Omega_{eff}$. This is determined via

$$t\Omega_{eff} = t_{sample}\Omega_{sample}\frac{N_{\gamma W}}{N_{\gamma Coll}} \tag{3.12}$$

where t_{sample} and Ω_{sample} are the values of the sampling target thickness and solid angle, respectively, used in the scattering simulation. $N_{\gamma Coll}$ is the number of photons that pass through the photon beam collimator prior to interacting with the target. $N_{\gamma W}$ is the yield of the simulated lineshape in the window W which is taken to be the same as that of the integration window used to extract the yield from the data. Table 3.8 compares the measured values of t and Ω to $t\Omega_{eff}$.

As an example, the losses in the DIANA 112 MeV bin, are: 3.7% from the effective target length, 1.6% from absorption of the incident photon, 34.7% from the cuts placed on the veto, etc., and 55% from the summing window. Target absorption of the outgoing photons is $\sim$1%.

The validity of the simulation was confirmed by analyzing the output without the detector cuts and a widened summing window. Here, the value of $t\Omega_{eff}$ should be approximately the same as the measured value since there are no photon losses (except absorption which is small in the case of the deuterium target) and the finite geometry effects are modest. There are two cases to consider:

1. Maximum Ω: The entire photon lineshape is integrated which allows for the possibility of photons scattering from the inside wall of the aperture. The solid angle for

[4]Reduction in number of events in the in-beam data set due to these cuts

Detector	Year	Cut	ADC	E(MeV)	Net Reduction
BUNI	2007	Veto	35	0.1	0.048
		Segment 1	1600	7.7	
		Segment 2	1600	18.3	
		Segment 3	1600	9.7	
		Segment 4	1600	8.5	
		LED Threshold		18	
CATS	2007	Veto	140	0.1	0.020
		Plastics	250	2.2	
		Software Threshold		40	
DIANA	2007	Veto	100	0.1	0.036
		Annulus	120	1.4	
		LED Threshold		20	
BUNI	2008	Veto	35	0.1	0.053
		Segment 1	1600	8.4	
		Segment 2	1600	19.6	
		Segment 3	1600	11.2	
		Segment 4	1600	9.4	
		LED Threshold		18	
CATS	2008	Veto	80	0.1	0.034
		Plastics	250	1.1	
		Software Threshold		40	
DIANA	2008	Veto	100	2.9	0.037
		Annulus	120	1.6	
		LED Threshold		20	

Table 3.7: Table of cuts placed on the components of the NaI detectors for the purposes of rejecting cosmic rays, charged particles, and low energy events. Also shown is the loss of events from each cut on the in-beam data that were collected with each detector in calibration running.

	$\theta_{Lab} = 60°$		$\theta_{Lab} = 120°$		$\theta_{Lab} = 150°$	
E_γ(MeV)	$t\Omega_{eff}$ (mm msr)	$\frac{t\Omega_{eff}}{t\Omega_{meas}}$	$t\Omega_{eff}$ (mm msr)	$\frac{t\Omega_{eff}}{t\Omega_{meas}}$	$t\Omega_{eff}$ (mm msr)	$\frac{t\Omega_{eff}}{t\Omega_{meas}}$
94	3307	0.49	5987	0.55	3332	0.65
87	3936	0.59	6288	0.57	3383	0.66
79	4055	0.61	6639	0.61	3462	0.68
70	3825	0.57	6915	0.63	3561	0.70
112	4230	0.63	6547	0.60	2763	0.54
105	4263	0.64	6774	0.62	3063	0.60
96	4224	0.63	7047	0.64	3166	0.62
87	4680	0.70	7138	0.65	3028	0.59

Table 3.8: Comparison of the measured and effective values of $t\Omega$. The measured value of t is obtained by measuring the target length along its central axis. The measured value of Ω is obtained by calculating the solid angle of the of the defining aperture for the spectrometer.

consideration is that defined by the front face of the lead shielding.

2. Minimum Ω: The photon lineshape is integrated over the region which corresponds to the region of the in-beam spectrum (i.e., ignore very low energy events). These photons are assumed to have passed through the aperture without interacting. The solid angle for consideration is that defined by the back face of the lead shielding. This is the solid angle value that is usually reported in the measured values.

A comparison of these values, along with a comparison of t_{eff} to t_{meas}, are shown in Table 3.9. The rather large discrepancy for the CATS maximal solid angle is possibly due to the fact that its collimator was tapered rather than straight so that the photons encountered a thinner effective shielding wall. This exercise was only carried out for the 2008 data set because the simulation for the 2007 data set had a cut on the partially-filled target and so is not suitable for this exercise.

In order to calculate the cross section, the areal density of target nuclei, is needed. This is related to the target thickness by

Detector	Year	t_{meas}(mm)	t_{eff}(mm)	Extreme	Ω_{meas}(msr)	Ω_{eff}(msr)
CATS	2008	170	166	Min.	38.9	40.1
$\theta = 60°$				Max.	47.3	52.9
BUNI	2008	170	166	Min.	68.4	69.1
$\theta = 120°$				Max.	106.7	104.2
DIANA	2008	170	166	Min.	30.5	31.4
$\theta = 150°$				Max.	37.9	39.5

Table 3.9: Comparison of the measured and effective values of t and Ω for the extreme cases (see text for more details).

$$\kappa = \frac{\rho t N_A}{A} \tag{3.13}$$

where ρ is the density of the target, t is the thickness, N_A is Avogadro's number and A is the mass per target nuclei. The density of the deuterium target is determined from the target diagnostics.

Deuterium Density As mentioned in Section 2.4.1, there were several monitors attached to the deuterium target throughout the run period. The target temperature and pressure were recorded for each run and are used to determine the density of the target. Using the work of [Gle93], the target density can be determined by considering only the target pressure weighted for each run by the number of recoil electrons counted during the run. By doing so, the target pressure was determined to be $0.1629\frac{g}{cm^3}$ for November 2007 and $0.1626\frac{g}{cm^3}$ for November 2008. In both cases, the statistical and systematic errors have been determined to be less than 0.5%.

3.7 Error Analysis

The analysis of the uncertainties of the extracted cross section is critical to determining the quality of the data. Each photon energy-scattering angle data point has been assigned error bars. Statistical and systematic errors are discussed below as well as given in tables.

E_γ(MeV)	94	87	79	70	112	105	96	87
Net Yield	10.4%	9.39%	9.46%	16.5%	7.37%	8.01%	5.68%	7.30%
ϵ_{Tag}	0.1%	0.1%	0.1%	0.1%	0.1%	0.1%	0.1%	0.1%
$t\Omega_{eff}$	0.3%	0.3%	0.3%	0.3%	0.3%	0.3%	0.3%	0.3%
Target Density	0.5%	0.5%	0.5%	0.5%	0.5%	0.5%	0.5%	0.5%
Stolen Correction	0.1%	0.1%	0.1%	0.1%	0.1%	0.1%	0.1%	0.1%
Ghost Correction	1.0%	1.0%	1.0%	1.0%	0.5%	0.5%	0.5%	0.5%
TDC Cut	0.2%	0.2%	0.2%	0.2%	0.2%	0.2%	0.2%	0.2%
Total	10.4%	9.5%	9.5%	16.5%	7.4%	8.1%	5.7%	7.3%

Table 3.10: Statistical errors for the extracted cross section from BUNI ($\theta_{Lab} = 120°$).

3.7.1 Statistical Errors

The statistical errors arise from statistical fluctuations in the various steps in the analysis. While each step could in theory produce an uncertainty, it was found that most of these are negligible due to the high statistics (e.g., the electron yield and the Monte Carlo simulations). Indeed, almost all of the statistical uncertainty comes from the yield extraction of the elastic peak in the missing energy spectra. The limiting factor here is the relatively few true counts in the elastic peak coupled with a rather large background. The statistical errors are given in Tables 3.10 - 3.12.

3.7.2 Systematic Errors

The sources and magnitudes of the systematic errors are more difficult to quantify than the statistical. Efforts have been made to identify all sources and estimate the systematic uncertainty. This process, however, is far from precise. When in doubt, the decision was made to err cautiously and assign a larger error.

The systematic errors have three varieties: (1) those which affect the individual points separately (e.g., yield extraction), (2) those which affect all the cross section from one detector identically (e.g., detector positioning), and (3) those which affect all points from one run period identically (e.g., ϵ_{Tag}). The last two types of errors have significant meaning

E_γ(MeV)	94	87	79	70	112	105	96	87
Net Yield	11.9%	12.8%	16.3%	15.8%	9.03%	9.88%	11.6%	12.3%
ϵ_{Tag}	0.1%	0.1%	0.1%	0.1%	0.1%	0.1%	0.1%	0.1%
$t\Omega_{eff}$	0.4%	0.4%	0.4 %	0.4%	0.4%	0.4%	0.4%	0.4%
Target Density	0.5%	0.5%	0.5%	0.5%	0.5%	0.5%	0.5%	0.5%
Stolen Correction	0.1%	0.1%	0.1%	0.1%	0.1%	0.1%	0.1%	0.1%
Ghost Correction	1.0%	1.0%	1.0%	1.0%	0.5%	0.5%	0.5%	0.5%
TDC Cut	0.2%	0.2%	0.2%	0.2%	0.9%	0.9%	0.9%	0.9%
Total	12.0%	12.8%	16.4%	15.9%	9.1%	10.0%	11.7%	12.4%

Table 3.11: Statistical errors for the extracted cross section from CATS ($\theta_{Lab} = 60°$).

E_γ(MeV)	94	87	79	70	112	105	96	87
Net Yield	17.8%	16.1%	18.7%	15.9%	12.2%	10.8%	8.73%	12.2%
ϵ_{Tag}	0.1%	0.1%	0.1%	0.1%	0.1%	0.1%	0.1%	0.1%
$t\Omega_{eff}$	0.2%	0.2%	0.2%	0.2%	0.3%	0.3%	0.2%	0.3%
Target Density	0.5%	0.5%	0.5%	0.5%	0.5%	0.5%	0.5%	0.5%
Stolen Correction	0.1%	0.1%	0.1%	0.1%	0.1%	0.1%	0.1%	0.1%
Ghost Correction	1.0%	1.0%	1.0%	1.0%	0.5%	0.5%	0.5%	0.5%
TDC Cut	0.1%	0.1%	0.1%	0.1%	0.3%	0.3%	0.3%	0.3%
Total	17.9%	16.1%	18.7%	15.9%	12.2%	10.9%	8.7%	12.2%

Table 3.12: Statistical errors for the extracted cross section from DIANA ($\theta_{Lab} = 150°$).

to the extraction of the absolute cross section. For example, an uncertainty in the position of the detector would increase/decrease the solid angle and hence decrease/increase the cross section from that detector. Likewise, an over/under-measurement of the target density would decrease/increase the cross section from all the detectors. Hence, the systematic uncertainties are a measure of the degree to which the absolute cross section is known.

The systematic errors are summed in quadrature since there is no reason to expect the errors to be correlated. The systematic errors for each of the photon spectrometers are shown in Tables 3.13 - 3.15. The individual sources of error are discussed below.

Yields There were some systematic uncertainties in the extraction of the elastic peak yield from the photon spectrometer. The dominant effect here is due to the subtraction of the background contribution from the detector lineshape. In order to get an estimate of this error, the normalization region for the background subtraction was varied. Also, several efforts were made to remove any remaining over/under-subtraction of the background by fitting various functions to the missing energy spectra. After these steps were taken the error was estimated by taking the spread of the resulting yields.

Detector Positioning As in the discussion above, the position of the detector can have an effect on the solid angle. The error is dictated by the uncertainty in the detector placement. Given the difficulty in positioning the detectors a minimum value can not be assumed here. Instead, each detector was given an error of ± 3 mm and then the error in the solid angle calculated from this estimate.

Target Thickness The physical measurement of the target cell thickness has a small uncertainty. A value of t = (170 $\pm$ 2) mm has been used in this analysis.

Target Density The density of the target varies throughout the run period as seen in the pressure readings. This variation leads to an uncertainty in the number of target nuclei available at a given time. Given that there was some variation in the beam rates during the course of the run period there is concern that this could be a large uncertainty. Fortunately,

as seen in [Gle93], the deuterium density is very stable as a function of pressure in its liquid state.

Tagging Efficiency The systematic uncertainty due to the tagging efficiency is taken from the variation in the daily measurements. Geant simulations indicated that any systematic effects due to differences between the Pb-glass and NaI spectrometers is negligible and so these effects have been ignored. As mentioned previously, the work of [For10] seems to indicate that the tagging efficiency is stable as a function of beam energy. For those reasons, the systematic effects here are on the order of 1%.

$t\Omega_{eff}$ Extraction Typically one of the larger sources of error came from the Geant simulations and the calculation of $t\Omega_{eff}$. The largest unknown in the simulations was the spatial profile of the photon beam as it entered the photon collimator. It was assumed that the beam profile was a Gaussian distribution where the spread was chosen to match the tagging efficiency results. However, there was no apparatus available to confirm this assumption. In the end, two extreme profiles were considered to set some bounds on the systematic uncertainty. In the first case the beam was assumed to be a perfect cylinder with no divergence; while the second considered the beam to have a perfectly uniform divergence. Simulations were run and analyzed for these cases in the same manner as for the Gaussian distribution. The uncertainty shown below are the result of averaging the discrepancy of the extreme profiles from the Gaussian.

It is worth noting that the systematics are dramatically higher in this case for the 2007 run period than the 2008 run period. This is a result of the target not filling properly during the earlier run. The non-diverging beam does not notice this effect and so it tends to skew the uncertainties. Discounting this source, though, does not change the final systematic errors of these points significantly so they have been left as shown.

Summing Window As mentioned previously, the summing window (and, by default, the lineshape fitting window) was generally kept to a region from -2 MeV to +2 MeV to minimize any potential contamination from the inelastic contribution. However, the window can be narrower and this could result in a systematic variation of the cross section. The lower edge

of the summing window was increased over a small range. The change to the cross section was calculated for each change in the window and the spread of the cross section taken as the uncertainty due to the window.

Stolen Correction The error in the stolen trues correction is taken to be $\pm 2\%$. This value is obtained by comparing the stolen trues fraction in the pre-scaled FP trigger. This data set has a clean trigger signal with no accidentals so it is easy to analyze and simulate using the Monte Carlo program. The resulting stolen trues agree extremely well, but a maximum variation of 2% would still result in agreement between the simulation and data. Hence, this value was chosen to represent the worst-case scenario.

Ghost Correction The uncertainties in the ghost correction have to come from the simulation since there is no companion in the data as there is in the stolen trues case. There are two possible sources of error. The first is from re-binning the tagger channels. So the spread of ghost correction values for each tagger channel in a given energy bin is considered. Secondly, the time profile of the electron beam in the tagger channels can cause some variation in the ghost correction. This can be understood because the occurrence and timing of the ghosts is strictly due to accidental coincidences in the tagger channels which can very as the time profile is altered. Like the stolen trues correction, the worst-case uncertainties are used here.

TDC Cut The cut on the TDC prompt peak by definition cut off a small portion of the prompt electrons. The fraction of lost events due to this cut was determined by doing the same analysis with the in-beam data. However, since the prompt scattering peak sits atop a background with time structure there is the possibility that the prompt window is not centered on the peak. Therefore, in the in-beam analysis, the window was allowed to shift by ± 0.5 ns and the resulting change in the fraction of events cut was taken as the systematic uncertainty.

E_γ(MeV)	94	87	79	70	112	105	96	87
Net Yield	4.40%	3.70%	3.83%	8.83%	3.06%	4.36%	1.07%	4.54%
Detector Position	2.91%	2.91%	2.91%	2.91%	2.91%	2.91%	2.91%	2.91%
Target Thickness	1.18%	1.18%	1.18%	1.18%	1.18%	1.18%	1.18%	1.18%
ϵ_{Tag}	0.79%	0.66%	0.75%	0.79%	1.23%	1.13%	1.24%	1.18%
$t\Omega_{eff}$	9.78%	9.78%	9.78%	9.78%	2.46%	2.46%	2.46%	2.46%
Summing Window	2.83%	2.07%	2.34%	4.75%	0.95%	2.12%	1.19%	7.31%
Target Density	0.05%	0.05%	0.05%	0.05%	0.20%	0.20%	0.20%	0.20%
Stolen Correction	2.00%	2.00%	2.00%	2.00%	2.00%	2.00%	2.00%	2.00%
Ghost Correction	2.00%	2.00%	2.00%	2.00%	0.70%	0.70%	0.70%	0.70%
TDC Cut	0.71%	0.71%	0.71%	0.71%	0.33%	0.33%	0.33%	0.33%
Total	11.92%	11.51%	11.61%	14.67%	5.69%	6.73%	4.96%	9.80%

Table 3.13: Systematic errors for the extracted cross section from BUNI ($\theta_{Lab} = 120°$).

E_γ(MeV)	94	87	79	70	112	105	96	87
Net Yield	4.47%	6.30%	7.36%	4.82%	3.04%	5.52%	9.32%	8.69%
Detector Position	3.06%	3.06%	3.06%	3.06%	3.06%	3.06%	3.06%	3.06%
Target Thickness	1.18%	1.18%	1.18%	1.18%	1.18%	1.18%	1.18%	1.18%
ϵ_{Tag}	0.79%	0.66%	0.75%	0.79%	1.23%	1.13%	1.24%	1.18%
$t\Omega_{eff}$	8.30%	8.30%	8.30%	8.30%	1.98%	1.98%	1.98%	1.98%
Summing Window	7.26%	5.20%	14.67%	5.68%	2.75%	1.51%	3.09%	1.98%
Target Density	0.05%	0.05%	0.05%	0.05%	0.20%	0.20%	0.20%	0.20%
Stolen Correction	2.00%	2.00%	2.00%	2.00%	2.00%	2.00%	2.00%	2.00%
Ghost Correction	2.00%	2.00%	2.00%	2.00%	0.70%	0.70%	0.70%	0.70%
TDC Cut	2.33%	2.33%	2.33%	2.33%	0.70%	0.70%	0.70%	0.70%
Total	12.90%	12.66%	19.06%	12.21%	6.16%	7.33%	10.85%	10.03%

Table 3.14: Systematic errors for the extracted cross section from CATS ($\theta_{Lab} = 60°$).

E_γ(MeV)	94	87	79	70	112	105	96	87
Net Yield	4.62%	5.71%	9.83%	9.16%	3.67%	5.83%	4.39%	5.46%
Detector Position	2.09%	2.09%	2.09%	2.09%	2.09%	2.09%	2.09%	2.09%
Target Thickness	1.18%	1.18%	1.18%	1.18%	1.18%	1.18%	1.18%	1.18%
ϵ_{Tag}	0.79%	0.66%	0.75%	0.79%	1.23%	1.13%	1.24%	1.18%
$t\Omega_{eff}$	8.08%	8.08%	8.08%	8.08%	2.08%	2.08%	2.08%	2.08%
Summing Window	4.59%	6.27%	6.80%	5.42%	6.80%	4.29%	2.96%	4.08%
Target Density	0.05%	0.05%	0.05%	0.05%	0.20%	0.20%	0.20%	0.20%
Stolen Correction	2.00%	2.00%	2.00%	2.00%	2.00%	2.00%	2.00%	2.00%
Ghost Correction	2.00%	2.00%	2.00%	2.00%	0.70%	0.70%	0.70%	0.70%
TDC Cut	0.78%	0.78%	0.78%	0.78%	0.40%	0.40%	0.40%	0.40%
Total	11.08%	12.33%	14.94%	13.91%	8.72%	8.27%	6.66%	7.92%

Table 3.15: Systematic errors for the extracted cross section from DIANA ($\theta_{Lab} = 150°$).

3.8 Other Targets

As mentioned earlier, data were collected from targets other than deuterium. The two targets important from an analysis standpoint were carbon and Kapton. These data and their analysis are discussed in this section.

3.8.1 Carbon

A carbon target was employed for approximately one day of beam time during each of the two periods. These data served as a means of both confirming the detectors and electronics were properly working and also as a means of establishing the ability to extract an absolute cross section from the MAX-lab facility. The elastic Compton scattering cross section for carbon is more than an order of magnitude larger than that of deuterium, the signal-to-noise ratio is much larger, and the carbon inelastic peak is at 4.4 MeV, not 2.2 MeV. For these reasons, extracting the carbon cross section suffers from fewer problems than the deuterium data set.

$E_{\gamma,inc}$ (MeV)	$\theta_{Lab} = 60°$ ΔE (MeV)	$\theta_{Lab} = 120°$ ΔE (MeV)	$\theta_{Lab} = 150°$ ΔE (MeV)
94	1.9	5.4	6.6
87	1.6	4.6	5.7
79	1.4	3.9	4.8
70	1.1	3.1	3.8
112	2.7	7.6	9.2
105	2.4	6.6	8.1
96	2.0	5.7	6.9
87	1.6	4.6	5.6

Table 3.16: The difference of the Compton energy shift between carbon and deuterium at each of the scattering angles employed in this experiment. The large difference at the back angles is an indication that the Kapton target will have a minimal contribution to the extracted deuteron yields at these angles.

The analysis steps employed are exactly the same as those detailed above for the deuterium target. The cross section is found in the first section of the next chapter.

3.8.2 Kapton

The deuterium is housed in a cylindrical cell composed of Kapton. Even though the walls of the cell are $\sim$100 μm thick there is still some small probability that photons scattering from the cell walls could cause an event in the detector and be counted as an additional component of the deuterium yield. Kapton, for the purposes of Compton scattering, is composed primarily of carbon and the relative difference in the Compton shifted photon energies for each data point are shown in Table 3.16.

Based on these calculations it is expected that the Kapton contribution to the deuterium yield will be nearly zero for the back angle detectors and non-negligible for the forward angle detector. A dummy target composed of several hundred sheets of Kapton was made and placed at the target center position; approximately six hours of data were collected during each run period for the purpose of determining the photon yield from the cell.

The analysis of the Kapton data is similar to that done for deuterium. However, since only the effects related to the yield are needed, it was only necessary to obtain the scattering lineshape. The scaling factors relevant to correcting the data from the dummy target to the target cell also needed to be determined. These are the relative thicknesses of the two targets, their relative effective solid angles and the relative photon fluxes. Fig. 3.22 shows the Kapton lineshape (with the deuterium Compton shift applied before calculating E-E_T) and the integration window used in calculating the contribution to the deuterium yield.

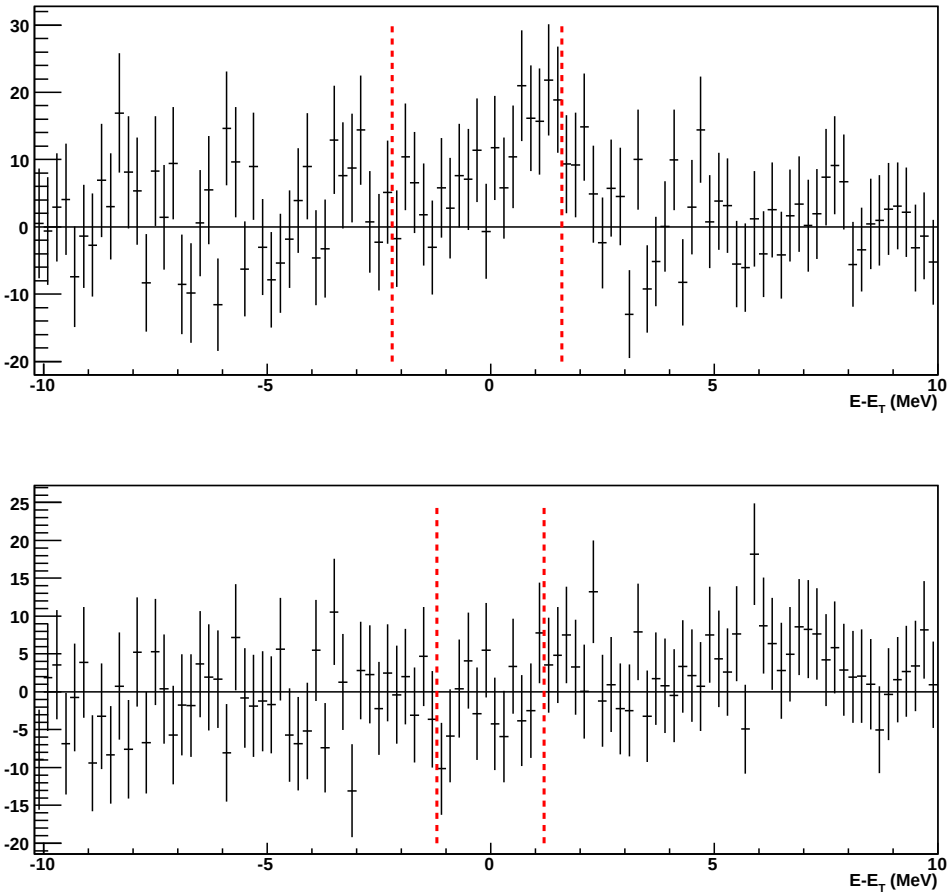

Figure 3.22: Kapton missing energy lineshapes with the accidentals subtracted for the 60^o detector (CATS – top) and 150^o detector (DIANA – bottom). The yield integration window is denoted by the dashed vertical lines. The contribution from the cell is small (but non-zero) at the forward angle and consistent with zero for the back angle detectors.

The yield of the Kapton data were multiplied by the net scaling factor to get the contribution to the deuterium yield. The net scaling factor was ∼0.79 for the 2007 run period and

	$\theta_{Lab} = 60°$			$\theta_{Lab} = 120°$			$\theta_{Lab} = 150°$		
E_γ(MeV)	Y	δY^{stat}	δY^{syst}	Y	δY^{stat}	δY^{syst}	Y	δY^{stat}	δY^{syst}
94	4	17	2	-10	23	4	2	20	5
87	22	16	4	15	22	9	-7	18	3
79	44	16	6	26	22	4	-13	19	3
70	71	16	11	53	24	6	-5	19	3
112	14	10	4	14	12	7	-5	8	4
105	15	11	5	6	12	2	3	9	4
96	60	12	5	17	13	4	-6	9	4
87	70	14	3	-8	15	7	-11	10	7

Table 3.17: Yields from integrating and scaling the missing energy spectrum from the Kapton target. The integration window is the same as that used for determining the deuteron yields.

$\sim$0.37 for 2008. (The difference in these values is due mainly to an approximate doubling in the number of Kapton sheets used in the dummy target.) The final contributions of the Kapton target to the deuterium yields are given in Table 3.17.

4 Discussion

4.1 Cross Sections

The absolute cross section is given in Table 4.1 for the deuteron and Table 4.2 for carbon. These results are still preliminary and should be regarded as such at this time. The values used to determine the carbon cross section are given in Appendix D. The cross section, as a function of energy for each angle, is shown in Figs. 4.1 and 4.2 for the deuteron and carbon, respectively.

	$\theta_{Lab} = 60^\circ$			$\theta_{Lab} = 120^\circ$			$\theta_{Lab} = 150^\circ$		
E_γ(MeV)	$\frac{d\sigma}{d\Omega}$ $(\frac{nb}{sr})$	$\delta\frac{d\sigma}{d\Omega}^{stat}$ $(\frac{nb}{sr})$	$\delta\frac{d\sigma}{d\Omega}^{syst}$ $(\frac{nb}{sr})$	$\frac{d\sigma}{d\Omega}$ $(\frac{nb}{sr})$	$\delta\frac{d\sigma}{d\Omega}^{stat}$ $(\frac{nb}{sr})$	$\delta\frac{d\sigma}{d\Omega}^{syst}$ $(\frac{nb}{sr})$	$\frac{d\sigma}{d\Omega}$ $(\frac{nb}{sr})$	$\delta\frac{d\sigma}{d\Omega}^{stat}$ $(\frac{nb}{sr})$	$\delta\frac{d\sigma}{d\Omega}^{syst}$ $(\frac{nb}{sr})$
94	10.16	1.22	1.31	10.74	1.12	1.27	7.89	1.41	0.86
86	9.19	1.18	1.15	11.70	1.10	1.33	8.71	1.40	1.06
79	8.63	1.41	1.65	12.48	1.19	1.44	7.69	1.44	1.14
70	11.86	1.88	1.44	8.20	1.35	1.20	9.70	1.54	1.34
112	7.96	0.72	0.50	7.76	0.57	0.45	7.10	0.87	0.62
105	7.88	0.78	0.58	7.30	0.59	0.50	7.55	0.82	0.63
96	7.87	0.92	0.86	10.68	0.61	0.55	9.76	0.85	0.66
87	7.89	0.97	0.80	8.51	0.62	0.84	7.61	0.92	0.61

Table 4.1: The extracted deuteron sross section from this experiment.

4.2 Comparison with Previous Data

The analysis, at this stage, suggests that there are unknown issues affecting the ability to extract the absolute cross section. However, the stated goal of the experiment included the extraction of the neutron polarizabilities. In order to gain some understanding of the electromagnetic polarizabilities, it is only necessary to know the relative angular distribution. This is true because the forward angle cross section is constrained by the Baldin Sum Rule and the sensitivity to α - β dominates at the backward scattering angles.

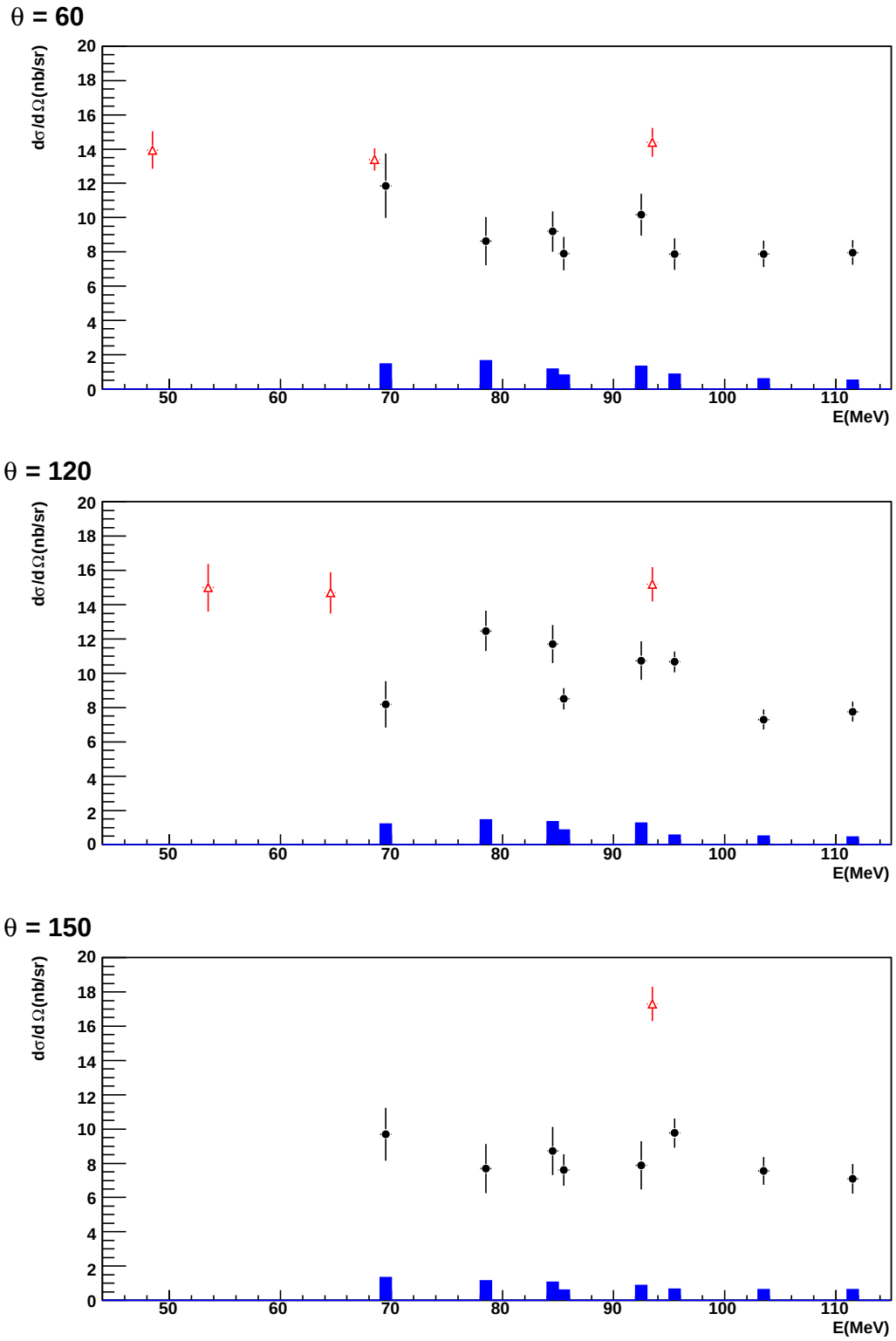

Figure 4.1: The deuteron cross section from these data (•) and previous experiments (Δ) are shown along with their statistical errors. Systematic errors for these data are shown as vertical bars along the energy axis.

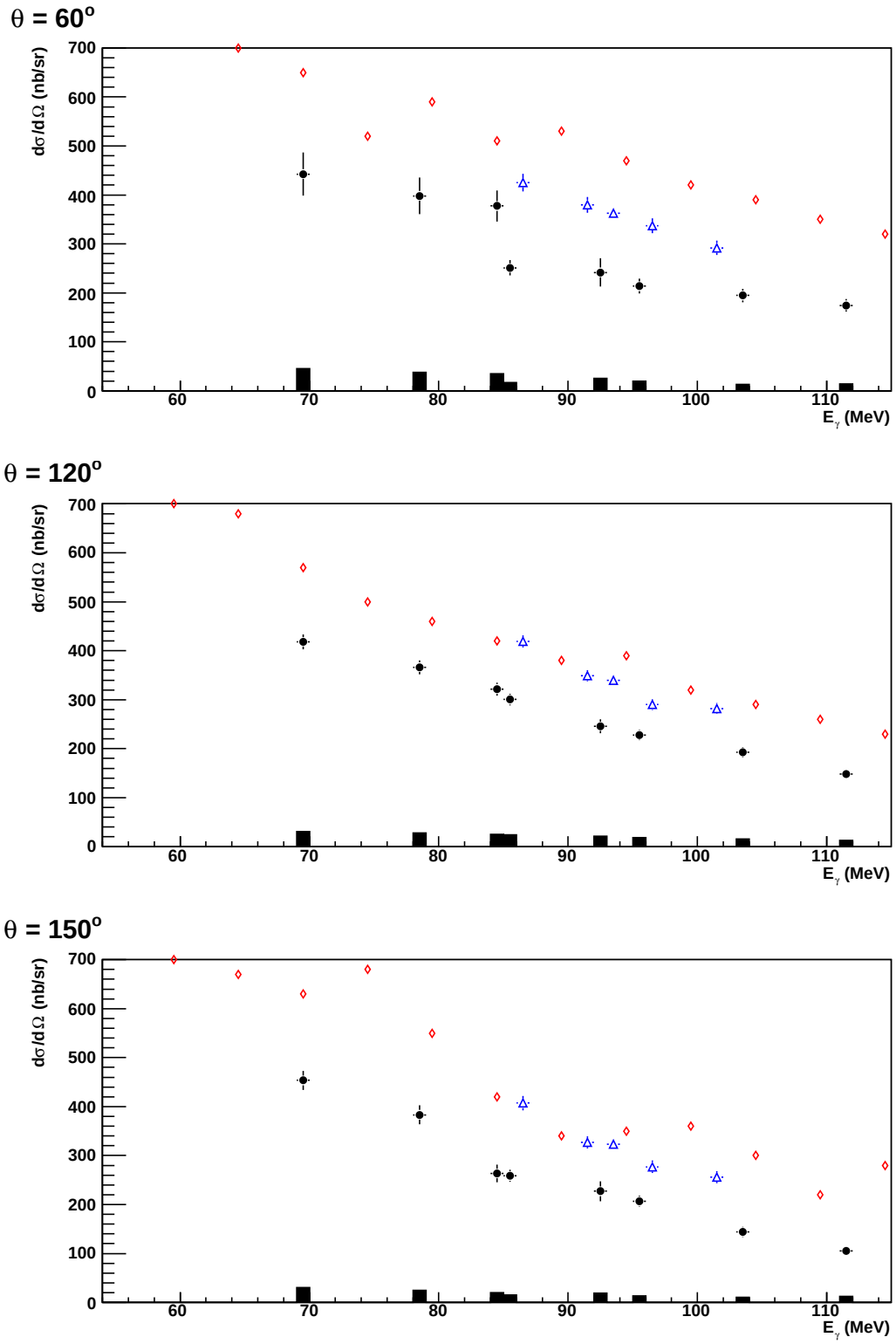

Figure 4.2: Carbon cross section from these data (•) and previous experiments (Δ[War01] and ◇[Sch90]) are shown along with their statistical errors. Systematic errors for these data are shown as vertical bars along the energy axis.

	$\theta_{Lab} = 60°$			$\theta_{Lab} = 120°$			$\theta_{Lab} = 150°$		
E_γ(MeV)	$\frac{d\sigma}{d\Omega}$ $(\frac{nb}{sr})$	$\delta\frac{d\sigma}{d\Omega}^{stat}$ $(\frac{nb}{sr})$	$\delta\frac{d\sigma}{d\Omega}^{syst}$ $(\frac{nb}{sr})$	$\frac{d\sigma}{d\Omega}$ $(\frac{nb}{sr})$	$\delta\frac{d\sigma}{d\Omega}^{stat}$ $(\frac{nb}{sr})$	$\delta\frac{d\sigma}{d\Omega}^{syst}$ $(\frac{nb}{sr})$	$\frac{d\sigma}{d\Omega}$ $(\frac{nb}{sr})$	$\delta\frac{d\sigma}{d\Omega}^{stat}$ $(\frac{nb}{sr})$	$\delta\frac{d\sigma}{d\Omega}^{syst}$ $(\frac{nb}{sr})$
94	242	29	26	246	14	22	227	20	19
86	378	32	35	322	13	25	263	18	20
79	398	38	38	366	14	28	383	19	24
70	442	44	45	418	15	31	453	20	31
112	174	13	14	148	9	13	105	9	12
105	194	14	13	193	10	15	144	10	10
96	214	15	20	228	11	19	206	11	13
87	251	16	17	300	11	24	258	12	15

Table 4.2: The extracted carbon cross section from this experiment.

The carbon data were used to test the ability to obtain relative cross sections. To do this, it was assumed that the extracted carbon cross section lacked an overall scaling factor common to all detectors and run periods. The re-scaled data were fit to the previously published cross section ([War01] results were used where applicable, [Sch90] at all other energies). By doing this, a scaling factor of 1.47±0.10 was obtained. The effect of the scaling factor on the cross section is shown in Fig. 4.3. This scaling factor was then applied to the deuteron data and the resulting cross section is shown in Fig. 4.4. The error bars on these points do not account for the uncertainty in the scaling factor.

These results present a more promising picture of the data. The scaling factor has brought the current analysis into agreement with the previously published data. A discussion of possible attempts to identify and understand the source of this scaling factor will be discussed later in this chapter.

4.2.1 Neutron Polarizabilities

The angular distribution of the re-scaled deuteron cross section is plotted in Fig. 4.5 for each energy bin. The curves are taken from [Gri10]. The error bars shown are statistical only

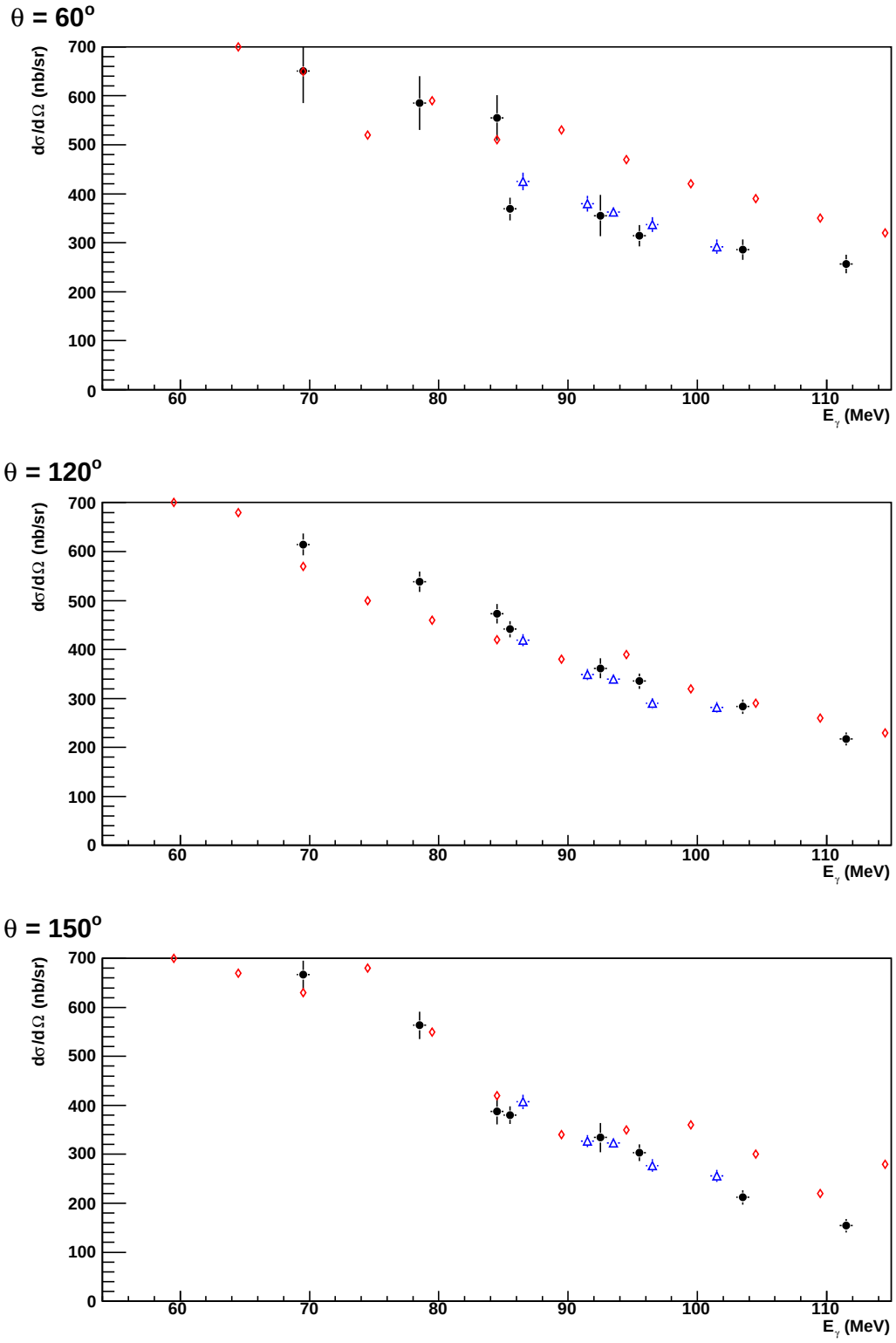

Figure 4.3: Rescaled (○) carbon cross section from these data and previous experiments (Δ[War01] and ♢[Sch90]).

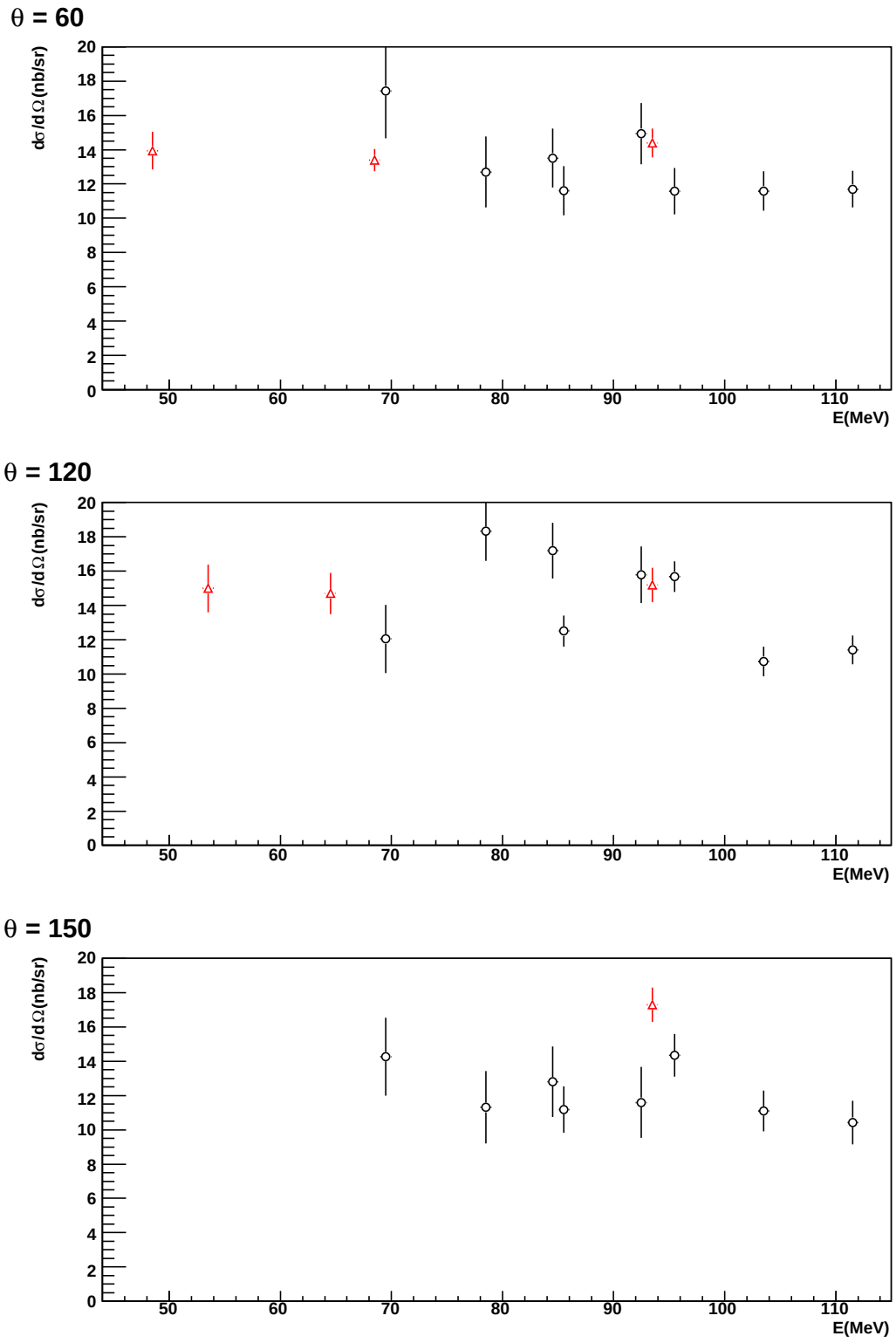

Figure 4.4: Rescaled deuteron cross section from these data (∘) and previous experiments (Δ).

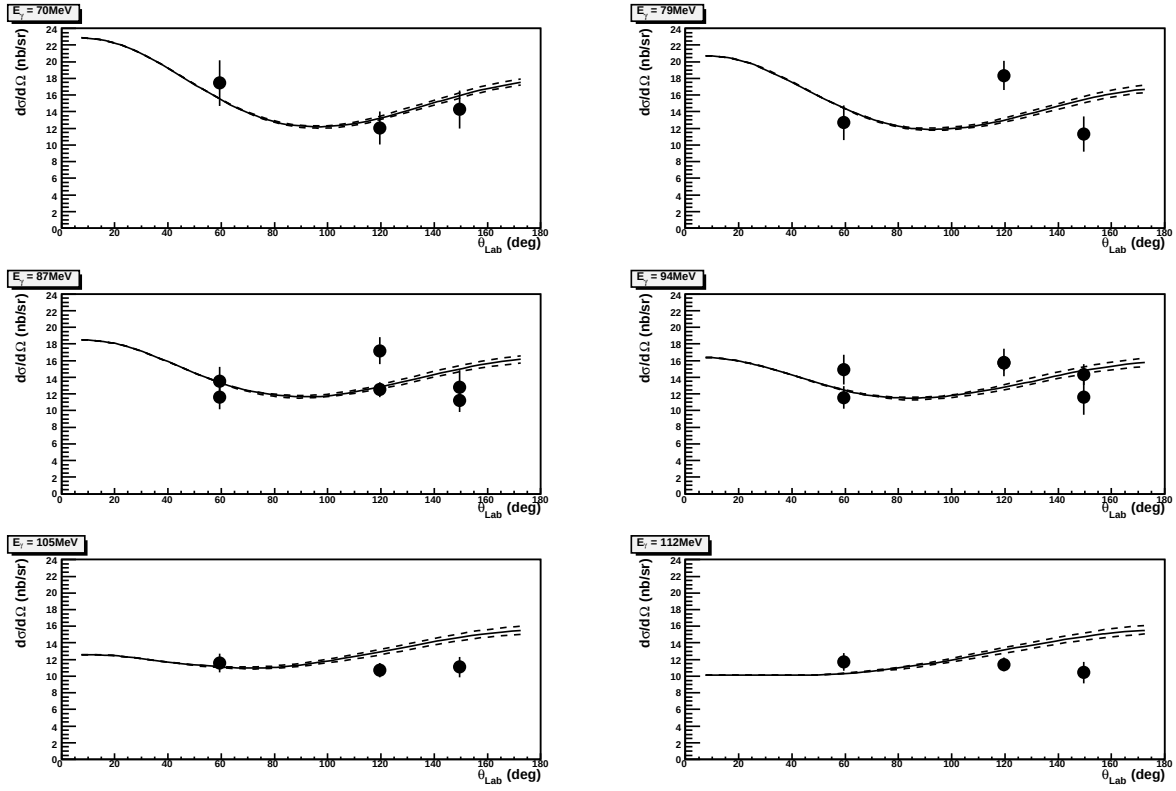

Figure 4.5: Plot of rescaled deuteron cross section versus scattering angle. Theoretical curves are taken from [Gri10] where the polarizabilities are those published prior to these data. The solid line represents the cross section obtained with isoscalar polarizabilities of $\alpha = 11.3$ and $\beta = 3.2$. Dashed lines correspond to cross section calculations with variations of $\delta(\alpha - \beta) = \pm 2$.

and do not reflect any contribution from the scaling factor. The error bars on these data are comparable to the previously published deuteron Compton scattering cross section and, as such, would represent an upgrade to the world data set based on the improved coverage of the phase-space. However, since the scaling factor is not fully understood at this time and represents a $\sim$50% increase to the deuteron cross section, it would be unwise to attempt to extract the neutron polarizabilities from these data.

4.3 Discussion of Results

The previous sections have presented the positive and negative realities of the deuteron Compton scattering program at this time. The scaling factor that persists, despite the

maturity of the data analysis, is disconcerting. As mentioned in chapter 2, the MAX-lab facility had undergone a major upgrade just prior to this experiment. As the first measurement performed post-upgrade, it was conceivable that issues arising from the changes to the accelerator and experimental equipment would be discovered. The reality of the situation is that the first fully analyzed data from the new MAX-lab facility are coming from an experiment measuring a cross section on the order of 10 nb/sr.

The small cross section of this experiment, combined with the extended target, the large photon spectrometer acceptances, the complicated time structure of the photon beam and its high rate, the 50% overlap of the hodoscope counters and the complicated nature of the tagger electronics lead in part to the delayed realization that the absolute cross section was much smaller than expected. Due to the multiple corrections that had to be applied, and the possibility that any or all of them could be substantial, the low preliminary results could always be explained by the anticipation of a large, subsequent correction. It was not until this thesis analysis was performed that it became obvious that the extracted cross section was much too small.

The apparent ability to extract the angular distribution of the Compton scattering cross section provides an indication that the source of the scaling factor may be common to all detectors and run periods. Unfortunately, it is also possible that there may be several sources that, in combination, result in the low cross section. Several potential methods of investigation into these sources will be discussed in the final section.

4.4 Suggestions for Future Work

There are two possible avenues to producing cross sections that are not subject to the previously discussed scaling factor. The first is to continue running the experimental program but with care taken to minimize the size of the corrections. The obvious advantage is that data will still be produced; however, it is possible that the source of the scaling factor may not be identified. The second method involves dedicated scattering from well-known targets and specific tests of the various factors that constitute the cross section. These measurements would not focus on exploring new physics, but would attempt to clearly identify the source of the scaling factor. Details of both methods are described below.

4.4.1 Minimizing Corrections

After performing a test run in March 2010 (see Appendix C) to gain an understanding of the tagger and beam characteristics, several potential improvements to the experimental setup became evident. These include:

- reducing the average beam intensity so that the stolen trues and ghosts corrections are reduced. Both of these effects increase with the electron rate. The greatest concern is the instantaneous beam rate which can be as much as ten times the average rate. This can be seen in the beam structure shown in Appendix C.

- running the accelerator in a new configuration which produces a beam with a slightly higher duty factor ($\sim$60%) and narrower structures in the ToF spectra (i.e., less beam structure and lower instantaneous rates).

- reducing the width of the tagger counter discriminator output signal from $\sim$45 ns to $\sim$30 ns. This change reduces the chance of the ghost (accidental) coincidences and, hence, its correction.

- increasing the tagger counter overlap to 100%. This completely eliminates not only the ghost coincidences but also the strange timing characteristics observed in the test run. Another advantage is that the pre-scaled FP trigger should give an accurate measure of the stolen trues confirming the existing Monte Carlo simulation.

- employing the multi-hit TDCs (with a proper setup) which allow for an analysis that does not require a stolen trues correction. The multiple stops are sufficient to guarantee that all prompt electrons will be recorded in the TDC.

Several of these steps were incorporated in a recent deuteron Compton scattering measurement in November 2009. Additionally, several were used in the setup of a pion photoproduction experiment in June 2010. Unfortunately, neither analysis is mature enough to provide input to the present work.

4.4.2 Dedicated Tests

The COMPTON@MAX-lab Collaboration has discussed several dedicated tests designed to extract scattering cross sections from several well-known targets. The tentative plan is to conduct these measurements in the fall of 2010 ([Fel10]). This program would include:

- one day of scattering from a lead target at an average electron beam rate of 1 MHz per tagger channel.
- two days of scattering from a carbon target at an average electron beam rate of 1 MHz per tagger channel.
- three days of scattering from a lead target at an average electron beam rate of 100 kHz per tagger channel.
- placing one photon spectrometer at the forward angle and the other two at a matching backward angle. This permits adjusting the solid angle of the two backward detectors so as to investigate any effects due to the larger acceptance.
- a potential second week of measurements to run at other beam rates or angles.
- incorporating some or all of the suggestions in the previous section.

As mentioned in chapter 2, a test run ([For10]) was conducted to measure the dependence of the tagging efficiency on the average beam rate. Unfortunately, due to the physical restrictions of the tagging magnet and photon beam collimator, it was only possible to attain a beam rate of $\sim$40 kHz which is only about 4% of the nominal beam rate in scattering configuration. At these reduced rates, the electron beam must be mis-steered prior to entering the MAX-I ring. Current discussions ([Kov10]) are focusing on developing a method of extending the test run to allow for measuring the tagging efficiency at both high and low beam rates. These measurements would potentially use an air Cherenkov detector (constructed with plastic pipe) in the beam with a mounted PMT that observes the beam from the side. The low efficiency of this system could be modified by adjusting the air pressure in the pipe and would permit stepping up the beam from typical tagging efficiency rates to nominal

scattering rates. This idea is still in the early stages of development, but a consensus is being reached that some test must be designed that can measure the tagging efficiency at scattering rates.

A second avenue to determining the tagging efficiency is being developed using a Geant4 simulation ([Lit10]). The setup of the simulation is still in progress and the magnetic field of the tagger magnet has not been implemented at this time. However, there is optimism that this simulation will shed more light onto the issue of the tagging efficiency.

Taken together, it is expected that these avenues of research will provide an understanding of the scaling factor. In the future, it is hoped that the scattering cross section presented in this thesis can be corrected and published resulting in a substantial improvement to the knowledge of the deuteron Compton scattering cross section and the global neutron polarizabilities.

5 Conclusions

The indications from this initial experiment at the upgraded MAX-lab facility are that angular distribution of the Compton scattering cross section can be obtained with the current understanding of the photon beam and spectrometers. The measured cross section is $\sim 2/3$ of the expected value for the targets studied in this thesis. Dedicated experiments using well-known targets and focused tests on specific aspects of the beam are planned for the near future. The aim is to continue this series of experiments under ever improving conditions thereby extracting an accurate deuteron Compton cross section and the resulting neutron polarizabilities.

A Tagged Photon Energies

Bin 1		Bin 2		Bin 3		Bin 4	
Tagger Channel	E_γ (MeV)	Tagger Channel	E_γ (MeV)	Tagger Channel	E_γ (MeV)	Tagger Channel	E_γ (MeV)
0	97.05	15	90.22	30	82.86	45	74.88
1	96.61	16	89.74	31	82.34	46	74.32
2	96.17	17	89.27	32	81.83	47	73.77
3	95.73	18	88.79	33	81.31	48	73.20
4	95.28	19	88.31	34	80.79	49	72.64
5	94.83	20	87.83	35	80.27	50	72.07
6	94.38	21	87.34	36	79.74	51	71.50
7	93.92	22	86.85	37	79.21	52	70.93
8	93.47	23	86.36	38	78.68	53	70.36
9	93.01	24	85.87	39	78.15	54	69.78
10	92.55	25	85.37	40	77.61	55	69.20
11	92.09	26	84.88	41	77.07	56	68.62
12	91.62	27	84.37	42	76.53	57	68.03
13	91.16	28	83.87	43	75.98	58	67.45
14	90.69	29	83.36	44	75.43	59	66.86
						60	66.27
						61	65.67

Table A.1: The tagged photon energies for the 2007 run period for each tagger channel.

Bin 1		Bin 2		Bin 3		Bin 4	
Tagger Channel	E_γ (MeV)	Tagger Channel	E_γ (MeV)	Tagger Channel	E_γ (MeV)	Tagger Channel	E_γ (MeV)
0	115.73	15	108.29	30	100.24	45	91.57
1	115.26	16	107.77	31	99.69	46	90.96
2	114.78	17	107.25	32	99.13	47	90.36
3	114.30	18	106.72	33	98.56	48	89.75
4	113.81	19	106.20	34	98.00	49	89.13
5	113.32	20	105.67	35	97.43	50	88.51
6	112.83	21	105.14	36	96.86	51	87.89
7	112.34	22	104.61	37	96.28	52	87.27
8	111.84	23	104.07	38	95.70	53	86.64
9	111.34	24	103.53	39	95.12	54	86.01
10	110.84	25	102.99	40	94.54	55	85.38
11	110.33	26	102.45	41	93.95	56	84.74
12	109.82	27	101.90	42	93.36	57	84.10
13	109.31	28	101.35	43	92.77	58	83.45
14	108.80	29	100.80	44	92.17	59	82.81
						60	82.16
						61	81.50

Table A.2: The tagged photon energies for the 2008 run period for each tagger channel.

B Gain Monitoring

Reconstructing the energy deposition of a photon in the NaI detector requires converting the ADC readout into an energy. The ADC readout is proportional to the gain of the PMT and this value can change over time due to environmental effects (power surges, external fields, temperature, etc.). Given the need for high energy resolution to extract an accurate cross section it was imperative that the gains in all parts of the NaI were tracked and corrected for over time. Based on work done by [Lun02], the suggestion was made to use cosmic ray events to monitor the gain drifts throughout the run period. The first section will detail the work done in testing this procedure. The second will briefly review the implementation of cosmic ray gain monitoring and the effect on the final scattering lineshape.

B.1 Cosmic Ray Test Run

In June 2007, a one day test run was conducted at MAX-lab for the purposes of testing the feasibility of gain monitoring via cosmic rays. Given the rather limited beam time, it was decided that the gain should be artificially introduced by adjusting the high voltages on the NaI PMTs. The run plan consisted of a calibration run, followed immediately by a dedicated cosmic ray run. The high voltages were adjusted, and then another cosmic ray run and calibration run were conducted.

The tagged photons in the two calibration runs must have the same energy. However, the ADC values will differ due to the change in the gain. The cosmic ray runs can then be used to correct the second calibration run.

The cosmic ray data were fit to a modified Gaussian distribution given by:

$$f(x) = \begin{cases} p_0 e^{\frac{(x-p_2)^2}{-2p_1^2}} & (x \leq p_2) \\ p_0 e^{\frac{(x-p_2)^2}{-2p_1^2}} + p_3 e^{-p_5 x}(1 - e^{\frac{(x-p_2)^2}{-2p_4^2}}) & (x \geq p_2) \end{cases} \tag{B.1}$$

A fit of this distribution to a sample cosmic ray spectrum is shown in Fig. B.1. By comparing the fits to a standard run taken at the time of a calibration run the gain drift for each PMT can be determined. The effect of this gain correction for the June 2007 test run can be seen in Fig. B.2.

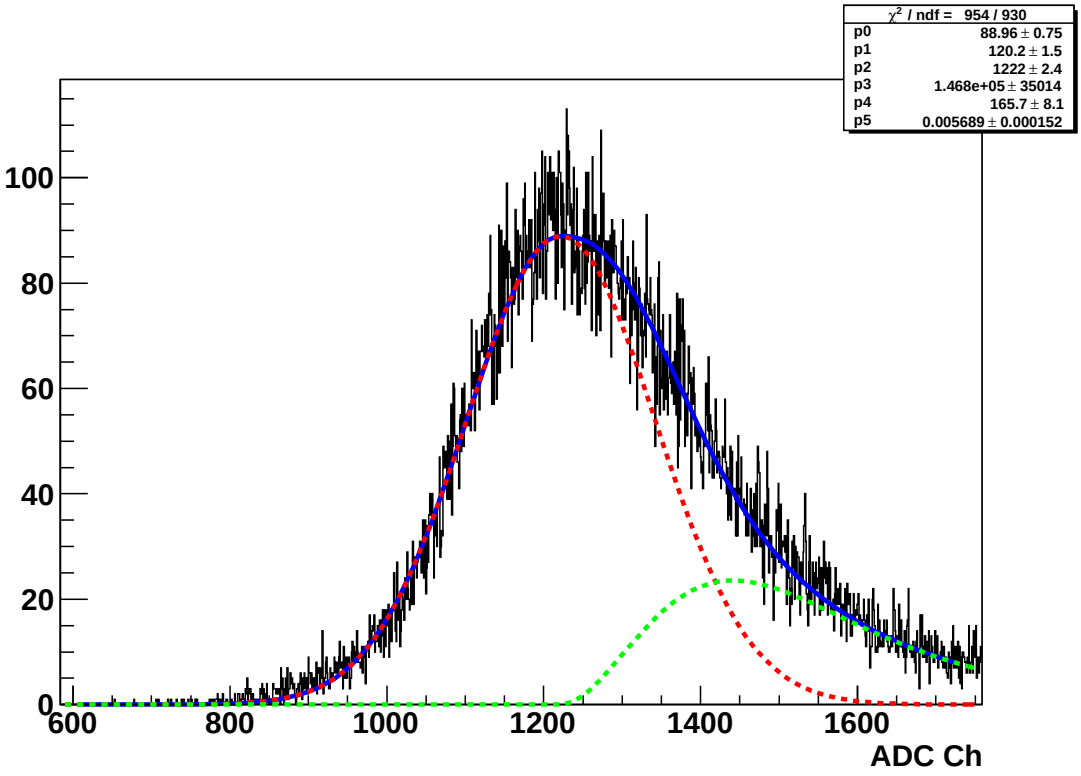

Figure B.1: Sample of modified Gaussian distribution fit to PMT cosmic ray spectrum. The thick, solid line is the fitted lineshape. The dashed lines represent the two functions that make up the fit. Variation of this lineshape from run to run was assumed to be due to changes in the gain of the PMT.

B.2 Scattering Runs Gain Correction

The same procedure that was applied to the data from the June 2007 test run was used in the production data to correct for gain drifts. It was found that the largest fraction of the gain drift occurred immediately after moving the NaI from the calibration position into its scattering position. The theory is that this is due to a stray magnetic field from the MAX-III ring directly above the nuclear physics experimental area; there was not sufficient time to investigate the cause, though. The ability to correct for gain drifts was seen as the pressing priority.

During a run period, a cosmic ray run was collected immediately after the calibration run and before moving the detector into its scattering position. This provided a reference that allowed for an accurate energy calibration of the scattering runs. Once in scattering

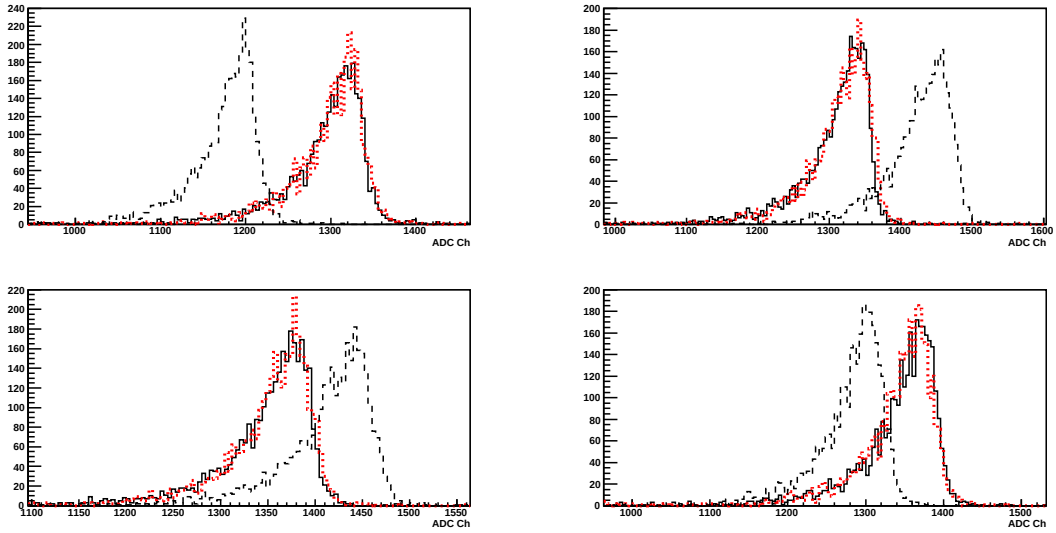

Figure B.2: PMT ADC spectra from the June 2007 test run. The lineshape from the 1^{st} calibration run is shown by the solid line. The lineshape from the 2^{nd} calibration run is shown without a gain correction (dashed) and with a gain correction (dotted, red).

position the PMT gains tended to drift only a few percent. While this may seem like a small effect, as seen in Fig. B.3 the position of the elastic peak is off-center without the applied gain corrections.

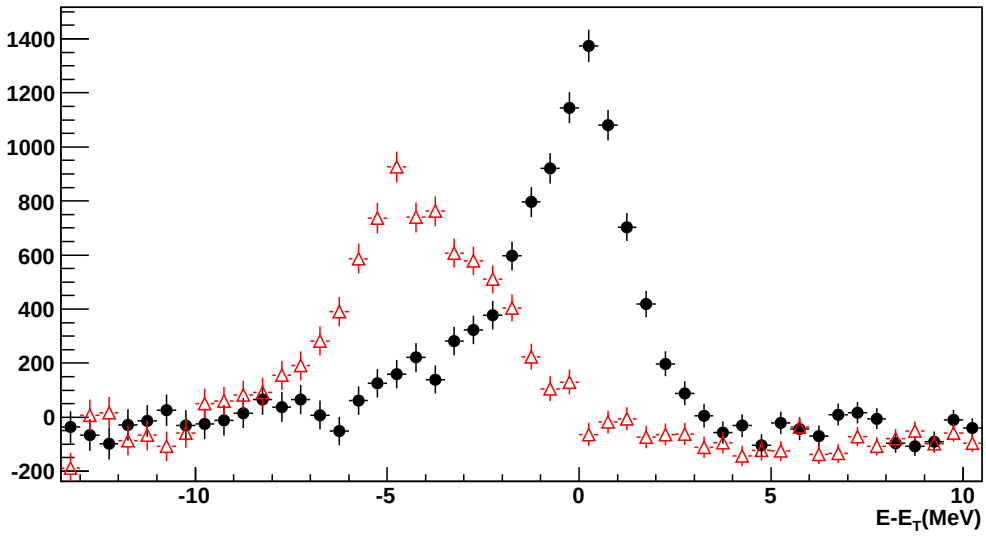

Figure B.3: Comparison of elastic peak lineshape with (•) and without (Δ) gain corrections. The application of the gain corrections moves the peak to the proper photon energy and also restores the energy resolution to the value obtained in the calibration run.

C Tagger Rate-Dependent Corrections

In March 2010 a test run was conducted for the purposes of understanding the corrections due to rate-dependent effects in the SAL hodoscope. The basis for this work was a similar study done in the 1990's at SAL [Mac95]. The purpose was to understand the behavior of the electronics so that a simulation could be written that would enable the effects of stolen trues and ghosts to be calculated. Since these effects have been discussed in previous works of this nature only a cursory overview of the phenomena will be discussed here. The first section will deal with the specific tests conducted during the test run. The second section will detail the setup of the tagger simulation and how it compares to a controlled data set from the production runs.

C.1 Tagger Rate Tests

The rate tests were designed to examine specific details of the tagger electronics. Each component was tested: the discriminators, the overlap modules, the TDCs and the scalers. The specifics are below.

Discriminators The hodoscope discriminators are run in burst guard mode. This prevents the discriminators from locking up during high rate beam bursts. In this mode, the first electron will trigger the discriminator and produce a NIM output pulse with a pre-set width. If no other electron occurs within the output pulse the discriminator resets after the fixed time. However, if a second electron occurs while the discriminator is still down then the output pulse will have a duration equal to the longer of the fixed width or the second pulse recrossing the threshold. The discriminator locks out any other electrons until the discriminator has been reset to zero.

The pulse width of the minimum ionizing electrons in the hodoscope scintillators was measured to be 12 ns at the discriminator threshold. The pre-set width of the output widths were ~ 45 ns.

Overlap Modules The overlap modules used in the tagger electronics were modules built and used at SAL. These modules take the discriminator outputs from the 63 counters and

form coincidences between consecutive counters to create the overlap channels. Identical copies of a discriminator output were fed into neighboring counters and by delaying one counter the overlap module output signal could be observed. The overlap modules were designed so that their output pulse width is the same as the amount of overlap in the incoming signals. The minimum overlap necessary to create a coincidence signal is 3 ns.

Tagger Channel TDC Behavior Two tests were used to understand the behavior of the TDCs used for the tagger electronics. The first was an overlap resolution test. As described above, identical signals were sent to the overlap modules with some relative delay. The delay was increased until the TDC no longer observed a stop signal in the overlap channel. Surprisingly, this occurred at an overlap width at 11 ns, not the 3 ns needed for the overlap modules.

The second test was designed to understand the response of the TDC to the ghost signals in the overlap channel. The first attempt was set up as shown in Fig. C.1. The test used the signals from the x-paddles to create both a self-timing TDC (to identify which paddle was the trigger) and also as an additional signal to the hodoscope electronics. Accidental electrons in other counters would then form ghost coincidences with the x-paddle signals and these would be seen clearly in the TDC spectrum. From similar work done at SAL the expectation was that the ghosts would show up as a sharp peak with shelf trailing off to the right. However, as can be seen in Fig. C.2, the ghost spectrum from this test shows a sharp peak with a short shelf to the right and a satellite peak to the left. Similarly, the overall width of the ghost structure was narrower than anticipated from the SAL work. These results necessitated another attempt to understand the behavior of ghost events in the tagger channel TDCs.

The setup for the second attempt was identical to the setup used in the overlap resolution test. In this case, a second channel without delay between its counters was used to provide a trigger. Unlike the resolution test, the TDC peak positions were measured for the channel as a function of the overlap width of the incoming TDC stop. The channel with synchronized overlap inputs provides a steady TDC spectrum with which to compare the ghost timing. As seen in Fig. C.3, as delay is added to the ghost channel, the position of the ghost peak

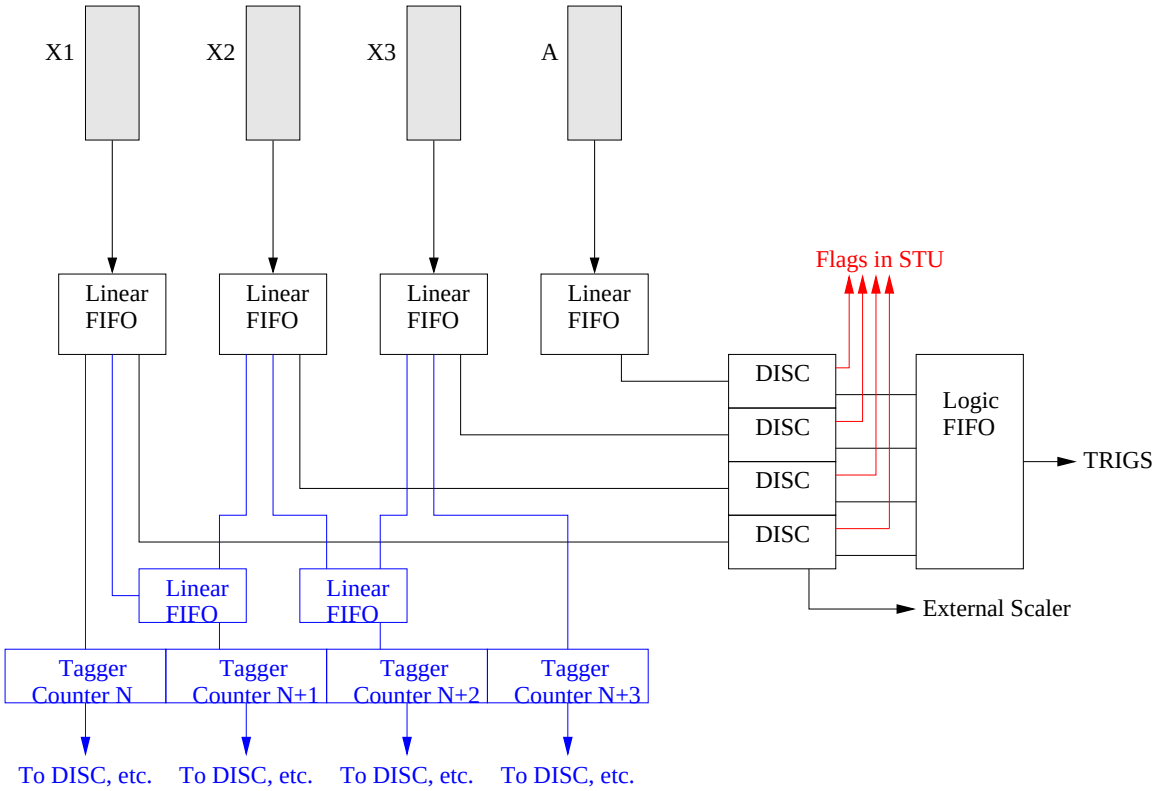

Figure C.1: Electronics setup for the x-paddle test used during the March 2010 test run. This test was critical to understanding the probability of creating a ghost accidental and understanding the timing of the ghosts in the TDC.

moves. Since the later pulse going into the overlap module is the one setting the timing the expectation is that for negative delay the peak position would be unchanged and that for positive delay the ghost peak would move later in time exactly equal to the amount of delay. The results are obviously incompatible with this interpretation, but it does agree with the behavior seen in the earlier attempt with the x-paddles. This behavior can not be explained, but it can be readily incorporated into a tagger simulation.

Tagger Channel Scaler Behavior Since there is no timing component in the scalers, the only concern was the overlap resolving time. The same setup was used an in the TDC overlap test and it was found that a minimum overlap pulse width of 3 ns was necessary for the pulse to be recorded in the scaler.

A second test was conducted to provide more information on the behavior of the tagger

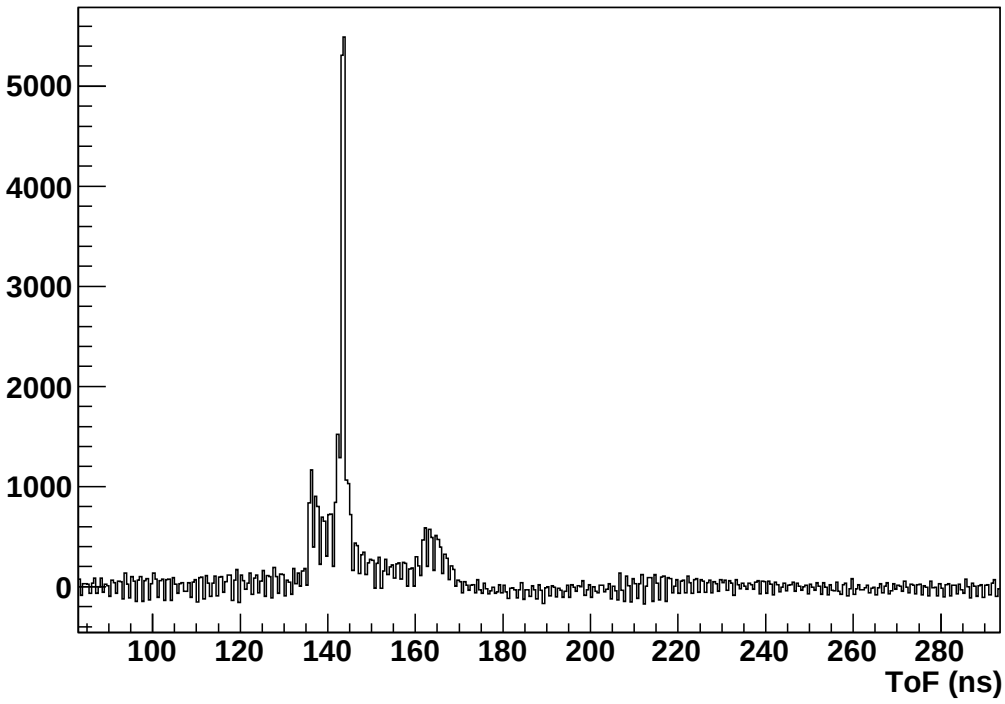

Figure C.2: Structure of the ghost events (with random background subtracted) from the x-paddle test. The majority of the ghosts appear within the prompt peak region. Due to the characteristics of the tagger electronics, the ghosts can also appear both to the left and right of the prompt peak as seen in the smaller structures in this spectrum.

channel scalers. This test was designed to investigate the deadtime in the scaler arm (due to deadtime in the discriminators, overlap, and scalers) as a function of beam rate. Four hodoscope counters were used individually, in pairs, and four-fold. The individual counters are fed into scalers to be used as the expected rate in the other counts. The fraction of lost counts in the pairs and four-fold scalers were then an indication of the deadtime.

The results of these, and the test above, are discussed further in the next section.

C.2 The Tagger Simulation

The information gathered during the tagger test run was used to develop a tagger simulation that could calculate the corrections that resulted from the rate-dependent effects. The simulation has the following steps:

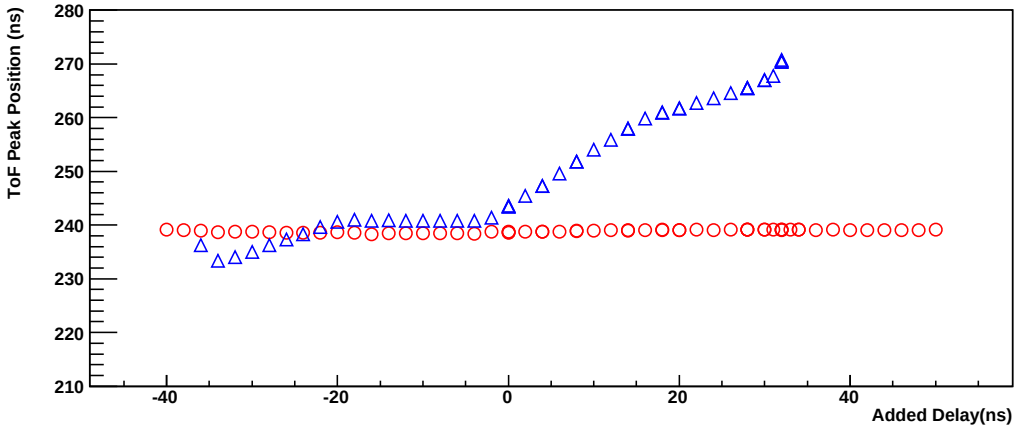

Figure C.3: Behavior of the true (○) and ghost (Δ) ToF peak as a function of delay removed/added to the ghost signal. The timing of the true signal does not vary since no delay is added to this tagger channel. The ghost ToF peak moves as a function of delay since the timing of the tagger channel is determined by the second counter to fire. The non-linearity is due to timing characteristics of the electronics.

1. Input parameters are initialized for the average tagger channel rates, the discriminator output widths, assorted trigger rates, and other relevant values.

2. The electron beam time profile is extracted from the TDC data.

3. Once initialized, the simulation proceeds to create and track electrons and pulses through the hodoscope electronics one nanosecond at a time.

4. Using Poisson statistics, the simulation first checks to see if an electron is detected in the overlap channels. If so, then the appropriate counter discriminators are updated as defined by the burst guard mode operation.

5. The overlap modules then produce an output based on the overlap of neighboring counters.

6. Triggers are set based on the rates set in the initialization. If a trigger has occurred an inhibit is also set.

7. Tagger channel scalers and TDCs are filled based on the overlap time, trigger time and the presence/absence of an inhibit signal.

C.2.1 Beam Time Profile

In order for the simulation to work properly, the time profile of the electron beam needed to be extracted from the data. This was a non-trivial exercise. The complicated structure of the TDCs (see Fig. 3.7) hints at the nature of the electron beam profile but is not sufficient to make any quantitative statements about the profile. The extraction of the beam profile is done by:

1. Fill the multi-hit TDC with only accidental events. This was most easily accomplished by considering the pre-scaled FP trigger data and using all channels physically separated from the triggering channel.

2. The profile of the accidentals in the multi-hit TDC is assumed to be an auto-correlation of the electron beam profile: $P_{MHTDC} = \int_{-\infty}^{\infty} P_e(\tau)\ P_e(\tau - t)\ \mathrm{d}\tau$.

3. Working off the assumption above, the electron beam profile, $P_e(t)$, can be extracted by taking the Fourier transform of the accidental multi-hit TDC profile, taking the root, and then taking the inverse Fourier transform.

In order to confirm the above method the extracted beam profile was used as an input and the simulation was run for a typical pre-scaled FP trigger. The TDC spectrum (single-hit) from the data is shown as the solid line in Fig. C.4. The multi-hit spectrum used in the beam profile extraction was taken from this same data set. The beam profile is shown in Fig. C.5. The duty factor of this beam is $\sim 30\%$, which when coupled with the increased count rate at the upper end of the SAL hodoscope, yields an instantaneous beam rate of $\sim$ 10 MHz. These very high rates are the reason obtaining an accurate simulation of the ghosts and stolen trues is such a concern. The TDC spectrum that is generated by the simulation is shown as the dashed line in Fig. C.4. The excellent agreement, even with such a complicated structure, gives credence to this method and simulation.

C.2.2 Simulation Results

With the simulation written to reflect the knowledge gained from the tagger tests, the challenge was to compare to the simulation to data collected during running. The first

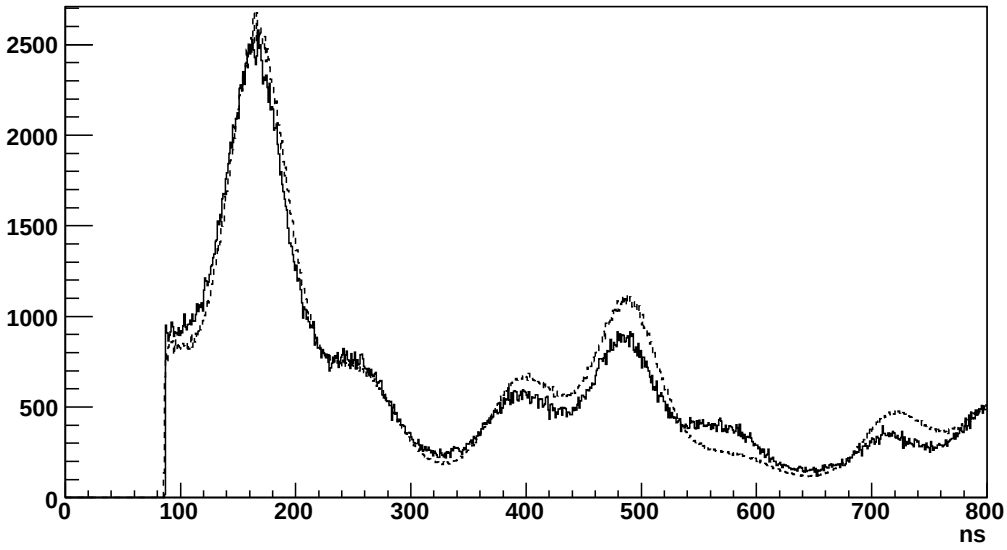

Figure C.4: Comparison of the single-hit TDC spectrum from the data (solid) and the tagger simulation (dashed). Data taken from the 2007 run period. Due to the beam tuning during this run there are structures with a period of ∼110 ns and ∼330 ns. The ability of the simulation to replicate such a complicated spectrum is seen as confirmation of its validity.

comparison was made to the scaler rate test discussed above. As seen in Fig. C.6 the simulation accurately reproduces the results of this test.

The second comparison was made with data collected using a pre-scaled FP trigger that was part of the x-trigger in the production running. By firing on electrons this trigger should see only a prompt peak and stolen trues in the TDC spectrum. The simulation, then, should be able to replicate the stolen trues fraction for this subset of the data. The stolen trues fraction as a function of rate is shown in Fig. C.7 for both the data and the simulation. This analysis lead to the systematic uncertainty of the stolen trues correction that is stated as ±2%.

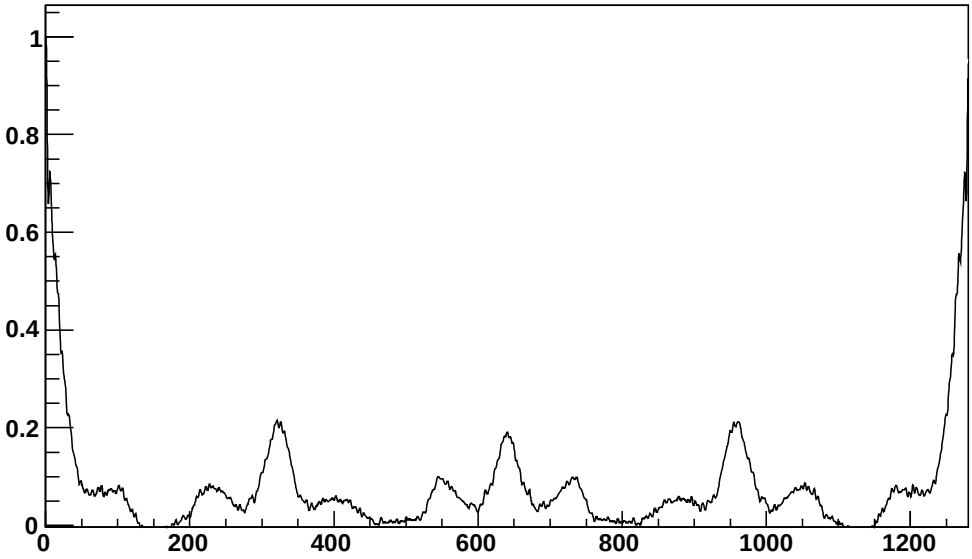

Figure C.5: Relative extracted beam profile (in ns) from the 2007 run period as determined via the auto-correlation and Fourier transform method discussed in the text.

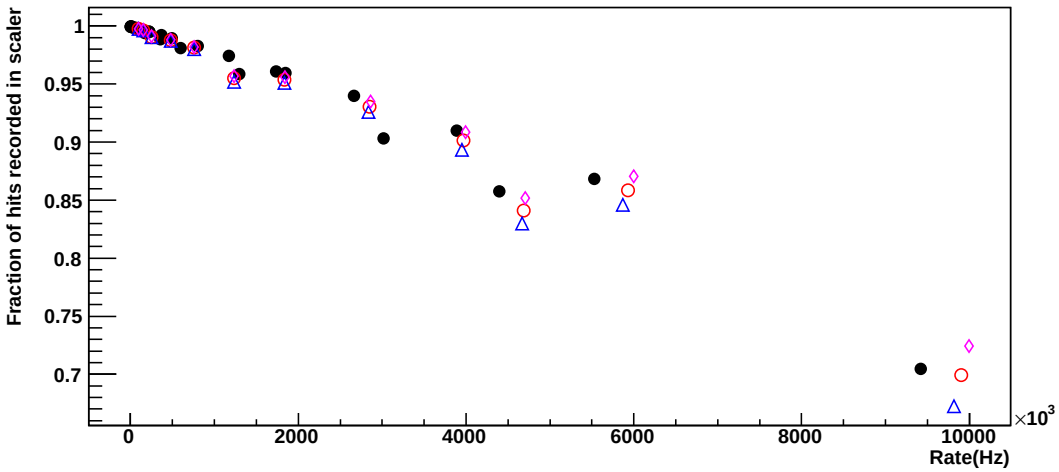

Figure C.6: Comparison of tagger simulation to data (•) collected during the scaler rate test. The simulation was run for beam profiles with duty factors of 0% (Δ), 50% (○) and 100% (♢).

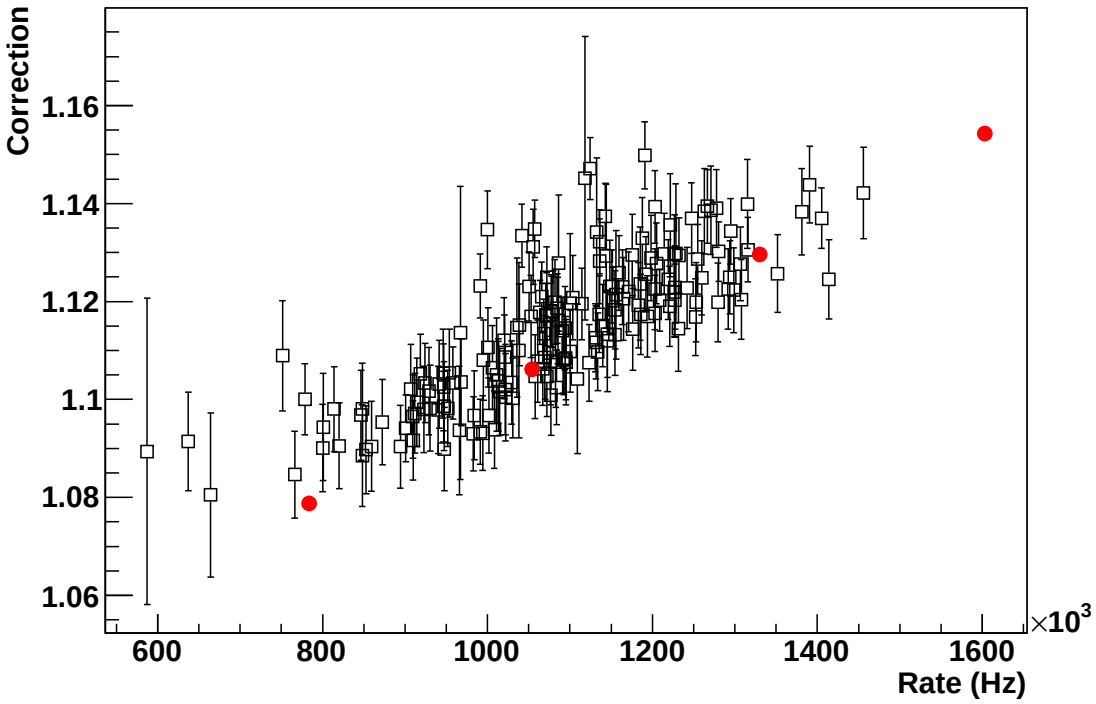

Figure C.7: Comparison of the stolen trues correction for the pre-scaled focal plane trigger. The corrections from the tagger simulation (•) and the collected data (□) are shown as a function of the average beam rate.

D Carbon Factors

This appendix contains tables of the factors, unique to the carbon analysis, for extracting its cross section. These include the yield, $t\Omega_{eff}$, and the ghost and stolen trues corrections. The tagging efficiency is the same as those listed in the deuterium analysis. The density of the carbon target was measured to be $1.83 \pm 0.06 \frac{g}{cm^3}$.

	$\theta_{Lab} = 60°$			$\theta_{Lab} = 120°$			$\theta_{Lab} = 150°$		
E_γ(MeV)	Y	δY^{stat}	δY^{syst}	Y	δY^{stat}	δY^{syst}	Y	δY^{stat}	δY^{syst}
94	548	65	44	839	47	40	405	36	25
87	1116	93	74	1425	57	42	613	42	23
79	1341	126	92	1869	70	40	1021	50	31
70	1850	183	151	2677	93	27	1525	65	53
112	1072	78	55	1145	69	43	444	40	46
105	1340	96	33	1672	88	30	696	49	36
96	1669	116	121	2266	108	42	1150	63	46
87	2410	148	49	3643	137	73	1783	85	62

Table D.1: The yields for each detector and energy bin obtained from scattering from the carbon target.

	$\theta_{Lab} = 60°$		$\theta_{Lab} = 120°$		$\theta_{Lab} = 150°$	
E_γ(MeV)	$\kappa\Omega_{eff}$ (mm msr)	$\frac{\kappa\Omega_{eff}}{\kappa\Omega_{meas}}$	$\kappa\Omega_{eff}$ (mm msr)	$\frac{\kappa\Omega_{eff}}{\kappa\Omega_{meas}}$	$\kappa\Omega_{eff}$ (mm msr)	$\frac{\kappa\Omega_{eff}}{\kappa\Omega_{meas}}$
94	1537	0.75	2366	0.70	1182	0.75
87	1563	0.76	2431	0.72	1211	0.77
79	1590	0.77	2517	0.75	1233	0.78
70	1625	0.79	2629	0.78	1282	0.82
112	1626	0.79	2285	0.68	1119	0.71
105	1644	0.80	2339	0.70	1152	0.73
96	1648	0.80	2420	0.72	1175	0.75
87	1681	0.82	2511	0.75	1212	0.77

Table D.2: Comparison of the measured and effective values of $t\Omega$ for carbon scattering.

	$\theta_{Lab} = 60°$			$\theta_{Lab} = 120°$			$\theta_{Lab} = 150°$		
E_γ(MeV)	f_{ghost}	δf^{stat}_{ghost}	δf^{syst}_{ghost}	f_{ghost}	δf^{stat}_{ghost}	δf^{syst}_{ghost}	f_{ghost}	δf^{stat}_{ghost}	δf^{syst}_{ghost}
94	1.031	0.010	0.015	1.022	0.010	0.011	1.018	0.010	0.009
87	1.018	0.010	0.010	1.013	0.010	0.007	1.009	0.010	0.007
79	1.036	0.010	0.020	1.027	0.010	0.015	1.022	0.010	0.013
70	1.027	0.010	0.015	1.014	0.010	0.011	1.010	0.010	0.010
112	1.013	0.005	0.005	1.012	0.005	0.005	1.007	0.005	0.005
105	1.009	0.005	0.005	1.009	0.005	0.005	1.003	0.005	0.005
96	1.015	0.005	0.007	1.015	0.005	0.007	1.007	0.005	0.005
87	1.010	0.005	0.006	1.010	0.005	0.006	1.004	0.005	0.006

Table D.3: The ghost corrections for carbon scattering as obtained from the tagger simulation.

	$\theta_{Lab} = 60°$			$\theta_{Lab} = 120°$			$\theta_{Lab} = 150°$		
E_γ(MeV)	f_{stolen}	δf^{stat}_{stolen}	δf^{syst}_{stolen}	f_{stolen}	δf^{stat}_{stolen}	δf^{syst}_{stolen}	f_{stolen}	δf^{stat}_{stolen}	δf^{syst}_{stolen}
94	1.152	0.004	0.023	1.196	0.004	0.024	1.154	0.004	0.023
87	1.190	0.004	0.024	1.249	0.004	0.025	1.194	0.004	0.024
79	1.228	0.004	0.025	1.304	0.004	0.026	1.235	0.004	0.025
70	1.273	0.004	0.025	1.370	0.004	0.027	1.283	0.004	0.026
112	1.105	0.004	0.022	1.235	0.004	0.025	1.113	0.004	0.022
105	1.118	0.004	0.022	1.266	0.004	0.025	1.127	0.004	0.023
96	1.140	0.004	0.023	1.319	0.004	0.026	1.151	0.004	0.023
87	1.164	0.004	0.023	1.379	0.004	0.028	1.177	0.004	0.024

Table D.4: The stolen trues corrections for carbon scattering as obtained from the tagger simulation.

References

[Arn96] R. A. Arndt, I. I. Strokovsky, and R. L. Workman, Phys. Rev. C **53**, 430 (1996).

[Bab98] D. Babusci, *et. al.*, Phys. Rev. C **58**, 1013 (1998).

[Bal60] A. M. Baldin, Nuc. Phys. **18**310 (1960).

[Bar74] P. Baranov, *et. al.*, Phys. Lett. **52B**, 122 (1974).

[Bea03] S. R. Beane, *et. al.*, Phys. Lett. **B567**, 200 (2003).

[Ber94] V. Bernard, *et. al.*, Z. Phys. A **348**, 317 (1994).

[Car83] L. S. Cardman, *Photon Tagging, Present practice and future prospects,* Proceedings of The Magnetic Spectrometer Workshop, Williamsburg, Virginia (1983).

[Eni97] T. L. Enik, *et. al.*, Sov. J. Nuc. Phys. **60**, 567 (1997).

[Fed91] F. J. Federspiel, *et. al.*, Phys. Rev. Lett. **67**, 1511 (1991).

[Fel04] G. Feldman, M. Kovash, *Elastic Compton Scattering From Deuterium at 40-110MeV*, MAX-lab PAC Meeting, Lund, Sweden (2004).

[Fel10] G. Feldman, Private Communication (2010).

[For10] U. Forsberg, B. Sc. Thesis, Lund University, 2010.

[Gea10] http://geant4.cern.ch/

[Gle93] T. Glebe, Ph. D. Thesis, Georg-August-Universitat, Gottingen, 1996.

[Gri08] H. W. Griesshammer, *Nucleon Polarizabilities from Deuteron Compton Scattering*, MAX-lab PAC Meeting, Lund, Sweden (2008).

[Gri10] H. W. Griesshammer, D. Shukla, To be published and private communication (2009/2010).

[Han05] K. Hansen, *MAX-lab Activity Report 2005-06*, pp 458-9.

[Han07] K. Hansen, *MAX-lab Activity Report 2007*, pp 424-5.

[Hil05] R. P. Hildebrandt, *et. al.*, Nuc. Phys. A **748**, 573 (2005).

[Hor99] D. L. Hornidge, Ph. D. Thesis, University of Saskatchewan, 1999.

[Hor00] D. L. Hornidge, *et. al.*, Phys. Rev. Lett. **84**, 2334 (2000).

[Koe88] L. Koester, Z. Phys. A **329** 229 (1998).

[Koe95] L. Koester, *et. al.*, Phys. Rev. C **51**, 3363 (1995).

[Kol00] N. R. Kolb, *et. al.*, Phys. Rev. Lett. **85**, 1388 (2000).

[Kos02] K. Kossert, *et. al.*, Phys. Rev. Lett. **88**, 162301 (2002).

[Kov08] M. Kovash, Private Communication (2008).

[Kov10] M. Kovash, Private Communication (2010).

[Kum09] D. Kumbaro, *MAX-lab Injector*, Lund University (2009).

[Lev00] M. I. Levchuk, A. I. L'vov, *et. al.*, Nuc. Phys. A **674**, 449 (2000).

[Lit10] M. Litwack, Private Communication (2010).

[Luc94] M. A. Lucas, Ph. D. Thesis, University of Illinois (1994).

[Lun02] M. Lundin, Ph. D. Thesis, Lund University (2002).

[Lun05] M. Lundin, *MAX-lab Activity Report 2005-06*, pp 464-5.

[Lvo97] A. I. L'vov, *et. al.*, Phys. Rev. C **55**, 359 (1997).

[Mac95] B. E. MacGibbon, Ph. D. Thesis, University of Illinois 1995.

[Mil88] J. P. Miller, *et. al.*, Nuc. Inst. Methods A **270**, 431 (1988).

[Olm01] V. Olmos de Leon, *et. al.*, Eur. Phys. J A **10**, 207 (2001).

[Pet81] V. A. Petrun'kin, Sov. J. Part. Phys. **11**, 278 (1981).

[Phi04] D. Phillips, *Nucleon Polarizabilities from Compton Scattering on Deuterium: An Opportunity for MAX-lab*, MAX-lab PAC Meeting, Lund, Sweden (2004).

[Pow49] J. L. Powell, Phys. Rev. **75**, 32 (1949).

[Roo10] http://root.cern.ch/drupal/

[Ros90] K. W. Rose, *et. al.*, Nuc. Phys. A **514**, 621 (1990).

[Sch88] J. Schmiedmayer, *et. al.*, Phys. Rev. Lett. **61**, 1065 (1988).

[Sch90] K. P. Schelhaas, *et. al.*, Nuc. Phys. A**506**, 307 (1990).

[Sch91] J. Schmiedmayer, *et. al.*, Phys. Rev. Lett. **66**, 1015 (1991).

[Sch08] B. Schroeder, *The MAX-lab Facility and COMPTON@MAX-lab*, Workshop on Soft Photons and Light Nuclei, Seattle, Washington (2008).

[Vog93] J. M. Vogt, *et. al.*, Nuc. Inst. Methods A **324**, 198 (1993).

[War01] B. J. Warkentin, *et. al.*, Phys. Rev. C **64**, 014603 (2001).

[Wis94] F. Wissmann, *et. al.*, Phys. Lett. B **335**, 119 (1994).

[Wis99] F. Wissmann, *et. al.*, Nuc. Phys. A **660**, 232 (1999).

[Zie92] A. Zieger, *et. al.*, Phys. Lett. B **278**, 34 (1992).